

DOCTORAL THESIS

Novel Mechanisms of Robot Locomotion: Variable Stiffness Actuators for Underwater and Multi-phase Environments

Roza Gkliva

TALLINN UNIVERSITY OF TECHNOLOGY
DOCTORAL THESIS
3/2023

Novel Mechanisms of Robot Locomotion: Variable Stiffness Actuators for Underwater and Multi-phase Environments

ROZA GKLIVA



TALLINN UNIVERSITY OF TECHNOLOGY
School of Information Technologies
Department of Computer Systems

**The dissertation was accepted for the defence of the degree of Doctor of Philosophy
(Computer and Systems Engineering) on January 20th 2023**

Supervisor: Prof. Maarja Kruusmaa,
Department of Computer Systems, School of Information Technologies,
Tallinn University of Technology
Tallinn, Estonia

Opponents: Prof. Cesare Stefanini,
Scuola Superiore Sant'Anna,
Pisa, Italy

Prof. João Sousa,
Universidade do Porto,
Porto, Portugal

Defence of the thesis: February 3rd 2023, Tallinn

Declaration:

Hereby I declare that this doctoral thesis, my original investigation and achievement, submitted for the doctoral degree at Tallinn University of Technology, has not been submitted for any academic degree elsewhere.

Roza Gkliva

signature



European Union
European Regional
Development Fund



Investing
in your future

Copyright: Roza Gkliva, 2023
ISSN 2585-6898 (publication)
ISBN 978-9949-83-950-6 (publication)
ISSN 2585-6901 (PDF)
ISBN 978-9949-83-951-3 (PDF)
Printed by Koopia Niini & Rauam

TALLINNA TEHNIKAÜLIKOOL
DOKTORITÖÖ
3/2023

Robotite uued liikumismehhanismid: muutuva jäikusega täiturid veealustes ja mitmefaasilistes keskkondades

ROZA GKLIVA



Contents

Abstract.....	7
Kokkuvõte	9
List of Publications	11
Author's Contributions to the Publications	12
Abbreviations.....	13
Introduction	14
1 Background	17
1.1 Robot locomotion in aquatic environments	17
1.1.1 Bio-inspired underwater locomotion	17
1.2 Amphibious robot locomotion	18
1.2.1 Soft actuators for amphibious locomotion.....	19
1.3 Locomotion using variable stiffness actuation.....	20
1.3.1 VSA for aquatic locomotion	20
1.3.2 VSA for terrestrial locomotion	21
1.3.3 VSA for amphibious locomotion	21
1.4 Conclusions.....	21
2 Underwater thrust vectoring	23
2.1 Leveraging material properties	23
2.1.1 Fin design and fabrication.....	24
2.1.2 Oscillatory motion pattern and control	25
2.1.3 Experimental characterization of forces.....	26
2.1.4 Conclusion	28
2.2 Leveraging actuator morphology and material properties.....	28
2.2.1 Flapped paddle concept design and fabrication	29
2.2.2 Actuator dynamic model.....	30
2.2.3 Experimental characterization of actuator forces.....	31
2.2.4 Trials with the μ -CAT robot	34
2.2.5 Discussion and Conclusion	34
2.3 Conclusions.....	35
3 Variable stiffness actuation for amphibious locomotion	36
3.1 Actuator material modelling.....	37
3.1.1 Uniaxial tensile tests and data processing	37
3.1.2 Yeoh hyperelastic model	39
3.1.3 Material model experimental validation	40
3.2 Actuator design and fabrication	41
3.3 Experimental evaluation of locomotion performance.....	43
3.3.1 Natural frequency analysis.....	44
3.3.2 Motion patterns and control.....	44
3.3.3 Characterization of propulsive forces	45
3.3.4 Characterization of tractive behaviour	46
3.4 Discussion and Conclusions.....	48

4 Conclusions and future outlook	50
List of Figures	52
References	53
Acknowledgements	63
Appendix 1	65
Appendix 2	73
Appendix 3	81
Curriculum Vitae	91
Elulookirjeldus.....	92

Abstract

Novel Mechanisms of Robot Locomotion:

Variable Stiffness Actuators for Underwater and Multi-phase Environments

A significant proportion of our planet's surface is covered by water, and despite extensive effort, large areas of it remain unexplored. The research and scientific communities for a while now have shown considerable interest in the study, the protection, and the sustainable exploitation of the oceans' natural resources. The demand for remote and safe access to aquatic and mixed environments has led to the proliferation of autonomous and remotely operated robotic vehicles that aim to negotiate these challenging conditions. As the field of robotics advances, the methods of locomotion evolve to achieve more efficient and agile manoeuvring, employing a variety of actuator designs and configurations.

Traditional methods of robot locomotion are optimized for specific environmental conditions, with most common strategies featuring legs and wheels for terrestrial locomotion and propellers for underwater swimming. The performance of these methods declines when the environmental conditions change. To mitigate the diminishing performance in these conditions, the research community has been investigating alternative methods of locomotion that include non-traditional actuator designs and compliant materials. While actuators that can dynamically adjust their stiffness and shape have been studied in a wide range of applications throughout the years, there is a significant gap in underwater robotics.

This thesis investigates the premise that hybrid and non-traditional actuation systems that comprise compliant parts with variable stiffness can be effective for locomotion in a wide range of environmental conditions and locomotion scenarios. The hypothesis was that variable stiffness actuation will enable reconfigurability that can improve actuator force output and enable locomotion in a variety of aquatic and mixed environments, without increased control and motion planning requirements. For this purpose, three actuator prototypes were developed in order to experimentally investigate actuator morphology and material selection. The first two prototypes consisted of actuators with compliant parts that feature non-uniform stiffness, and focused on the investigation of underwater thrust vectoring. The experimental evaluation showed that while the non-uniform stiffness profile greatly improved the force output and efficiency of the actuators, it somewhat reduced the repertoire and range of locomotion patterns the robot could achieve. Based on the findings of the first two investigations, the work expanded to locomotion in more diverse environmental conditions, studying amphibious locomotion with variable stiffness actuation. The third prototype relying on a material and design that allow reconfigurability of shape and stiffness, demonstrated multi-modal locomotion in aquatic and terrestrial conditions, as well as on submerged terrain that emulates the transition between aquatic and terrestrial locomotion.

This work demonstrated locomotion in a variety of aquatic and amphibious scenarios. Compared to most existing variable stiffness actuators for thrust vectoring and more notably for multi-modal amphibious locomotion, the mechanical complexity as well as the control and motion planning requirements of all prototypes presented in this thesis are significantly low. Additionally, while most implementations of amphibious locomotion rely on rigid and fast-moving components that can be harmful to the actuator and to the surrounding environment, this work relied on mostly soft parts and demonstrated minimal impact to the surroundings.

This study can lead to further improvements in actuator performance for locomotion

in more challenging environmental conditions. The experimental study and analysis of these methods provides a deeper understanding of their benefits and limitations. This can help identify and further advance the technologies that are currently delaying progress in this field, eventually increasing the operational autonomy of the robots that use them. Additionally, the demonstrated low impact motion and low disturbance of the surroundings encourages the wider adoption of variable stiffness actuation for applications that require low environmental impact. Lastly, the insights into variable stiffness actuation can be transferable to other disciplines of robotics beyond locomotion, such as grasping and rehabilitation.

Kokkuvõte

Robotite uued liikumismehhanismid: muutuva jäikusega täiturid veealustes ja mitmefaasilistes keskkondades

Märkimisväärne osa meie planeedi pinnast on kaetud veega ning vaatamata ulatuslikele pingutustele, on suured alad sellest avastamata. Uurimis- ja teadusringkonnad on juba mõnda aega näidanud üles märkimisväärset huvi ookeanide loodusvarade uurimise, kaitse ja säästva kasutamise vastu. Nõudlus ohutu kaugjuurdepääsu järele veekeskondades ja nendega piirnevas, on viinud autonoomsete ja kaugjuhitavate robotsõidukite kiire levikuni, millede eesmärgiks on nendes keerulistes tingimustes hakkama saamine. Arengutega robotikas arendatakse ka liikumismeetodeid tõhusamaks ja agiilsemaks, kasutades selleks erinevaid täiturmehhanismide konstruktsioone ja konfiguratsioone.

Traditsioonilised robotite liikumisviisid on optimeeritud konkreetsete keskkonnatingimuste jaoks, kõige levinumate strateegiatega puhul võib esile tõsta jalgmehhanismid ja rattad maapealse ning sõukruvid veealuse liikumise jaoks. Antud liikumislahenduste efektiivsus väheneb keskkonnatingimuste muutudes. Keskkonnatingimuste muutumise mõjul väheneva jõudluse leevendamiseks on uuritud alternatiivseid liikumisviise, mis hõlmavad mitmetraditsioonilisi tehnilisi lahendusi ning pehmeid materjale. Kuigi täiturmehhanisme, mis suudavad oma jäikust ja kuju dünaamiliselt reguleerida, on läbi aastate uuritud paljudes rakendustes, on allveerobotikas selles osas märkimisväärne mahajäämus.

Antud väitekiri uurib eeldust, et hübriid- ja mitmetraditsioonilised täiturid, mis koosnevad muutuva jäikusega ühilduvatest osadest, võivad olla tõhusad liikumiseks varieeruvates keskkonnatingimustes ja liikumisstsenaariumides. Hüpotees seisnes selles, et muutuva jäikusega aktuaatorite kasutamine võimaldab ümberkonfigureerimist, mis võib parandada täiturmehhanismi jõudlust ning võimaldada liikumist veealustes ja mitmefaasilistes keskkondades, tõstmata seejuures juhtimisloogika ja liikumise planeerimise keerukust. Sel eesmärgil töötati välja kolm prototüüpi, et eksperimentaalselt uurida täiturmehhanismide morfoloogiat ja materjali valikut. Kahe esimese prototüübi näol oli tegemist pehmete osadega täiturmehhanismidega, millel on ebaühtlane jäikus ja mille rakendamisel keskenduti veealuse tõukejõu vektorite uurimisele. Eksperimentaalne hindamine näitas, et kuigi ebaühtlane jäikusprofiil parandas oluliselt täiturmehhanismide jõudu ja tõhusust, vähendas see mõnevõrra roboti liikumismustrite repertuaari ja ulatust. Kahe esimese uurimistöö tulemuste põhjal laienes töö liikumisele vaheldusrikastes keskkonnatingimustes, uurides amfiibset liikumist muutuva jäikusega täituriatega. Kolmas prototüüp, mis põhines kuju ja jäikuse ümberkonfigureerimist võimaldavatel materjalidel ja disainil, demonstreeris multi-modaalset liikumist vee- ja maismaatingimustes, samuti märjal vesisel pinnasel, mis imiteerib üleminekut vee- ja maapealse liikumise vahel.

Antud töös demonstreeriti liikumist erinevates veealustes ning amfiibsetes stsenaariumides. Võrreldes enamiku olemasolevate muutuva jäikusega ning juhitava tõukejõuga täituriatega, eriti multimodaalse amfiibliikumise jaoks mõeldutega, on kõigi selles lõputöös esitatud prototüüpide mehaaniline keerukus, samuti juhtimisloogika ja liikumise planeerimisenõuded tähendusrikkalt madalad. Lisaks, kuigi enamikes amfiibliikumise rakendustes kasutatakse jäiki ja kiiresti liikuvaid komponente, mis võivad olla täiturmehhanismidele ja ümbritsevale keskkonnale kahjulikud, põhinesid antud töös esitatud lahendused peamiselt pehmetel komponentidel, avaldades keskkonnale seeläbi minimaalset mõju.

Käesolev väitekiri loob aluse edasisteks arendusteks täiturmehhanismide jõudluse tõstmiseks liikumaks väljakutseid pakkuvates keskkonnatingimustes. Nende meetodite eksperimentaalne uurimine ja analüüs annab sügavama ülevaate nende eelistest ja piirangutest.

See võib aidata tuvastada ja edasi arendada tehnoloogiaid, mis praegu antud valdkonnas arenguid aeglustavad, suurendades lõpuks seeläbi neid tehnoloogiaid kasutavate robotite tööautonoomiat. Lisaks julgustab demonstreeritud madal keskkonnale avaldatav mõju ning vähene häiring muutuva jäikusega täiturite laiemat kasutuselevõttu rakendustes, mis nõuavad minimaalset keskkonnamõju. Lõpuks saab muutuva jäikusega aktuaatorite arendusi üle kanda ka teistele robotika valdkondadele peale liikumise, näiteks haaramise või taastusravi rakendustele.

List of Publications

This Ph.D. thesis is based on the following publications that are referred to in the text by Roman numbers.

- I R. Gkliva, M. Sfakiotakis, and M. Kruusmaa, "Development and experimental assessment of a flexible robot fin," in 2018 IEEE International Conference on Soft Robotics (RoboSoft), vol. 1, pp. 208–213, IEEE, 2018
- II A. Simha, R. Gkliva, Ü. Kotta, and M. Kruusmaa, "A flapped paddle-fin for improving underwater propulsive efficiency of oscillatory actuation," IEEE Robotics and Automation Letters, vol. 5, no. 2, pp. 3176–3181, 2020
- III R. Gkliva and M. Kruusmaa, "Soft fluidic actuator for locomotion in multi-phase environments," IEEE Robotics and Automation Letters, vol. 7, no. 4, pp. 10462–10469, 2022

Other Related Publications

This work is also published/presented in adjacent fields but does not form a main part of this thesis.

- 1 M. Kruusmaa, R. Gkliva, J. Tuhtan, A. Tuvikene, and J. Alfredsen, "Salmon behavioural response to robots in an aquaculture sea cage," Royal Society open science, vol. 7, no. 3, p. 191220, 2020
- 2 W. Remmas, R. Gkliva, and A. Ristolainen, "Dynamic modelling of a screw actuator for improved locomotion control on various terrains." EGU General Assembly 2022, Vienna, Austria, 23-27 May, EGU22-5726, <https://doi.org/10.5194/egusphere-egu22-5726>, 2022

Author's Contributions to the Publications

- I In [Publication I], I was the main author; defined the research problem, designed the prototype, planned and carried out the experiments, analysed the results, and wrote the manuscript
- II In [Publication II], I was co-first author; designed and fabricated the prototypes, proposed a mathematical model for the actuator, designed and developed the data acquisition setup, planned and carried out the experiments, analysed the results, prepared all the figures and co-wrote the manuscript.
- III In [Publication III], I was the main author; defined the research problem, designed and fabricated the prototype, created a model of the actuator and ran simulations, developed the data acquisition setup, planned and carried out the experiments, analysed the results, and wrote the manuscript.

Abbreviations

BCF	Body Caudal Fin
CAD	Computer Aided Design
DAQ	Data Acquisition
DOF	Degree of Freedom
FEM	Finite Element Method
IMU	Inertial Measurement Unit
MCU	MicroController Unit
MPF	Median Paired Fin
PID	Proportional Integral Derivative
ROS	Robot Operating System
SMA	Shape Memory Alloy
U-CAT	Underwater Curious Archaeology Turtle
UUV	Unmanned Underwater Vehicle
VSA	Variable Stiffness Actuator

Introduction

In the past few decades, robot locomotion in unstructured and uncertain conditions has gained considerable interest in the academic, research, and industrial robotics communities. Stemming from the growing number of applications related to the exploration, the protection and the sustainable exploitation of the planet's natural resources, this interest has resulted in an ever-increasing number of studies and development of robots that can negotiate locomotion in a variety of aquatic, terrestrial and mixed conditions. This field aims to reduce danger to human operators and to potentially extend the operational capabilities of relevant missions. Most mobile robots employ highly specialized locomotion strategies that have been optimized for narrow operational specifications, most notably using wheels, tracks, or legs for terrestrial locomotion [6], and propellers or lift-based control surfaces for swimming [7]. The performance of these methods can be high in their intended applications, but diminishes when locomotion is required in varying environmental conditions with high uncertainty, such as in the transition between aquatic and terrestrial locomotion. In order to address these limitations, alternative approaches have been introduced, featuring combinations of different actuation modalities, as well as reconfigurable and hybrid designs. However, most of these strategies include mechanically complex, rigid, fast-moving parts, which can have negative effects on locomotion performance and on their interaction with the surroundings.

A strategy often used to mitigate some of these risks is to incorporate compliant components in the robot's locomotion system. Some of the most popular materials used for this purpose belong to the group of rubber silicones. These materials can withstand and recover from large strains and deformations, they demonstrate safer interaction with the surroundings, and can store and release energy due to their elastic behaviour. While these characteristics can greatly benefit an actuation system, the use of compliant materials can also include drawbacks related to low positional accuracy, low force output, and challenging state estimation, as traditional sensing and actuation methods are not straightforward to adopt when using these materials.

In this context, the goal of this work was to develop new kinds of adaptable soft actuators, as well as their motion planning and control algorithms, to enhance the mobility of underwater and terrestrial robots in environments potentially consisting of both solids and fluids, ranging from completely submerged underwater swimming, to terrestrial locomotion on wet or dry granular terrains. The work to achieve this goal was driven by the hypothesis that the soft actuator's morphology and stiffness profile can enable a passively or actively reconfigurable mechanism that will allow multi-modal actuation, appropriate for locomotion in this wide range of environments. The expected outcome was that implementing a mechanism that can permanently or temporarily adjust the stiffness in a compliant actuator, will allow taking advantage of the benefits that are associated with using a compliant material, while at the same time reducing the negative effects of compliance by selectively increasing the actuator's stiffness.

With this purpose, this dissertation focuses on the empirical investigation of locomotion methods in aquatic and terrestrial environments, using compliant actuators with variable stiffness. The investigation approaches the problem from different points of view in each environmental setting, studying the effects that the actuator's morphology and material can have to its force output and to its energetic characteristics. For this purpose, a series of actuator prototypes were designed, fabricated and used to experimentally evaluate different modes of locomotion in aquatic and terrestrial conditions.

While the aim was to maximize the proposed actuators' force output and energetic efficiency, the design process included additional criteria relating to the prototypes' ease of

use and fabrication. The first criterion was to increase the actuators' force output without increased motion planning and control requirements. This guideline informed the design choices on actuator morphology and material selection. The second criterion was to keep the fabrication method simple, accessible, and low-cost. For this reason, the prototypes were fabricated using a commercially available silicone rubber, 3D printed parts, and miscellaneous commonly available components.

The knowledge gained from this thesis can help advance the study of underwater and amphibious locomotion with compliant and variable stiffness actuation. Specifically, this work provides the following main contributions:

- **The design and fabrication of a series of actuator prototypes that feature a variety of stiffness profiles: constant or variable, and stiffness adjustment methods: passive or active.** Each prototype allowed to investigate the stated hypothesis from a different viewpoint, providing a more well-rounded overview of the investigated problem. It also allowed to identify the challenges and solutions related to design and fabrication.
- **The experimental parametric analysis** of each of the prototypes' output and energetic characteristics over a range of kinematic inputs. This type of analysis helped reveal the advantages of the methods, as well as their limitations.
- **A simplified force model for the actuator described in [Publication II], and its experimental validation.** Despite the simplified way that the drag coefficient was calculated, the model follows the experimental data quite closely, and can be used for designing model-based control strategies, as well as for simulations.
- **The material model selection and parameter identification for the soft material (silicone rubber) used throughout the thesis, and experimental validation of the model.** Given the challenges of modelling the deformation of complex shapes and hyperelastic materials with limited experimental data, the model identification and validation made simulations possible and allowed the design process described in [Publication III] to converge to a successful prototype.
- **The actively reconfigurable actuator design described in [Publication III], and experimental proof-of-concept of multi-modal amphibious locomotion.** This prototype can serve as a starting point for further development of variable stiffness actuators, as well as for related technologies that can increase the operational autonomy of these systems, such as the miniaturization of systems that provide power and pressure.

The main content of this thesis is divided into two parts, focusing on the investigation of locomotion using a series of actuators that demonstrate variable stiffness profiles. The first part, contained in Chapter 2, provides an investigation of underwater thrust vectoring, using variable stiffness actuation. The focus of this work was to study the effects of passively modifying a soft actuator's stiffness profile and shape. For this purpose, two different prototypes are proposed, leveraging material and design properties to study their effects to actuator force output. The experimental evaluation of the actuator output provides insight into how the stiffness profile of a compliant actuator can affect the generated forces and energetic characteristics.

The second part, in Chapter 3, expands on the findings of the work described in the first part, and provides an investigation of amphibious locomotion via multi-modal actuation. A novel actuator prototype is presented that allows shape and stiffness adjustment.

This enables two different motion patterns for locomotion in aquatic, terrestrial and multi-phase environments, using a rather straightforward stiffness adjustment mechanism and simple motion planning and control schemes.

The above-mentioned parts are preceded by a background literature review, in Chapter 1, that gives an overview of the existing literature in soft and variable stiffness actuation for underwater and amphibious locomotion. This helps highlight the motivation and the scientific importance of the work described in this thesis.

1 Background

Over the years there has been a growing demand for remote access in environments with varying levels of locomotion complexity, stemming from our need for exploration, as well as from the always increasing number of applications that relate to the study, the protection and the sustainable exploitation of natural resources. These environments range from rocky or granular, dry or wet terrains, to fully submerged aquatic environments [8]. This demand has triggered an increase in the development and study of robotic vehicles that can negotiate locomotion in these challenging environmental conditions [6].

Traditional methods of terrestrial locomotion include wheels and tracks, with legged configurations gaining in popularity [6]. Aquatic locomotion counterparts include combinations of propellers and lift-based control surfaces or multi-thruster systems [7]. These methods have a proven record of highly efficient and agile locomotion in their respective applications. However, their performance declines significantly when manoeuvring is needed in unstructured, unstable environments, as well as when transitioning through drastically different environments. To mitigate the diminishing performance of locomotion in these conditions, the research community is exploring alternative methods of locomotion, including non-traditional hybrid designs [9, 10] and compliant materials [11, 10].

The following sections offer an overview of technologies that enable robot locomotion in aquatic and terrestrial conditions, by exploring relevant implementations from published literature. This overview contains and expands on background information from [Publications I, II, and III]. Section 1.1 gives an overview of methods for robot locomotion in aquatic environments, focusing on non-traditional bio-inspired methods. Section 1.2 extends the review to cover amphibious locomotion, including reconfigurable rigid and soft actuators that have been implemented for locomotion in mixed, i.e., aquatic and terrestrial, conditions, to highlight the effect of using compliant components for locomotion. A review on implementations of variable stiffness actuation for locomotion in aquatic, terrestrial, and mixed conditions is given in Section 1.3, and aims to narrow down to use cases related to the topic of this thesis.

1.1 Robot locomotion in aquatic environments

Agility, energy efficiency, and stealth operation are characteristics of great importance for robots working in aquatic environments. These attributes become increasingly important when precise manoeuvring in confined spaces, stable station keeping and orientation control in the presence of drifting currents is needed, as well as in applications that require minimal sediment disruption and low environmental impact. These requirements are critical during missions for underwater archaeology, shipwreck exploration, submerged pipeline inspection, inspection and maintenance of offshore energy installations [12], studying fish behaviour [13, 4], and many others.

Marine locomotion can be split into two main categories [14]: surface swimming, where only part of the robot is submerged, and fully submerged swimming, where the entire robot is submerged, with methods of locomotion for robots in either category varying significantly. As in this thesis the focus was on the latter category, the review in this section reflects that choice.

1.1.1 Bio-inspired underwater locomotion

Traditional methods for underwater locomotion, namely, lift-based control surfaces and multi-thruster configurations, show diminishing performance in the conditions described above. One of the strategies the research community uses to overcome these challenges is

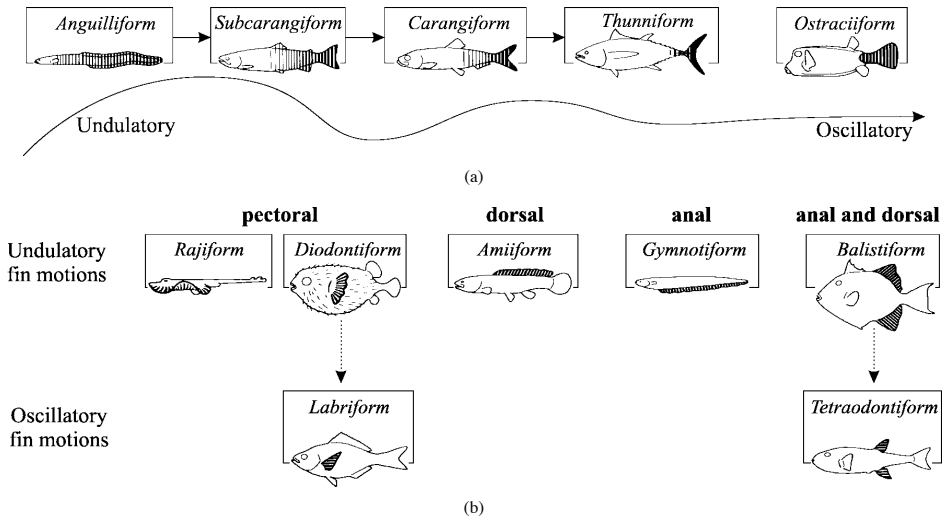


Figure 1.1: Classification of fish swimming modes: (a) body and/or caudal fin (BCF) propulsion, (b) median and/or paired fin (MPF) propulsion. ([18] ©1999 IEEE)

drawing inspiration from nature, to develop novel, bio-inspired actuators for underwater robots [15, 16, 17].

Bio-inspired propulsion designs for robotic underwater vehicles follow two main paradigms, seen in Fig. 1.1. Vehicles from the first category emulate the continuously flexing fish bodies for increased propulsive efficiency [19, 20, 21, 22, 23, 24, 25] following the *body and/or caudal fin* (BCF) locomotion class [18, 26], and the second employs mechanical analogues of biological active appendages [16, 27]. Most of the systems in the second category include either pectoral or lateral, pitching or heaving fins [16, 28, 29, 30, 31, 32, 33, 34, 35, 36], based on the morphology and functionality of the fins and paddles of marine species that use *median and/or paired fin* (MPF) locomotion method [18, 26], and have the potential to increase the robot's thrust vectoring capacity and energy efficiency, while maintaining a stealthy operation [16]. Other bio-inspired underwater locomotion methods include jet-propulsion systems, inspired by the locomotion of animals such as jellyfish, scallops, and octopus [37, 38, 39, 40].

While some of the actuators for aquatic locomotion described in this section consist of only stiff components [24], and some of only soft components [25, 41], the majority consist of a combination of stiff and soft parts [23, 42, 33, 43, 44].

1.2 Amphibious robot locomotion

This section extends the literature review to actuators for amphibious locomotion. It includes prototypes that employ rigid, soft, as well as combinations of rigid and soft components, to negotiate locomotion in aquatic, terrestrial, and multi-phase conditions. This topic is quite narrow as not many implementations have been successful in demonstrating effective locomotion in such a diverse range of conditions. For this reason, both underwater and surface swimming prototypes are included here. This section uses material from [Publication III].

In one of the first successful implementations of amphibious locomotion, the RHex vehicle demonstrated exceptionally agile locomotion negotiating terrains of varying com-

plexity, using a C-shaped compliant leg design [45]. This work was instrumental in the field of robotic amphibious locomotion, and resulted in the development of a series of actuators and robots using appendages that resemble wheels or curved legs, and compliant flippers. The Aqua robot demonstrated underwater and terrestrial walking as well as swimming, using two sets of actuators: C-shaped legs and flat blades, that can be manually switched for each locomotion mode [46]. Bridging these two configurations, mechanically reconfigurable actuators that can dynamically switch forms between curved leg or wheel, and flat fin [47, 48, 49], have been used to investigate locomotion in a variety of aquatic and terrestrial environments. A different robot design featuring a crab-like form demonstrated a variety of gaits for underwater swimming, walking on land and on the seabed using a combination of legs and paddles [50], featuring a total of 24 joints in its limbs.

Mechanically simpler mechanisms, that employ underactuated and partially passive configurations, have also successfully demonstrated amphibious locomotion. The “ninja-legs” design, combining a circular 1-DOF leg and a flat flipper [51], and a similar actuator comprising a stiff fan-shaped leg and a flipper with manually variable stiffness [52] have demonstrated locomotion on terrestrial and aquatic environments. The Whegs™ design, comprising a series of legs around a rotating shaft, was used to demonstrate walking and overcoming obstacles in unstructured terrestrial environments and in surf areas, as well as surface swimming [53, 54]. The RobotTerp quadruped [55] demonstrated the transition between walking on land and swimming on the water surface, using stiff legs with a grate-like morphology, covered by a compliant flap, that transforms the legs into paddles and passively optimize drag forces during swimming. A flat paddle 1-DOF mechanism with a passive elastic hinge enabled underwater walking and swimming for the PEAR hexapod [56].

1.2.1 Soft actuators for amphibious locomotion

The strategies mentioned above have been rather successful in demonstrating locomotion in a diverse range of amphibious conditions. However, to negotiate the uncertainty of moving through different media, they rely on rigid, and/or fast moving parts. This can be damaging to the environment or to the robot itself, and can generate large unwanted accelerations in the robot’s motion. Additionally, the combination of rapid impacts of rigid actuators on granular and deformable terrains can have negative effects on locomotion performance, resulting in reduced traction or the actuators digging into the ground, thus reducing energetic efficiency and increasing instability.

Integrating compliant parts into locomotion mechanisms can introduce benefits such as increased safety when interacting with the environment, the ability to store and release energy through passive elastic components, as well as improved quality of motion when negotiating unstructured environments [10].

In recent years there have been only a few examples of soft materials being used to fabricate completely or partially soft robots aimed at studying amphibious locomotion. A variable stiffness material-pneumatic prototype [57] was used to investigate the dynamic switch between leg and flipper form by adjusting the temperature and internal pressure of its components. Despite its slow transition and actuation mechanisms, this method shows promising results mostly due to the decoupling of stiffness and shape. A sea urchin-inspired amphibious robot using actuated rigid spines and extensible soft legs was used to investigate bio-inspired locomotion patterns in aquatic and terrestrial conditions [58]. A quadruped robot comprising groups of interconnected thin and soft McKibben actuators demonstrated locomotion on wet and dry terrains, using a variety of walking and crawling gaits [59]. A worm-inspired soft robot, featuring serially connected and individually

driven pneumatic actuators, was used to investigate crawling and swimming gaits [60]. A vibration-based actuator that comprises rigid and compliant parts was used to drive a miniature amphibious robot that employs a combination of legs and fins to achieve terrestrial and aquatic locomotion [44]. An SMA-driven bistable soft actuator, leveraging a snap-through instability to rapidly transform between two states, was used for amphibious locomotion [61]. Three tethered prototype robots were used to demonstrate a variety of locomotion modes, amphibious locomotion, crawling and jumping, and crawling and rolling caterpillar-like motion.

The works described in this section highlight the challenges of transitioning between aquatic and terrestrial conditions. As each mode of locomotion has specific requirements that are not applicable to other modes, the transition between environments can present challenges that need to be addressed. For example, as shown in Section 1.1, efficient swimming can be achieved easily with soft underactuated limbs performing slow motions, however the same actuators and motion patterns wouldn't be very successful on land.

1.3 Locomotion using variable stiffness actuation

Based on the findings of the previous sections, this section explores implementations of actuators with adjustable stiffness components, and how they address locomotion in each of the target environments: aquatic, terrestrial, and mixed. As mentioned previously, most traditional robot locomotion mechanisms include rigid, and/or fast moving parts, that can be damaging to the surrounding environment, or to the robot itself, and can generate large unwanted accelerations in the robot's motion.

Specific to locomotion, the rapid impacts of rigid actuators can negatively affect performance, when moving on granular and deformable terrains, or on low-traction surfaces, resulting in unstable locomotion or the actuators digging into the ground. Integrating compliant parts into locomotion mechanisms can introduce benefits such as increased safety when interacting with the environment and with humans [11], the ability to store and release energy through passive elastic components, as well as improved quality of motion and adaptability when negotiating unstructured environments [10, 11].

While using soft materials can benefit actuator systems, it also has drawbacks and challenges [62, 63], with some of the most notable being the difficulty to achieve high positional accuracy and force output, the challenge of adopting traditional sensing methods for position feedback, and the increased modelling and control requirements due to the nonlinear behaviour of soft materials. The research community has been investigating variable stiffness actuators (VSA) to address some of these challenges. The following subsections provide an overview of locomotion strategies for aquatic, terrestrial and mixed conditions, that use variable stiffness materials or mechanisms.

1.3.1 VSA for aquatic locomotion

Most aquatic locomotion implementations of VSA found in literature are actuators with shape or function inspired by fish locomotion. These include caudal fins actuated by fin-rays with variable stiffness, used to investigate a variety of kinematic patterns [64], bilateral pneumatic actuators [65, 66], as well as bistable pneumatic actuators [67], and a tendon-based VSA mechanism for propulsion of a dolphin-like robot [68, 69].

Additionally, undulatory motion is also investigated using VSA with active and/or passive fin-rays [70, 71]. Paddle-like mechanisms using a variable stiffness stem were used to investigate propulsion [72, 73]. Lastly, a flea-like mechanism comprising composite and SMA materials for jumping on water surface was used to investigate locomotion on the water surface [74].

1.3.2 VSA for terrestrial locomotion

Terrestrial locomotion strategies with VSA include walking, crawling, and rolling using a wide variety of stiffness adjustment mechanisms. An implementation of a walking mechanism using a spring-pulley system with variable pretension and spring length for adjusting the stiffness of a leg mechanism was used to investigate biped running [75]. A compliant spine mechanism was used to dynamically modify the stiffness of the C-shaped legs of a hexapedal robot [76]. Locomotion on deformable ground was investigated using a legged robot with stiffness and shape change through granular jamming [77].

Crawling-inspired locomotion has been investigated using a variety of technologies and methods, including peristaltic motions, leg-like appendages, as well as shape-memory alloy (SMA) materials. A combination of cable-driven reconfigurable leg-wheels and a tail was used to investigate crawling over obstacles [78]. A spring-loaded pneumatic actuator exploiting the bistability of snap-through was used to investigate high-speed crawling motions [67]. A robot using an internal pendulum in combination with inflatable bladders, was used to investigate crawling through vibration and hopping-based motion patterns [79]. Tendon and SMA-driven worm-like prototypes [80] and peristaltic motion SMA coil actuator [81] were used to investigate crawling. A pneumatic inchworm-like actuator was used to achieve locomotion of a differential-drive soft robot [82]. Other examples for VSA-based terrestrial locomotion include individually jammed surface elements of a soft robot [83], as well as a cable-driven tensegrity structure [84] that achieves a rolling motion.

1.3.3 VSA for amphibious locomotion

As locomotion in aquatic and in terrestrial conditions requires vastly different motion patterns and actuator characteristics, the traditional rigid and soft actuation methods seem to be insufficient in most cases. In this context, VSA-based locomotion systems are being investigated, aiming to find materials, designs, or motion patterns that can perform well in a variety of environmental conditions. This area of research is not well developed, however, literature shows that effort towards it is increasing.

An amphibian suction-based VSA was used to investigate climbing on smooth and semi-smooth surfaces [85]. The following strategies were used to achieve combinations of swimming and walking motions. A hexapod robot with actuators that can operate as stiff legs, or as variable stiffness flippers, was used to investigate walking and swimming-based locomotion in a variety of terrestrial and aquatic conditions, as well as to transition through mixed environments [86]. A reconfigurable fin-leg actuator for amphibious locomotion, using an embedded heater that triggers switching between soft and stiff states was used to demonstrate proof-of-concept of the morphing limb [57]. A tethered vehicle using this prototype was later used to demonstrate multi-modal locomotion in aquatic and terrestrial conditions [87].

1.4 Conclusions

This chapter provided a brief overview of the literature related to technologies investigated in this thesis. To summarize, the research fields of aquatic and amphibious robot locomotion were studied, focusing on use cases employing soft and variable stiffness actuation, in order to identify common technologies and strategies that have been previously successful, as well as to highlight research gaps that were subsequently investigated in this work. This analysis gives insight into this topic, regarding its potential for use in locomotion-related applications, as well as the challenges and limitations that it may present. Additionally, studying the methods of design, fabrication, and control from these implementations, helped guide the work described in the following chapters.

A variety of mechanisms and materials have been investigated for implementing variable stiffness actuators. The field of amphibious robot locomotion is still not very well developed, with very few examples of variable stiffness actuators present in literature. Most of the examples in this field include early stage prototypes with limited operational autonomy, that rely on external power, pressure and control. As the field advances, supplementary technologies will also mature, allowing energetic and operational autonomy to increase. This would in turn allow the development and testing of more robust and capable locomotion systems. In this context, the design choices made in this work were aimed at high robustness and simpler and more accessible implementation and use.

Background information for specific methods that were used, as well as for the motivation behind design choices, can also be found in Chapters 2 and 3.

2 Underwater thrust vectoring

This chapter discusses the development and study of actuators with variable stiffness, for underwater thrust vectoring. The motivation to investigate these types of actuators originates in the hypothesis that varying the stiffness of a soft actuator can help optimize their force output and energetic characteristics, without increasing the requirements for motion planning and control. In this context, the investigation of two methods of underwater thrust vectoring using variable stiffness actuators is presented here.

The work described in [Publication I], is investigating the use of non-uniform stiffness profiles in soft actuators. For this purpose, a modified version of an existing soft actuator was developed and experimentally tested. The experimental comparison between the original and the proposed actuators offers some insight into how the stiffness profile affects the generated forces and energetic efficiency.

The work described in [Publication II] is investigating the passive adjustment of stiffness and shape in soft actuators for underwater thrust vectoring. A novel actuator prototype is introduced, that passively switches its stiffness profile depending on its direction of motion. An experimental assessment of the actuator's generated forces serves as proof-of-concept of the actuator's design. The actuator's efficacy for locomotion is evaluated via a series of experiments. In the following subsections, the two thrust vectoring methods are presented and discussed.

2.1 Leveraging actuator stiffness profile to manipulate force direction and magnitude

In this section we discuss how a soft actuator's stiffness profile can affect the direction of generated forces, as well as the energetic characteristics of motion. The work described in this section was partially published in [Publication I]. The actuator of the U-CAT robot [88] was used as a test case.

U-CAT (Fig. 2.1) is a small-scale, low-cost, underwater robot designed for exploration of shipwrecks and underwater structures [89]. The robot was developed at the Centre for Biorobotics, TalTech, in the context of the ARROWS project [88]. For locomotion, it employs four individually actuated soft flippers that are arranged in a configuration that can achieve holonomic motion in 6-DOF [90]. This method of locomotion allows agility in confined spaces, with minimal disturbance of sediments.

Each of the robot's actuators can generate a force vector by oscillating around its motor shaft, following a sinusoidal motion pattern. The soft fin has two planes of symmetry,

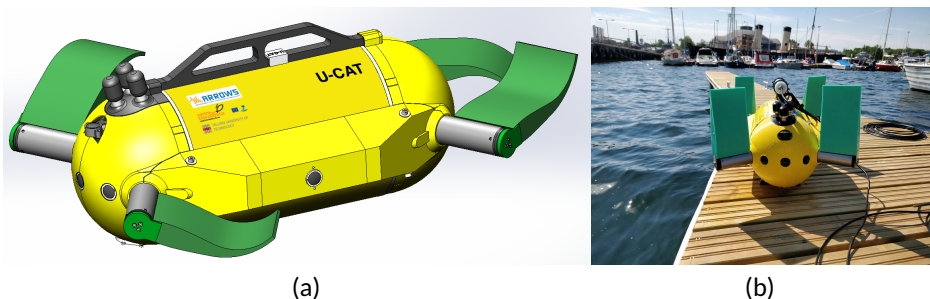


Figure 2.1: The U-CAT robot: (a) CAD model of the robot (Here, the fins are illustrated in a deformed state), (b) physical prototype.

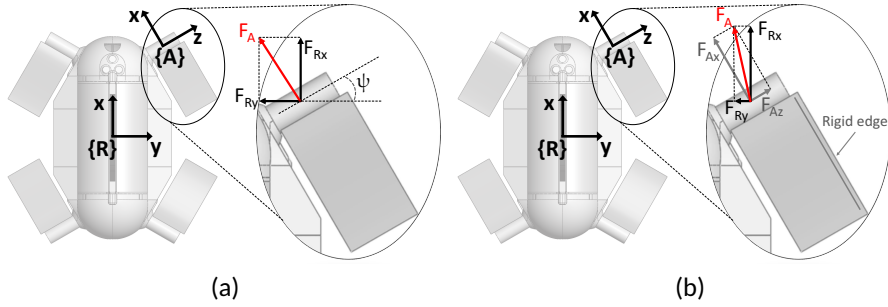


Figure 2.2: Illustration of generated forces on U-CAT's fins for comparison between the original and proposed actuators ([Publication 1]©2018 IEEE). (a) Original fin: the overall vector F_A of the generated force is in the direction of the x -axis of the fin frame {A}. (b) Proposed fin: the overall vector F_A of the generated force involves components on both the x - and z -axis of the fin frame {A}, thereby increasing the force along the x -axis of the robot frame {R}.

both parallel to its longitudinal axis. Because of this symmetry, if the motion pattern is a symmetric oscillation, the force vector is generated along the direction parallel to the fin's longitudinal axis, and the phase-averaged force vector is generated along the direction coinciding with the reference of oscillation (Fig. 2.2a). The reference of oscillation of the sinusoidal motion pattern can be set to any angle around the motor axis. This means that the generated force can be directed towards any angle on an axis normal to the motor shaft, by controlling the reference angle of oscillation. The four, independently targeted force vectors can be used to propel the robot in any direction.

2.1.1 Fin design and fabrication

Similar to how fish swim, while actuated with an oscillatory motion pattern the fin deforms into a backward-propagating wave (Fig. 2.3a, bottom), generating a force vector opposite in direction to this wave (Fig. 2.2a). We hypothesized that by changing the stiffness profile of the fin, it would result in a different bending profile during actuation. Specifically, we

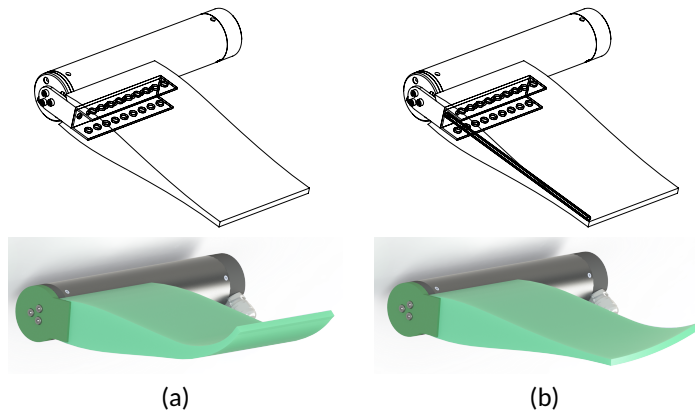


Figure 2.3: CAD model of the studied U-CAT fins ([Publication 1] ©2018 IEEE), illustrating their internal structure (top) and expected deformation profile (bottom) during an oscillatory motion pattern: (a) Original fin. (b) Modified fin (rigid bar is visible near the outside edge).

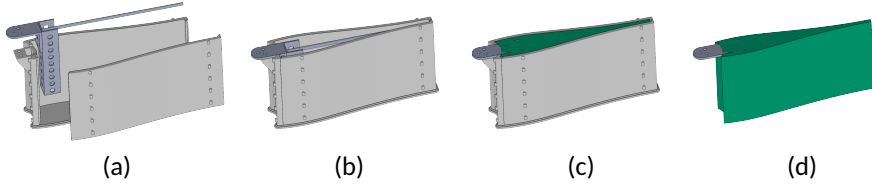


Figure 2.4: Illustration of the fabrication process of the proposed fin: (a, b) A metal frame is assembled into the two part 3D-printed mould. (c) Silicone compound is mixed and poured into the mould, and allowed to set. (d) The cured actuator is removed from the mould.

selected to create a deformation profile similar to what is seen in Fig. 2.3b, bottom. Due to the modified, non-symmetric bending profile, the generated force vector's direction will also change to be not parallel to the fin's longitudinal axis (Fig. 2.2b). To investigate this claim we introduced a rigid component to U-CAT's soft fin (Fig. 2.3b, top). By adding the stiff component on the fin's edge (Fig. 2.2) we expected the wave to be propagated at an angle between the two rigid edges of the fin, diverted away from the direction of the added rigid component, resulting in a force vector angled towards the actuator's z axis.

Fig. 2.4 shows an illustration of the fin fabrication process, using a two-part mould. Initially, a metal frame is assembled that includes an aluminium bracket that attaches to the motor shaft, a perforated aluminium profile that allows the silicone to attach to the metal frame, and a rigid bar that will increase the stiffness in that part of the actuator. This metal frame is assembled into the two part 3D-printed mould (Fig. 2.4(a, b)). Silicone compound is mixed and poured into the mould (Fig. 2.4c). After curing, the mould parts are separated and the actuator is removed (Fig. 2.4d).

2.1.2 Oscillatory motion pattern and control

To generate the propulsive force, an oscillatory motion pattern was achieved by prescribing a sinusoidal trajectory with amplitude A and frequency f to the motor that the actuator is mounted on, as:

$$\theta(t) = \frac{A}{2} \sin(2\pi ft) + \phi, \quad (1)$$

where, the offset parameter ϕ allows to orient the fin oscillations, and subsequently the generated forces, to a specific angle.

Fig. 2.5 shows the control scheme employed for the actuator's oscillatory motion. This scheme was implemented in Maxon's EPOS2 Module 36/2 as a position controller using "Profile Position Mode" [91]. This structure employs a position PID controller with a current PI controller as subordinate regulator. The input to this controller, the target position,

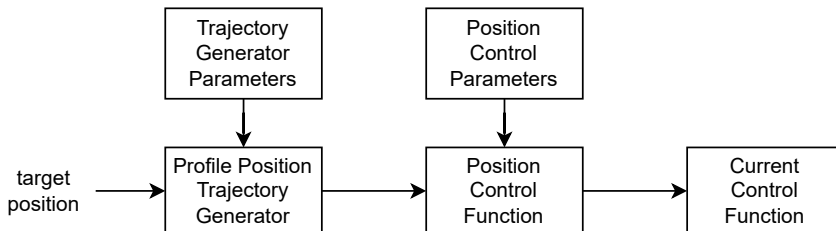


Figure 2.5: Position control structure for oscillatory pattern [91, 92].

is generated at regular intervals based on the sinusoidal motion profile described in (1). More details on the available controller functions of the Maxon EPOS2 Module 36/2 and how the selected controller scheme was implemented can be found in Section III-A of [Publication III]. All controller gains and feedforward factors were tuned using the "regulation tuning wizard" in the Epos Studio software.

2.1.3 Experimental characterization of forces

The actuator's efficacy related to generating underwater propulsive forces was evaluated via a series of experiments, focusing on the measurement of forces generated by in-place oscillations around a motor shaft (Fig. 2.6). Additionally, to studying the proposed actuator's force output, the original U-CAT actuator was used as a baseline of comparison for the force and efficiency metrics. For this reason, two sets of experiments were conducted, using both an 'original' and the 'modified' actuator in identical conditions.

The actuator was mounted on a waterproofed BLDC motor (EC-max 30 by Maxon Motors) driven by an EPOS2 36/2 motor controller, as seen in Fig. 2.6a and 2.6b, and was fully submerged in a water tank during the experiments. The data acquisition system and a diagram of the experimental setup can be seen in Fig. 2.6a.

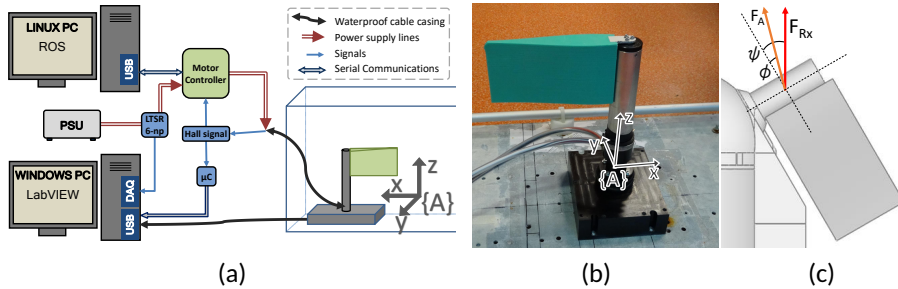


Figure 2.6: Experimental setup and data acquisition system ([Publication I] ©2018 IEEE): (a) Diagram showing the experimental setup and data acquisition system, (b) The modified fin prototype with its motor, mounted on a custom force sensor, (c) The resulting force vector F_A and how it contributes to the robot's surge.

The collected data was filtered to reduce noise, and averaged values were calculated for the force and current consumption. The generated force's contribution to the robot's surge F_{Rx} was also calculated based on (2).

$$F_{Rx} = F_A \cos(\psi - \phi) = \left(\sqrt{F_{Ax}^2 + F_{Az}^2} \right) \cos\left(\tan^{-1}\left(\frac{F_{Az}}{F_{Ax}}\right)\right) \quad (2)$$

All averaged values were calculated for a number of whole periods, to account for periodic phenomena, and excluding an initial transient effect which showed increased current consumption. As the actuator base was fixed in place, and the water in the tank was still, the static thrust/power ratio (N/W) was used as an indirect metric of the actuator's propulsive efficiency, based on [93].

$$\eta = \frac{\bar{F}_p}{\bar{P}_{in}} = \frac{1}{nT} \frac{\int_0^{nT} F_p(t) dt}{\int_0^{nT} VI(t) dt} \quad (3)$$

Fig. 2.7 shows indicative results of both the original and the proposed actuator, under the same kinematic parameters. The top graph shows the temporal evolution of the

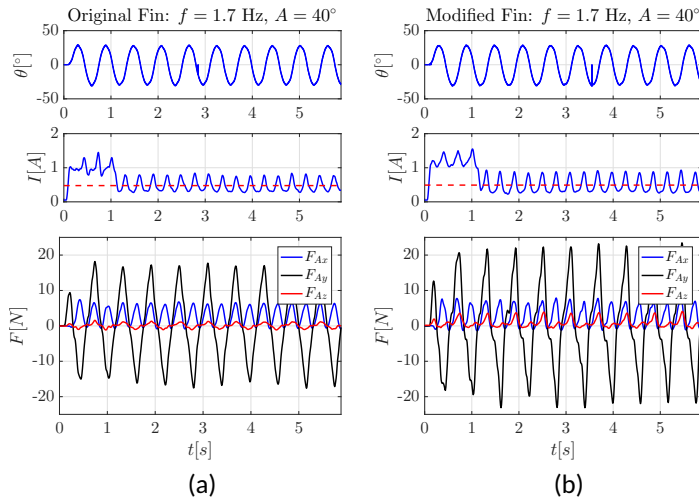


Figure 2.7: Indicative experimental results with U-CAT fins, including position feedback (top), instantaneous and mean current consumption (middle) and generated forces (bottom) along 3 primary axes ([Publication 1] ©2018 IEEE): (a) original fin, (b) modified fin

motor shaft's angular position. The middle graph shows the instantaneous current consumption with blue colour, and the phase-averaged current consumption with the red dashed line. The bottom graph shows the generated forces along the three primary axes.

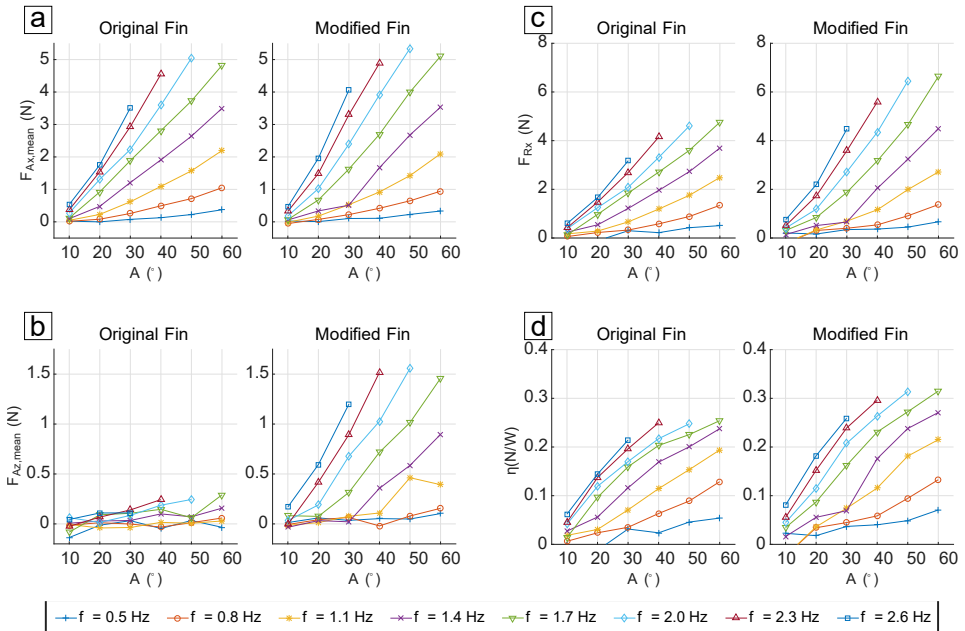


Figure 2.8: Parametric study of forces for a range of amplitudes and frequencies of oscillation with original and modified U-CAT fins, (adapted from [Publication 1]): (a) x-axis force component, (b) z-axis force component, (c) calculated force contribution to the robot's surge (F_{Rx}), (d) calculated thrust/power ratio.

The generated force and current consumption of the two actuators follow very similar patterns. The main difference between them is the increased output force in the z direction for the modified actuator, demonstrating that the generated force direction has a different direction compared to that of the original actuator. Additionally, despite the larger magnitude peaks seen in the lateral force component F_{Ay} , it should be noted that this force is symmetric around 0 and produces no net amount of force throughout the actuation cycle.

Fig. 2.8 shows the aggregated results of the parametric study, for the full range of kinematic parameters, A and f , for both the original and modified actuators. The two graphs on the left (a, b) show the averaged force components along the x and z primary axes. They show that the modified fin generates a force vector that is not parallel to its longitudinal axis, validating our hypothesis that the asymmetric stiffness profile would divert the generated force vector towards the z axis. This redirection of the force vector shows as increased contribution to the robot's surge force (Fig. 2.8c), as well as increased propulsive efficiency (Fig. 2.8d) for the surge direction.

2.1.4 Conclusion

This section presented an investigation into a soft actuator with non-uniform stiffness profile. The modified design and the comparison with the original actuator allowed us to investigate how a soft actuator's stiffness profile can be used to affect the direction of generated forces. The rather simple actuation and control scheme, consisting of an oscillatory motion pattern of a single degree of freedom mechanism, enables us to focus on the generated forces and study the patterns and directions.

In this case the stiffness profile of the actuator was fixed and did not allow for dynamic changes during operation. Because of this, even though the modified fin results in increased surge output, the sway component would be greatly reduced, thus almost eliminating the robot's capability to control its lateral motion. This limitation could be mitigated with a mechanism that can dynamically adjust the actuator's stiffness profile. This way, adjusting the direction of generated force output from each actuator, could be used to improve the robot's thrust vectoring, as well as to increase the robot's locomotion efficiency, without sacrificing force output in other DOFs.

Besides investigating the generated forces from an isolated actuator, as the one presented here, it would be useful to investigate how this modification affects the robot's overall motion quality and efficiency. As all experiments of this study were conducted using a static setup in still water, it is important to investigate the locomotion capabilities under non-zero inflow conditions.

2.2 Leveraging actuator morphology and material properties for underwater thrust vectoring

This section investigates how a soft actuator's stiffness profile can affect its generated forces for underwater and surface swimming. This work was motivated by the hypothesis that using a reconfigurable design that can passively adjust its shape and stiffness can optimize the drag forces that an oscillatory paddle actuator generates. To investigate this hypothesis, a novel actuator design was developed, consisting of a combination of soft and rigid parts. An experimental investigation of the generated forces and energetic characteristics of the actuator serves as proof-of-concept for this novel design. The robot μ -CAT (micro-CAT) is used as a test case for demonstration of untethered locomotion. μ -CAT is a small-scale, low-cost, underwater robot that features the same method of locomotion as U-CAT (see Section 2.1), in smaller scale and with more limited force output,

as well as sensing and computational capabilities. Due to its small size, it is preferred for testing in laboratory conditions.

2.2.1 Flapped paddle concept design and fabrication

The majority of bio-inspired underwater robots that use soft or partially soft fins, employ wake-induced forces that are generated when the actuator performs oscillatory motions [94], instead of drag-induced forces which are generated normal to the actuator's surface and are usually unwanted. As demonstrated in literature [95, 96], and as we observed in [Publication 1], while this lateral drag force component has usually a larger magnitude than lift-based forces, especially in low inflow conditions, it is also symmetric during the actuator's stroke cycle, and generates no net force.

One strategy to harness the drag-induced forces for bio-inspired propulsion includes asymmetric gait shaping [97, 98, 99, 100, 101, 102, 103] to introduce an asymmetry in the drag forces, between the power-stroke and the recovery-stroke of the actuation cycle. Other strategies that achieve asymmetric drag output, featuring less complex actuation mechanisms include passively opening and closing rigid flaps [104, 105], and a spring-loaded passive rowing joint [106]. The drag difference generated by these methods can be suboptimal, due to the inertia of rigid parts and them not opening fully during the recovery-stroke. Additionally, conventional fins have also been used to generate asymmetric drag force, using skewed motion patterns [64, 107, 108, 109]. This method can be quite effective for fish-inspired robots that use the same actuator for surge and orientation control. However, during fast swimming, turning motions require a significant level of asymmetry, which can result in lower swimming speed and intermittent motion.

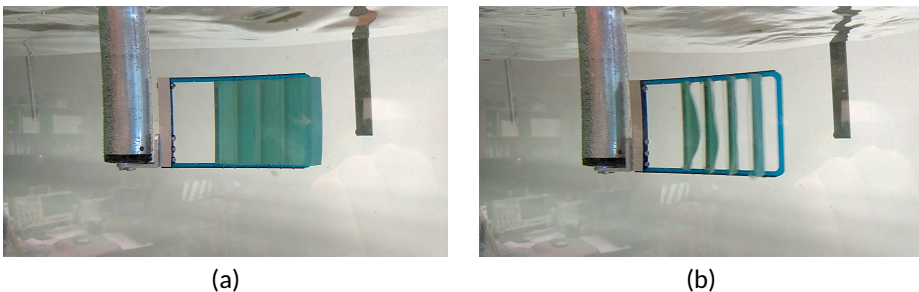


Figure 2.9: Early prototype of the flapped paddle-fin demonstrating the working principle of the soft flaps: (a) the flaps close during the power stroke, (b) the flaps open during the recovery stroke.

The actuator described in this section features a reconfigurable design that allows it to adjust the stiffness and direction of its parts, resulting in different configuration during the two phases of the actuation cycle: the power-stroke and the recovery-stroke. This is achieved with the use of a series of soft flaps, mounted on a thin rigid frame (Fig. 2.9). When at rest, the flaps are arranged in a cascaded configuration and slightly overlap in length. The actuator is mounted on a motor shaft and actuated around it in a sinusoidal motion pattern. The soft flaps are designed such that during the power-stroke, they are pressed against the rigid structure (Fig. 2.9a), forming a flat paddle that can displace water. During the recovery-stroke, the flaps are bent away from the rigid structure and allow water to pass through the actuator (Fig. 2.9b).

The soft flaps are made of silicone rubber (Zhermack Elite Double 22) cast around a thin deformable net. The net allows the thin silicone flaps to bend, without stretching, thus minimizing the drag force during the recovery-stroke, while they retain their shape

when they are pressed against the rigid frame during the power-stroke, which maximizes drag. A carbon fibre rod covered with cotton thread is also cast in the leading edge of the flaps. The rod is used to mount the flaps into the rigid frame. The cotton thread helps the silicone adhere to the carbon fibre rod. Additional support wires are placed across the frame, to prevent the flaps from passing through the gaps during the power-stroke.

2.2.2 Actuator dynamic model

The forces that act on the fin during oscillations are modelled based on the rigid paddle model by Healey et al. [110] adapted by Georgiades et al. [111, 95]. We further simplify the model by assuming a constant drag coefficient throughout the actuation cycle. This simplification makes the model significantly easier to tune for the two phases of the actuator's actuation cycle. The most significant force that acts during oscillation on a paddle at low speed locomotion, is the drag force F_D which is exerted in a direction collinear with the net flow velocity U (see Fig. 2.10). U is the sum of the fluid velocity due to the oscillatory motion NV which is normal to the paddle's surface, and the external inflow IV . Under zero inflow velocity, F_D is perpendicular to the fin's surface. The secondary lift force F_L is also exerted perpendicular to drag. At low inflow conditions however F_L is appreciably small compared to F_D , and is therefore not incorporated into the mathematical model. Moreover, modelling this force precisely is indeed a nontrivial task for the proposed actuator, and it is subsequently considered as a small residual force for control design.

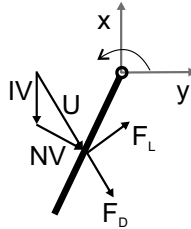


Figure 2.10: Illustration of drag and lift forces acting on the flapped paddle-fin's surface during oscillation ([Publication II] ©2020 IEEE).

The drag force F_D on the actuator is calculated by dividing the effective surface's area into several segments along its length, and the drag force due to each segment is computed according to a standard form-drag (quadratic) model [94], and subsequently integrated along the length. Let w denote the (uniform) width of each segment that is exposed to the flow during oscillation. The width of the flap area that impedes the flow during the power stroke is calculated to be 6 cm during the power stroke, and estimated to be 0.6 cm during the recovery-stroke. This approximation is made because most of the flap area does not impede the flow during recovery, however there is a residual drag from the frame and parts of the soft flaps near the hinges. Then, the drag force is given by

$$F_D(t) = \int_{0.03}^{0.1} \frac{1}{2} C_d \rho w \dot{\theta}^2(t) s^2 ds, \quad (4)$$

where C_d is the drag coefficient, $\rho = 997 \text{ kg m}^{-3}$ is the fluid density, θ is the instantaneous angular displacement of the motor shaft, and ds is the incremental length. The effective

area that generates drag, based on the actuator geometry, is set to be within 3 cm to 10 cm of its length (see Fig. 2.11b).

With the actuator's existing configuration, it is assumed that the power-stroke occurs when θ decreases and recovery-stroke occurs when θ increases. The lateral force during the power-stroke is given by

$$\begin{aligned} F_D(t) &= \frac{1}{2} C_d \rho w \dot{\theta}^2(t) \left[\frac{s^3}{3} \right]_{0.03}^{0.1} \\ &= 9.1 \times 10^{-5} C_d \rho \dot{\theta}^2(t). \end{aligned} \quad (5)$$

Due to the reduced area of the actuator generating drag during the recovery-stroke, we obtain the lateral force by using $w = 0.6$ cm as

$$F_D(t) = -9.1 \times 10^{-6} C_d \rho \dot{\theta}^2(t). \quad (6)$$

The components of the generated force, under zero inflow conditions, in the body-fixed frame of the force-plate are given by

$$F_x(t) = F_D(t) \sin(\theta(t)), \quad (7)$$

$$F_y(t) = F_D(t) \cos(\theta(t)). \quad (8)$$

The angular displacement is achieved using a proportional control law for the motor, with reference

$$\theta_r = -\frac{A}{2} \sin(2\pi f t). \quad (9)$$

2.2.3 Experimental characterization of actuator forces

The actuator's performance was evaluated experimentally, through a parametric study of the kinematic variables A and f of its oscillatory motion (9), as well as through a comparison with an existing soft fin of similar size. For this purpose, a series of experiments was conducted with the proposed actuator mounted on a force/torque measuring device, submerged in a laboratory test tank (Fig. 2.11c). A second set of experiments was conducted using the existing μ -CAT actuator (Fig. 2.11a). Additionally, the experimental data was used to validate the mathematical model presented in Section. 2.2.2.

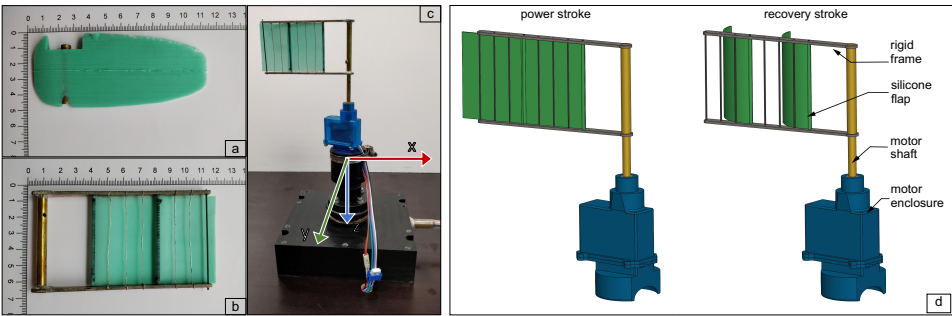


Figure 2.11: The flapped paddle-fin prototype ([Publication II] ©2020 IEEE): a) soft fin used for comparison, b) proposed flapped paddle-fin, c) Fin prototype mounted on force/torque test bed, d) CAD illustration of the two states of the fin prototype, during power and recovery stroke.

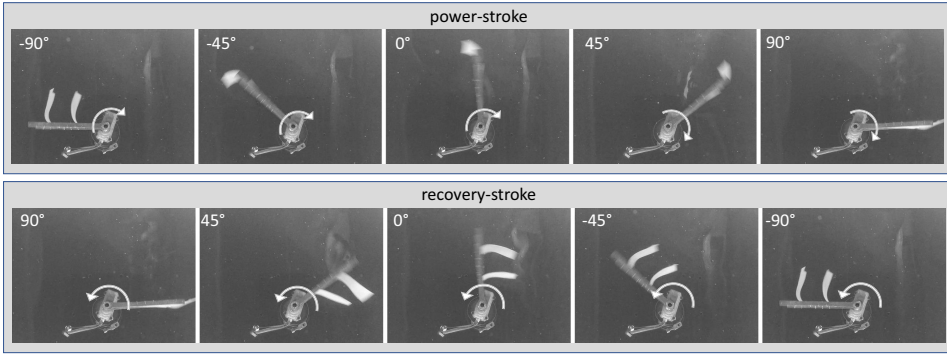


Figure 2.12: Still frames of the flapped paddle fin in oscillation showing the motion of flaps, closing and opening during the power and recovery stroke respectively ([Publication II] ©2020 IEEE)

The collected data was filtered to reduce noise, and averaged values of the forces and current consumption were calculated over a number of whole periods of steady state oscillation. Similar to the experiments in Section 2.1.3, the ratio of surge force over consumed power η was used as a metric of propulsive efficiency [93] as described in (3). In this case the force component F_p is the propulsive force, that is F_x for the original soft fin and F_y for the proposed actuator.

Fig. 2.12 demonstrates the principle of operation of the soft flaps on the proposed actuator, through a series of still photos during one cycle of actuation. The photographs were taken from below with the camera directed upwards towards the actuator, which was suspended upside-down and fully submerged in water. The photos show clearly the closing and opening of the soft flaps during the recovery-stroke and power-stroke phases of the actuation cycle. The angular position of the actuator in the frames has been inverted compared to what is seen in Fig. 2.14b.

Fig. 2.13a and Fig. 2.13b show indicative results during two different runs, using the original soft actuator and the proposed actuator respectively. The oscillation kinematic parameter set for each of these indicative runs was selected to demonstrate the max-

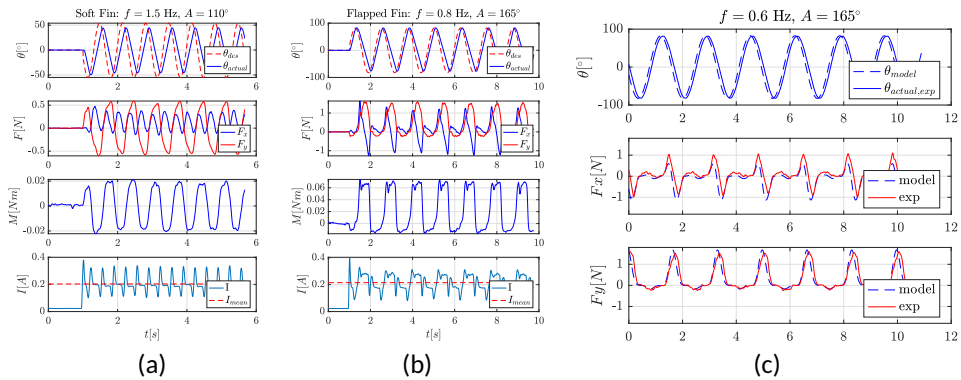


Figure 2.13: Indicative experimental results of flapped paddle-fin and original soft fin, including position feedback (top), generated forces and torque (middle) as well as instantaneous and mean current consumption (bottom): (a) soft fin, (b) flapped fin, (c) comparison of simulated model and experimentally measured forces ([Publication II] ©2020 IEEE)

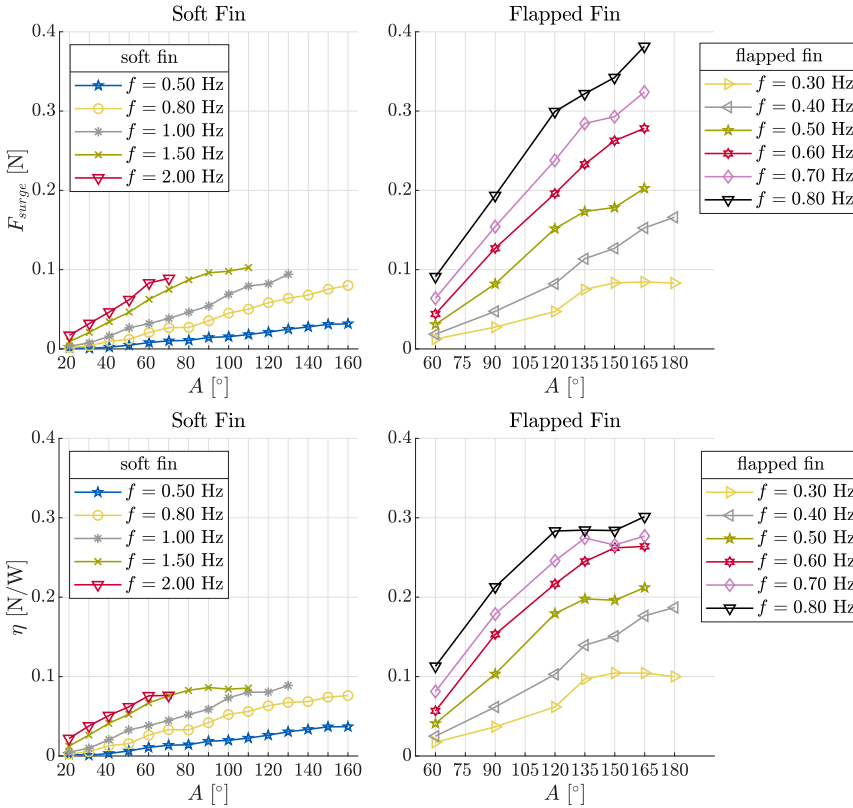


Figure 2.14: Parametric study of forces for a range of amplitudes and frequencies of oscillation with flapped paddle-fin (right) and soft fin (left) showing the average propulsive force component (top), and propulsive efficiency (bottom) ([Publication II] ©2020 IEEE).

imum propulsive performance in each case. The top graph shows the temporal evolution of the motor’s angular position, compared to the desired motion profile. The second graph shows the generated force vectors, with propulsive components being F_x for the soft fin and F_y for the proposed actuator. The third graph shows the torque around the vertical axis. The bottom graph shows the instantaneous current consumption with blue colour, and the averaged with red dashed line. The main difference here can be seen in the pattern and magnitude of the generated propulsive force. The original fin generates a propulsive force vector that has double the frequency of the actuation cycle. The proposed fin demonstrates a propulsive force much larger in magnitude, which follows the same frequency f as the actuation cycle. The minor negative force segments can be attributed to the small area of the soft flaps that generate drag during the recovery-stroke.

Fig. 2.13c shows the results of the experimentally acquired as well as the simulated forces based on the model presented in Section 2.2.2. The model follows the experimental data very closely, not taking into account unmodelled wake-induced forces and minor disturbances that occur during oscillation. It should be noted here that the drag coefficient C_d was calculated empirically using experimental data and has been averaged over the surface area of the fin. This can also account for some of the inaccuracy of the model.

Fig. 2.14 shows aggregated results of a parametric investigation into the effect of the kinematic parameters A and f to the generated propulsive forces for both studied actu-

ators. The top graphs show the averaged propulsive force, demonstrating a rather significant increase, with the maximum average values being over three times larger for the proposed actuator than for the original fin. The bottom graphs show the averaged propulsive efficiency, with the proposed actuator showing similar improvement. This behaviour can be attributed to the fact that while the consumed power for both actuators is comparable, the proposed actuator's generated propulsive force is significantly larger.

2.2.4 Trials with the μ -CAT robot

To investigate the quality of motion the proposed actuator can achieve, the small-scale underwater robot μ -CAT was used (Fig. 2.15). Four nearly identical actuators were fabricated and mounted on the robot's servo-motors. A series of actuation schemes were pre-programmed into the robot's control unit, driving the actuators to achieve a set of locomotion primitives (Fig. 2.16) for both underwater and surface swimming. The phase offset ϕ and angular offset A_0 of the motors' oscillation pattern were selected in order to direct the averaged generated forces accordingly with each locomotion primitive.

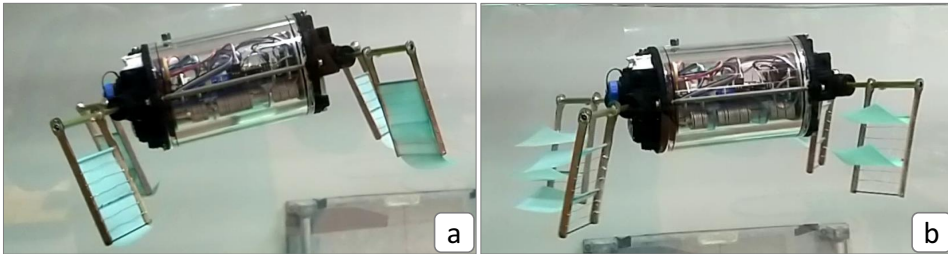


Figure 2.15: The μ -CAT robot swimming underwater using flapped paddle-fins (adapted from [Publication II]): a) flaps close during power-stroke, b) flaps open during recovery-stroke

During these tests, the robot demonstrated agility and manoeuvrability, justifying the design choice of the actuator. A detailed description of the trials and the resulting motions can be found in [Publication II] and its accompanying video.

2.2.5 Discussion and Conclusion

This section presented an investigation into a partially soft actuator with a reconfigurable design that allows adjusting its shape and stiffness passively. The experimental investiga-

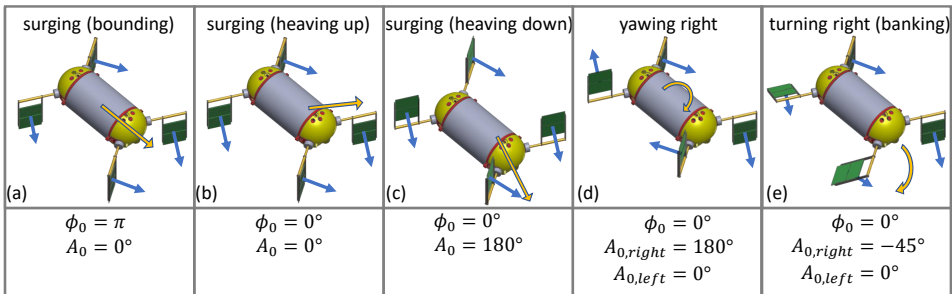


Figure 2.16: Kinematic inputs for swimming gait trials with μ -CAT using flapped paddle-fin actuators. The angular offset (A_0) and phase offset ϕ_0 were pre-selected to achieve the selected locomotion primitives ([Publication II] ©2020 IEEE). The robot's motion direction is indicated with yellow arrows. The individual actuator force directions are indicated with blue arrows.

tion of the generated forces serves as proof-of-concept of the actuator's reconfigurable design and provides some insight into how drag forces can be utilized for thrust vectoring. The trials using a small robot provide insight into the effects of using this actuator and help increase our understanding of its advantages as well as limitations.

Specifically, as seen in Fig. 2.13b, while the proposed actuator generates larger force peaks, this increase does not come without drawbacks, as the motion pattern follows a slower stroke generating intermittent motion. This was also observed during the trials with μ -CAT. There can be applications where this characteristic is unwanted, and a smoother operation is required. Strategies to mitigate this side effect could include implementing a non-synchronised stroke pattern between the robot's four actuators, by applying a phase offset to their oscillatory motion.

Additionally, the propulsive force vector can only be generated in one direction of motion of the actuator, meaning the directions of power-stroke and recovery stroke are fixed. Because of this, when used by a robot like μ -CAT, the actuator's reference of oscillation would need to be shifted by 180° in order to generate an opposite force. This might not be possible, if the robot is operating on or near the surface of the water.

A drawback of the design that was observed was that in some cases the flaps did not return to the overlapping 'power-stroke' position right away, possibly due to vortices generated by the fin's motion. Modification to the actuator's morphology, changing the design or material, can be made to ensure more consistent behaviour of the soft flaps.

Lastly, the actuator's performance was quantitatively evaluated only in zero inflow conditions. It would be particularly interesting to investigate the effects of inflow to the behaviour of the soft flaps, as well as to the motion of an untethered robot.

2.3 Conclusions

In this chapter two methods of locomotion were discussed, that rely on variable stiffness to generate the forces required for thrust vectoring in underwater or surface swimming scenarios. In the first case, an actuator with a permanent non-uniform stiffness profile was used to investigate its effects to the generated force. By comparison with a similarly shaped existing actuator with a uniform stiffness profile, we demonstrated the effects of this modification. The drawback of using a permanent stiffness profile is that while it may improve performance in some areas, it may decrease it in others. The main outcomes of this work are that, the stiffness profile of an actuator can be used to improve performance, however a stiffness profile that can be adjusted online would be preferable.

In the second case, a passively reconfigurable actuator was used to demonstrate how online passive adjustment of the actuator's shape and stiffness can be used to optimize its force output and energetic characteristics. The reconfigurable design allowed to use the usually dominant but unusable drag forces, without increased mechanical, motion planning, or control complexity. An experimental comparison with an existing soft foil actuator of similar size showed significant improvement in actuator performance. While this actuator has some limitations regarding the repertoire of locomotion patterns it can generate, it is providing some understanding into how this type of reconfigurable mechanism can optimize locomotion.

Specifically, the contributions of the work described in this chapter include:

- The design and fabrication of two actuator prototypes that feature two methods of variable stiffness, static and passively adjustable.
- The experimental parametric analysis of the actuators' output.
- A simplified force model for the second actuator, and its experimental validation.

3 Variable stiffness actuation for amphibious locomotion

This chapter investigates amphibious locomotion using a variable stiffness actuator. Parts of the work presented in this chapter have been published in [Publication III]. As discussed in Chapter 1, effective locomotion in unstructured environments with variable levels of water content, benefits from actuation systems with built-in reconfigurability and compliance. Specifically, while the compliant behaviour soft actuators exhibit is considered necessary when interacting with the surroundings, selectively increasing the stiffness and changing shape is also needed in order to adapt and generate forces required for locomotion in a variety of environments. For this reason, and building on the conclusions from the work described in Sections 2.1 and 2.2, the criteria for this investigation of amphibious locomotion were the actuator's reconfigurability of shape and variability of stiffness.

In this context, a novel actuator, that was described in [Publication III] is presented as proof-of-concept of locomotion in terrestrial and aquatic conditions. The proposed actuator (see illustration in Fig. 3.1) features a reconfigurable design that enables a dynamic switch between two forms, each of them appropriate for locomotion in different environmental conditions. The actuator's locomotion efficacy is experimentally evaluated separately in each locomotion setting, in terrestrial and aquatic conditions, as well as in the interface between aquatic and terrestrial conditions. The results demonstrate that while relying on two different but rather simple motion planning and control strategies, the actuator's morphology and compliant material enable locomotion in aquatic, terrestrial, and in multi-phase environments.

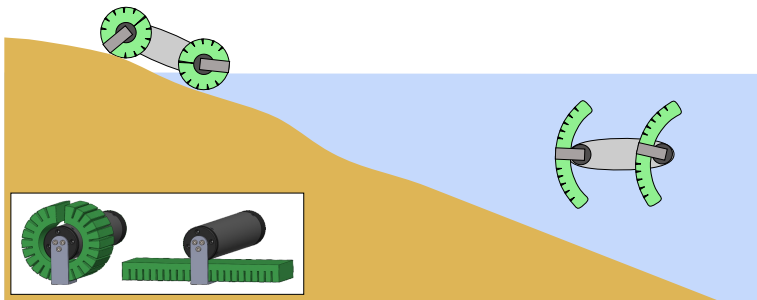


Figure 3.1: Illustration of concept vehicle using the variable stiffness actuator in a variety of environmental conditions [Publication III]. Top Left: the fully pressurized, stiffer actuator generates tractive forces enabling terrestrial locomotion by rotating around a motor shaft. Right: the softer actuator generates propulsive forces enabling underwater swimming by oscillating around the motor shaft. The inset depicts a CAD model of both states of the actuator mounted on a motor shaft.

The design of this actuator was inspired by the fast PneuNet design described in [112]. PneuNet actuators consist of a soft elastomeric part, usually silicone rubber, that contains a network of interconnected air chambers. Some implementations also include an embedded flexible strain-limiting element, that is used to determine the actuator's bending profile [113, 114, 115]. The shape and stiffness of these actuators can be controlled by adjusting their internal pressure, by increasing the volume of the fluid that is contained in their internal network of chambers. Their relatively simple design and actuation, along with demonstrated reliability and robustness [116, 112] have made them attractive for a variety of applications. This type of actuator has been used to study grasping [117, 118], rehabilitation [119], as well as locomotion [120, 121, 116]. Other soft pneumatic actuator designs similar to the PneuNet have also been developed and used for locomotion, using fabrication techniques such as silicone rubber casting [122] and 3D printing with flexible

materials [123].

The hypothesis that motivated this work was that because this design allows the dynamic adjustment of the actuator's stiffness and shape, it can be suitable for locomotion in a variety of different conditions, premise partly supported by [52]. More specifically, by increasing the internal pressure of the actuator, it deforms as seen in Fig. 3.1 and Fig. 3.9a. In this state it can function as a wheel, rotating around the motor shaft. When the internal pressure is kept at low levels, it can function as a paddle and can be used to generate propulsive forces by performing oscillations around the motor shaft.

3.1 Actuator material modelling

During the initial design stages of the actuator, a simulation was used to determine its final morphology and dimensions, as well as to predict its bending behaviour. The actuator discussed in this chapter consists of a few rigid parts, but mostly of soft parts, made of silicone rubber, a flexible elastomer in the wider category of hyperelastic or green-elastic materials. This material was selected as it can withstand large strains with no permanent deformation. The following subsections describe the process of obtaining the material parameters for the model that was used in this simulation. To summarize the process, initially the model type was selected (see Section 3.1.2), then a set of silicone specimens were fabricated and used in uniaxial tensile tests (Section 3.1.1). The data was post processed and used to identify the material model parameters. Lastly, the model was validated (Section 3.1.3), to ensure its accuracy before using in simulations.

3.1.1 Uniaxial tensile tests and data processing

Five nearly identical specimens of Elite Double 22 silicone were prepared following the ASTM D412 standard for Vulcanized Rubber and Thermoplastic Elastomers [124], using the Die D dimensions (Fig. 3.2) of dumbbell shape. While the most common method of fabricating the specimens according to this standard is die cutting them from a sheet of material, in this case, for convenience, a 3D printed mould was used to cast them (Fig. 3.2) similar to the process presented in [125]. For consistent results the same process of fabrication was followed for all specimens. Initially, a release agent was applied to the mould, then a batch of silicone was mixed, degassed, poured into the mould, and degassed again. As a last step before curing, a flat heavy object was placed on top of the mould, to ensure the flatness of the specimen's top surface. Using an Instron 5866 uniaxial testing machine (Fig. 3.3d,e) and following the ASTM D412 standard, tensile tests until break were conducted with the five specimens, and raw data of the extension (mm) and load (N) was collected.

The process of modelling the deformation response that was used in this work requires

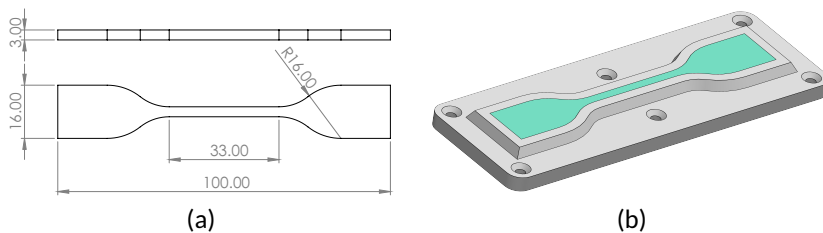


Figure 3.2: Mould for casting dumbbell specimen for tensile test: (a) The specimen dimensions. (b) CAD model of the mould and specimen.

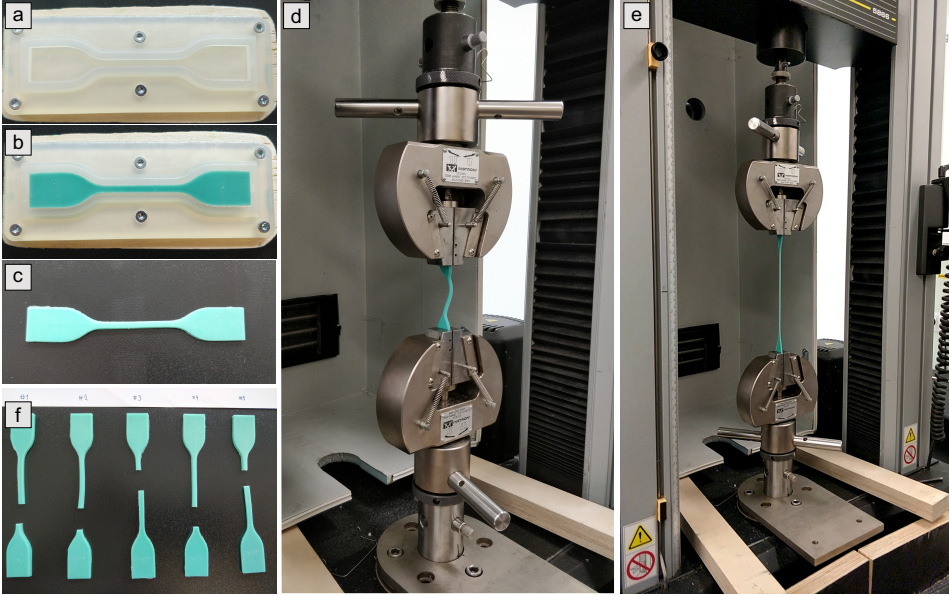


Figure 3.3: Fabrication and uniaxial tensile testing of silicone specimens (Elite Double 22 by Zhermack): (a) 3D-printed mould, (b) casting the specimen, (c) cured specimen, (d,e) specimen during tensile test, (f) all specimens after break

true stress-strain data [125], which can be calculated from the load-extension data that was acquired during the tensile tests. For all specimens, the data is processed as follows.

First, the engineering stress and strain are calculated from the load-extension data. The engineering stress σ_e is calculated as the axial load F over the surface of the specimen's initial cross-section A_0 :

$$\sigma_e = \frac{F}{A_0}. \quad (10)$$

The engineering strain ϵ_e is calculated as the change in length ΔL per unit of the original length L_0 of the specimen's middle part.

$$\epsilon_e = \frac{\Delta L}{L_0}. \quad (11)$$

With the stretch ratio defined as:

$$\lambda = \frac{L}{L_0} \Rightarrow \lambda = 1 + \epsilon_e, \quad (12)$$

the true stress and strain can be calculated. The true stress σ_t is the axial load over the surface A of the instantaneous cross-section. This calculation takes into account the variability of the cross-section due to tension in the direction normal to it and the conservation of volume ($AL = A_0L_0$).

$$\sigma_t = \frac{F}{A} \Rightarrow \sigma_t = \sigma_e(1 + \epsilon_e). \quad (13)$$

The true strain ϵ_t (or logarithmic strain) expresses the change in length δL per unit of the instantaneous length, and is calculated by:

$$d\epsilon_t = \frac{dL}{L} \Rightarrow \epsilon_t = \ln(1 + \epsilon_e) \quad (14)$$

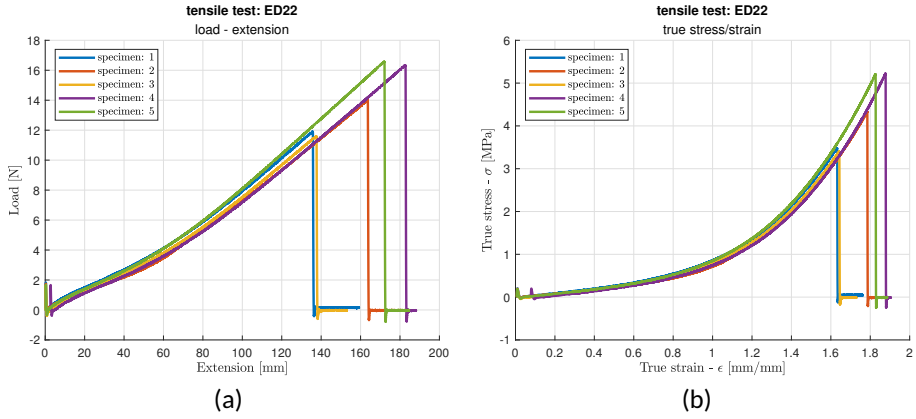


Figure 3.4: Uniaxial tensile test data of silicone specimens (Elite Double 22 by Zhermack): (a) raw load-extension data, (b) true stress-strain data

The raw load-extension and resulting stress-strain curves for five specimens of Elite Double 22 silicone can be seen in Fig. 3.4. The stress-strain data is used for modelling the material parameters as described in Section 3.1.2.

3.1.2 Yeoh hyperelastic model

As mentioned above, the main purpose of this model is to finalize the prototype's morphology by predicting its deformation under load. While development of soft robots relies heavily on experimental results and prototyping [126], modelling the deformation behaviour, even for static analyses, can help reduce the development time and cost.

Linearly elastic material models that can describe relatively small strains commonly rely on two material parameters, Young's modulus or Poisson ratio. However, pneumatic and fluidic actuators such as the one described in this work require significant deformations. To address this requirement, the materials used to fabricate these actuators demonstrate highly nonlinear stress-strain relationships, with large reversible deformations of up to 500% strain [127]. Due to these characteristics, these elastomeric materials are categorized as hyperelastic or green elastic materials. As linear elastic models can not accurately describe the material behaviour of hyperelastic materials, development and use of hyperelastic material models has been increasing in the last decades [127, 128].

The deformation behaviour of hyperelastic materials' nonlinear stress-strain relationship, is described by a strain energy density function W , which is a function of the elastic strain state.

$$W = f(I_1, I_2, I_3), \quad (15)$$

where W is the strain energy density, and I_1, I_2, I_3 are the three invariants of the Green deformation tensor, given in terms of the principal extension ratios $\lambda_1, \lambda_2, \lambda_3$, as

$$I_1 = \lambda_1^2 + \lambda_2^2 + \lambda_3^2 \quad (16)$$

$$I_2 = \lambda_1^2 \lambda_2^2 + \lambda_2^2 \lambda_3^2 + \lambda_3^2 \lambda_1^2 \quad (17)$$

$$I_3 = \lambda_1^2 \lambda_2^2 \lambda_3^2 \quad (18)$$

The principal extension ratios (or principal stretches) express the extent and direction to which a unit volume of the material has changed its dimensions during deformation, defined as

$$\lambda_i = \frac{l_i}{L_i}, i \in 1,2,3 \quad (19)$$

The strain energy density function W defines the amount of elastic energy stored in a unit volume of material, at a given state of strain [128].

Deriving analytical models for soft robots is rather challenging [126, 128], due to material related nonlinearities, as well as due to the complex geometries that soft fluidic actuators commonly use. For this reason an FEM model was preferred in this work. The main criterion of model selection was the expected strain range and the available type of data for the parameter identification [127]. Additionally, in order to utilize the strain energy function, the material is assumed incompressible, isotropic, homogeneous, free of hysteresis, and strain-rate independent [127, 128, 125].

The true stress-strain data from specimen 3 (see Section 3.1.1) was used to model the material in Ansys Workbench, using a 3rd order Yeoh hyperelastic material model. This model was selected as it describes the deformation of nearly or fully incompressible nonlinear elastic, rubber-like materials quite accurately, relying on only the first strain invariant I_1 and allows fitting various modes of deformation using only uniaxial tensile test data [129].

Assuming incompressibility of the material, the strain energy function is given by:

$$W(I_1) = \sum_{i=1}^3 C_{i0}(I_1 - 3)^i \quad (20)$$

where $C_{10} = 78783 \text{ Pa}$, $C_{20} = 16732 \text{ Pa}$, $C_{30} = 6618.5 \text{ Pa}$ are the material constants obtained from fitting the tensile test data to the 3rd order Yeoh model. The incompressibility parameters are $D_i = 0$, $i \in 1, 2, 3$. The strain-limiting inextensible elastic layer was modelled using a 1st order Yeoh model with material constant $C_{10} = 7.9 \text{ MPa}$ [130].

3.1.3 Material model experimental validation

The model parameters were validated experimentally, via a comparison between the deformation of a simulated soft fluidic actuator and a physical prototype of the same design,

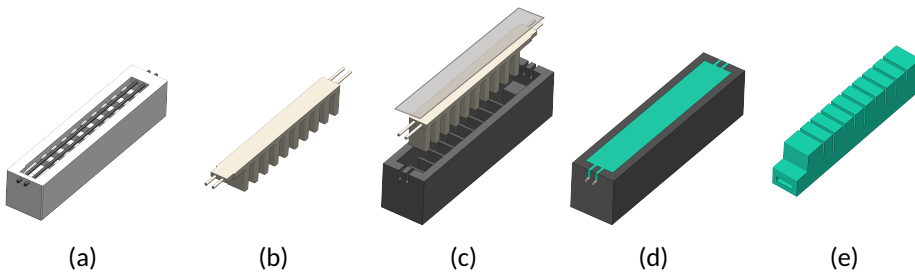


Figure 3.5: The fabrication process of a simplified variable stiffness actuator illustrated using CAD models: (a, b) Fabrication of wax core by casting in 3D printed mould, (c) Assembly of wax core and strain limiting fabric in actuator mould, (d) Casting silicone into mould, (e) The cured silicone actuator.

under the same load. For this purpose, a scaled-down, partial version of the proposed actuator was fabricated, following the two-step lost-wax process described in Section 3.2, and illustrated in Fig. 3.5.

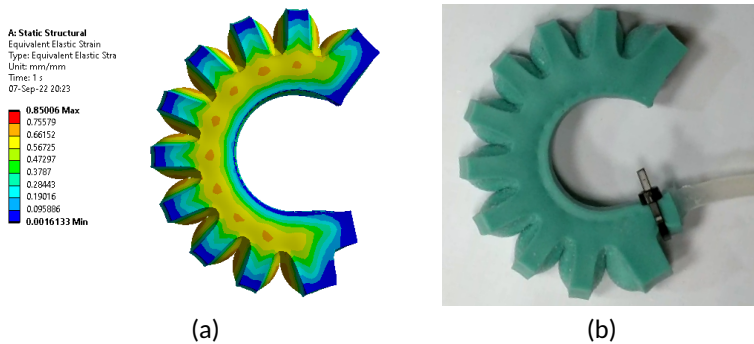


Figure 3.6: Experimental model validation using simulated and physical actuator. The prototype is deformed under 100 kPa of added pressure: (b) Strain study on Ansys, (a) Physical actuator

For the validation, a 3D CAD model of the physical prototype was imported to ANSYS workbench, and a static analysis was performed to investigate the deformation profile of the prototype, under a set of added internal pressure values. The physical prototype was connected to a pressure measurement device and was subjected to the same set of internal pressure increases. Due to its incompressibility, water was used to increase the internal pressure, to ensure consistent pressure is applied to the internal walls of the prototype and to the pressure sensor [112]. The prototype's deformation was captured on video. An example setpoint of this process can be seen in Fig. 3.6, with the simulated and physical prototypes deformed under 100 kPa of added pressure. This comparison visually demonstrates the hyperelastic model's accuracy.

3.2 Actuator design and fabrication

The model described in Section 3.1.2 was used in an iterative process of design and simulations to obtain the final actuator morphology. In alternating steps, The actuator's CAD model was modified in SolidWorks, and its deformation under load was simulated in an Ansys Workbench FEM static simulation.

The following boundary conditions and simulation settings were applied:

- The external surfaces between the chambers were defined as 'frictionless contact pairs', to prevent the actuator geometry from penetrating itself.
- A 'bonded contact' was defined between the inextensible (strain-limiting) layer and the actuator.
- The flat face surrounding the fixation bolts was defined as a 'fixed support'.
- All internal surfaces (belonging to chambers and interconnecting channels) were used to apply the internal pressure. Pressure was applied normal to the internal surfaces.

This process was only aimed at finding the geometry that would allow the desired deformation, and does not optimize the actuator morphology for dynamic phenomena, such as thrust and tractive forces. In this context, the design parameters that were adjusted

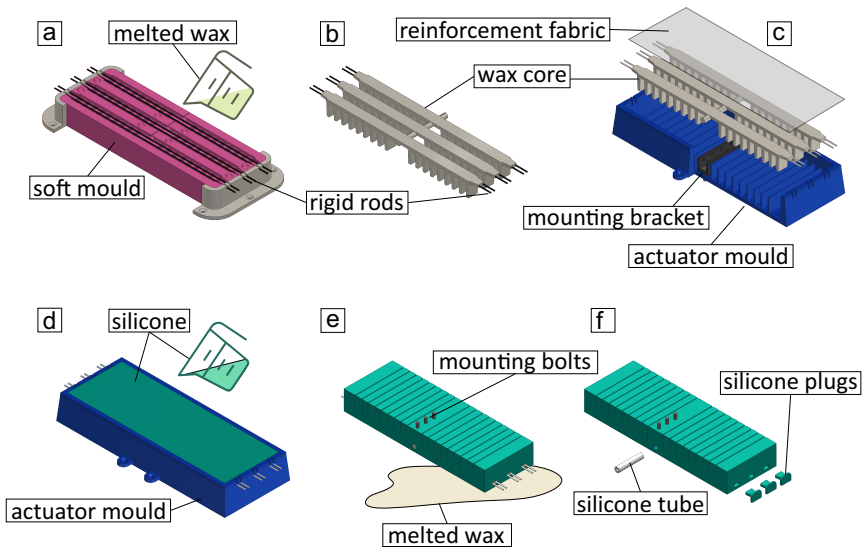


Figure 3.7: The fabrication process of a variable stiffness actuator (adapted from [Publication III]): (a-b) Fabrication of wax core, casting melted wax in a soft mould with 3d printed brackets and support rods. (c-f) Fabrication of soft actuator, casting silicone in a 3d printed mould, around the wax core. The prototype is finished by melting off the wax core and sealing the openings with cast silicone plugs.

and finalized using this process were the number and geometry of chambers, the inner wall thickness, the outer wall thickness, and the size of the gaps between the chambers.

Using the finalized morphology parameters obtained from the FEM analysis, a physical prototype was fabricated. A two-step, lost-wax process was followed as seen in Fig. 3.7. The fabrication process illustrated in Fig. 3.7 is as follows:

- a Six thin metal rods ($\varnothing .5\text{ mm}$) are suspended over a soft silicone mould on two 3D-printed brackets. These rods provide stability to the wax core, and serve as attachment points during casting the actuator. Melted wax is poured into the mould and allowed to set.
- b The wax core is demoulded and cleaned of excess wax.
- c An aluminium bracket with a series of bolts fastened on it, the wax core and a reinforcement fabric are assembled into the mould. The bolts are used to fasten the cured actuator to a motor shaft. The reinforcement fabric will act as the strain-limiting layer.
- d A batch of silicone is mixed, degassed and poured into the mould. While in the mould, the silicone is degassed a second time and allowed to cure.
- e The cured silicone actuator is demoulded, the wax is melted off at 80°C and pours out from openings on its sides.
- f After the wax and metal rods have been removed and traces of wax have been cleaned, silicone plugs and an intake silicone tube are glued in using Sil-Poxy by Smooth-On.



Figure 3.8: The variable stiffness actuator final prototype [Publication III]. The actuator is deformed by increasing its internal pressure by 100 kPa. Left: Equivalent elastic strain levels in FEM simulation. Right: The physical prototype with a fluid intake silicone tube and a pressure measurement module.

This method of fabrication is slightly more challenging compared to the traditionally popular method of casting the top and bottom parts of the actuator separately and then bonding them together [131, 132, 133]. This method was initially attempted but resulted in frequent failures of the bond between the two parts. As the actuator described in this thesis has a rather large surfaces that needs to be bonded, the method described in Fig. 3.7 produces more consistent results, with fewer failure points. A simulation and the final physical prototype can be seen in Fig. 3.8 deformed under the same internal pressure.

3.3 Experimental evaluation of locomotion performance

The actuator's locomotion performance in underwater and terrestrial conditions, was evaluated via a series of experiments, performed separately for each of the two scenarios. This section describes this process and its outcomes. For both scenarios, the soft actuator was mounted on a waterproofed BLDC motor (EC-max 30 by Maxon Motors) driven by an EPOS2 36/2 motor controller, such that it was allowed to fully deform and rotate around the motor shaft (Fig. 3.9).

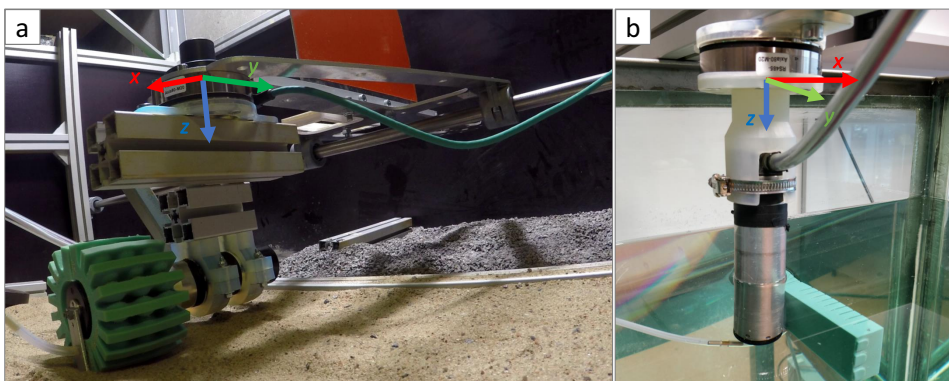


Figure 3.9: Experimental testbeds for locomotion performance evaluation of the variable stiffness actuator [Publication III]: (a) terrestrial, (b) underwater.

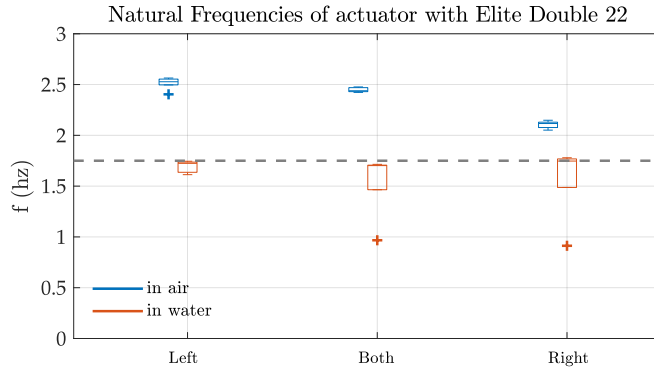


Figure 3.10: Experimentally determined first natural frequencies of variable stiffness actuator in air and in water. The grey dashed line denotes the highest actuation frequency for underwater oscillations.

3.3.1 Natural frequency analysis

The actuator's first natural frequency was investigated, as the actuation frequency relative to the natural frequency can affect its force output and energetic efficiency for underwater swimming. The first natural frequency was experimentally estimated using force measurements after manual excitation.

Specifically, a series of tests was performed, where the actuator was manually deformed and allowed to return to rest, while measuring the generated forces, in a setup identical to the one seen in Fig. 3.9b. A total of 30 tests were performed, consisting of 2 testing environments (actuator suspended in air and in water), 3 types of excitation (deforming the left, right, and both sides), and 5 replicates for each. A discrete Fourier transform algorithm was used on this data to identify the frequency components. The first natural frequency was found to be on average $f_{n,air} = 2.439$ Hz and $f_{n,water} = 1.7241$ Hz while suspended in air and in water respectively (Fig. 3.10).

3.3.2 Motion patterns and control

To achieve locomotion in the two target environments, two motion profiles were implemented. An oscillatory motion pattern of the undeformed actuator was used to generate forces in an underwater setting. A continuous rotation with the fully deformed actuator was used to generate tractive forces on sandy terrain. The motor driver hardware used for these experiments offers a variety of operating modes, using position, velocity and current control, with predetermined controller structures for each: PID position control, PI velocity control, PI current control [92]. Additionally, both operating modes for position control and velocity control employ acceleration and velocity feedforward components, and a current controller as a subordinate regulator.

The controller structure selection was based on the desired actuator motion pattern; profile position mode (Fig. 2.5) for oscillatory motion and profile velocity mode (Fig. 3.11) for continuous rotational motion. To achieve a paddle-like behaviour and to generate propulsive forces underwater, the internal pressure of the actuator was kept at low levels, and the motor shaft was driven with an oscillatory motion pattern. The motion pattern and control for this motion are described in Section 2.1.2. To achieve a wheel-like behaviour and generate tractive forces, the internal pressure of the actuator was initially increased until it reached the desired deformed state, after which, the motor was driven at

a constant angular velocity. The control scheme used for this mode (Fig. 3.11), was implemented as a velocity controller with "Profile Velocity Mode" in Maxon's EPOS2 Module 36/2 [91]. This structure employs a velocity PI controller with a current PI controller as subordinate regulator, and is described in more detail in Publication III and in [91, 92].

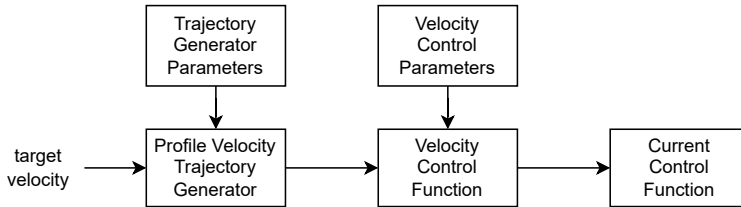


Figure 3.11: Velocity control structure for continuous rotations [92, 91].

In both experimental scenarios, feedback controller gains and feedforward factors were tuned in a Hardware-In-the-Loop configuration using the "Regulation Tuning Wizard" in EPOS Studio software (see Section 7.4 in [92]). For tuning, the Epos Studio software connects to the motor driver and actuates the motor through a series of motions using a variety of inputs, covering a spectrum of accelerations and velocities. The software performs an automated parameterization process that includes identification and modelling of the plant, parameter identification of the controller parameters (feedback and feedforward), and verification of the controller (feedback and feedforward). After successful tuning, the controller parameters are written into the motor controller. To ensure the maximum performance of the resulting controllers, similar conditions were applied for the tuning process as with the actual experiments, such as friction, inertia and gravity, by setting up the actuator, cables, and other equipment in the same configuration.

3.3.3 Characterization of propulsive forces

The actuator's underwater locomotion performance was evaluated via a series of experiments in a water tank (Fig. 3.9b), focusing on the measurement of generated forces during oscillatory motion. A parametric analysis was performed to investigate the effects of the oscillations' kinematic parameters (amplitude A and frequency f) to the generated forces and current consumption. Post-processing included filtering noisy data and summarizing the performance metrics by calculating averaged values of forces and current consumption, over a number of whole periods of steady state oscillation.

To evaluate the controller performance, the amplitude tracking error was calculated by comparing the average actual oscillation amplitude with the nominal desired oscillation amplitude.

$$A_{error} = |A - (\bar{\theta}_{high} - \bar{\theta}_{low})| \quad (21)$$

To evaluate the actuator's energetic characteristics, the ratio of propulsive force over the averaged consumed power was used [93], as described in (3) in Section 2.1.3.

Fig. 3.12 shows the results of the experimental evaluation of the actuator's underwater propulsive force generation. Fig. 3.12a shows indicative results from an underwater experiment. It can be observed in this graph that the pressure measurement follows the pattern of generated propulsive forces, which can provide a proprioceptive approach for estimating the generated forces. Examining the pressure measurement in combination with the motor shaft's angular position, gives an indication of the deformation due to the drag forces that the actuator's outer surface is exposed to while oscillating. In the current consumption graph, the measurement is quite noisy in the first second, while the rest of

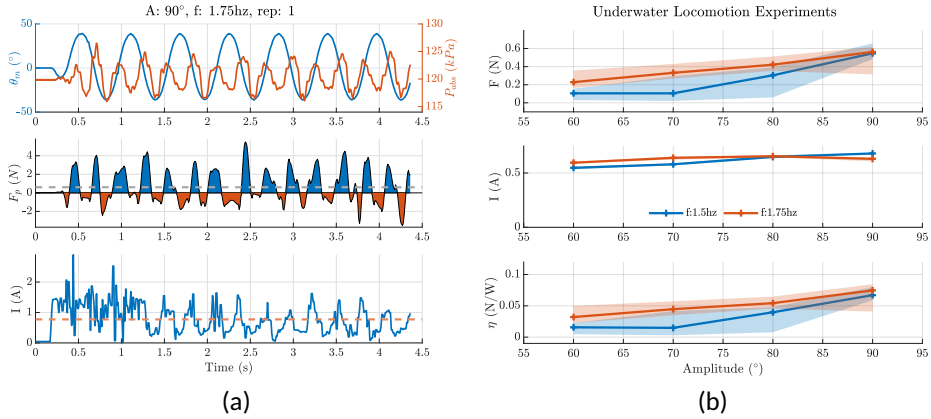


Figure 3.12: Experimental results of underwater force characterization with the variable stiffness actuator [Publication III]: (a) Indicative results. The upper graph shows the motor's actual position as it follows a sinusoidal motion pattern, and the measured internal pressure of the actuator. The middle graph shows the temporal evolution of the instantaneous propulsive force. The dashed horizontal line denotes the phase-averaged value, with positive (forward) forces shaded blue and negative (backward) forces shaded red. The lower graph shows the instantaneous current consumption of the motor in blue colour and the average current consumption as a dashed horizontal line. (b) Parametric study of the full range of amplitudes and frequencies of oscillation. The crosses show the median values of 10 replicates for each parameter set, with 25th and 75th percentiles as shaded areas. The upper graph shows the evolution of thrust forces, as the amplitude of oscillation increases, for two frequencies of oscillation. The middle graph shows the median current consumption. The lower graph shows the energetic efficiency metric as described in (3).

the graph follows the generated force peaks. This is a transient effect at the beginning of each underwater locomotion experiment that was observed in previous implementations with this motor driver hardware [1], and is most probably attributable to the type of controller used. This noisy transient period was excluded from the calculation of the average values for all measurands.

Fig. 3.12b shows aggregated results of the underwater experiments, summarizing the entire sweep of experimental parameters. Two frequencies and four amplitudes of oscillation were studied. While increasing the amplitude and frequency of oscillation generally results in increased propulsive forces, they seem to converge in the higher end of amplitude. This is attributed to increased amplitude tracking errors that were observed in this experiment set, due to velocity and acceleration limitations imposed to the controller. Additionally, while current consumption is higher for the faster experiments ($f = 1.75\text{Hz}$), it is lower at $A = 80^\circ$ and $A = 90^\circ$. We hypothesize that this can be attributed to the proximity of this set to the actuator's first natural frequency described in Section 3.3.1. Regarding the actuator's propulsive efficiency η , while it performs worse here than the other prototypes described in this thesis that have been designed purely for underwater locomotion [Publication I] and [Publication II] this is an acceptable trade-off, as it enables locomotion in a wider range of environments.

3.3.4 Characterization of tractive behaviour

The actuator's performance for locomotion on dry and wet terrestrial conditions was evaluated via a set of experiments on sandy terrain (Fig. 3.9a), focusing on the measurement of the distance travelled by the actuator as it rolls on the ground. A parametric analysis

was performed to study the effects of motor angular speed and water content in the soil to the actuator's travelling speed and energetic efficiency.

In post-processing, noisy data was filtered, and performance metrics were calculated and summarized as averaged values, over a number of whole cycles of actuation to account for periodic phenomena.

The velocity of the gantry along the x -axis was estimated using backwards differentiation of the smoothed (10^{th} order Savitzky-Golay filter) linear displacement.

$$u(t) = \frac{x(t) - x(t-1)}{\tau}, \quad (22)$$

where x is the gantry's position along x at times t and $t-1$, and τ is the time increment.

The slip ratio was used to evaluate the traction quality of the actuator based on [134]:

$$S = \begin{cases} \frac{r\omega - u}{r\omega} & , r\omega > u: \text{accelerating} \\ \frac{r\omega - u}{ru} & , r\omega < u: \text{braking} \end{cases} \quad (23)$$

Assuming no braking during the range of data, the slip ratio of the wheel was calculated as:

$$s(t) = \frac{r\omega(t) - u(t)}{r\omega(t)}, \quad (24)$$

where r is the deformed actuator's radius, assuming a constant curvature, $u(t)$ is the gantry's instantaneous velocity along the x direction, and $\omega(t)$ is the angular velocity of the motor shaft.

To evaluate the actuator's energy characteristics, the Cost of Transport metric was used:

$$CoT = \frac{\overline{P}_{in}}{mg\bar{u}} = \frac{1}{nT} \frac{\int_0^{nT} VI(t)dt}{mg \int_0^{nT} u(t)dt}. \quad (25)$$

Here $m = 2.15\text{ kg}$ is the mass of the actuator assembly excluding the gantry, and g is the acceleration of gravity.

Fig. 3.13 shows the results of the experimental characterization of the actuator's tractive behaviour. Fig. 3.12a shows indicative results from terrestrial experiments on sand with 6.25% water content. The jump that occurs when the actuator rolls over its seam (e.g., at 5 sec) is caused by the actuator digging into the sand, and can be corrected by increasing the internal pressure or further optimizing the actuator morphology. In general, with constant angular velocity of the motor, the actuator maintained a rather constant linear speed of the gantry.

Fig. 3.12b shows aggregated results of the entire parameter sweep for terrestrial experiments. These graphs show that increasing the motor's angular velocity results in higher linear velocity of the gantry, with a linear relationship for the two middle cases of water content, but not for the dry sand (0%) and the sand that was saturated with water (25%). This dependence on water content can also be observed in the slip ratio and Cost of Transport metrics, where the two edge sets perform significantly worse and the 6.25% set is consistently the lowest. This behaviour is supported by Fall et al. [135] that studied the effect that water content in sand has on its shear modulus, explaining the tractive characteristics of locomotion on sand with varying water content.

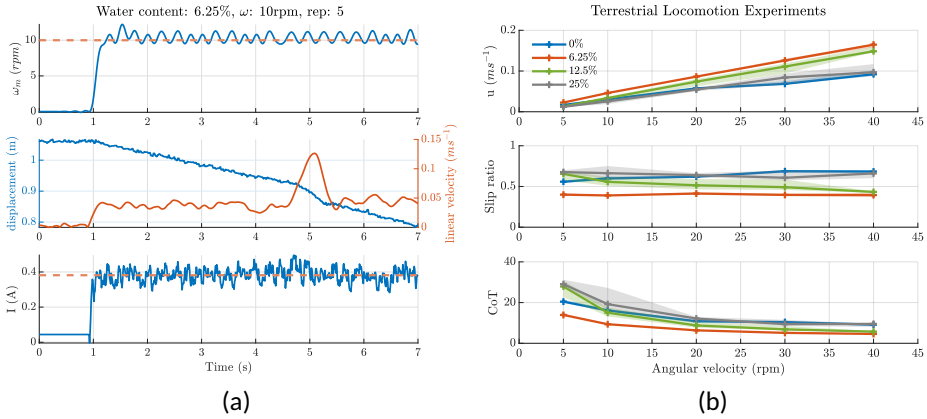


Figure 3.13: Experimental results of terrestrial velocity characterization with the variable stiffness actuator [Publication III]: (a) Indicative results. The upper graph shows the actual angular velocity of the actuator’s motor shaft. The dashed horizontal line denotes the desired angular velocity. The middle graph shows the temporal evolution of the gantry’s position along the rail as it moves towards the distance sensor, as well as the gantry’s velocity calculated based on (22). The lower graph shows the instantaneous current consumption in blue colour and the averaged as a red dashed line. (b) Parametric study of the full range of actuation speeds and water content levels. The crosses show the median values of 10 replicates for each parameter set, with 25th and 75th percentiles as shaded areas. The upper graph shows the linear velocity of the gantry for all angular velocities and all levels of water content in the soil. The middle and bottom graphs show the slip ratio and the Cost of Transport calculated based on (24) and (25) respectively.

3.4 Discussion and Conclusions

This chapter discussed the design, development and experimental evaluation of a soft fluidic actuator that can enable locomotion in aquatic and terrestrial environments, ranging from fully submerged swimming, to wet and dry granular terrains. Locomotion in this wide range of environmental conditions is enabled by the actuator’s built-in reconfigurable design that allows transitioning between two forms: soft paddle and wheel. We have experimentally evaluated our hypothesis that this design can achieve amphibious locomotion, by performing experiments in both target environments. Additionally, we investigated conditions that resemble the transition between the two, via experiments in terrestrial conditions with gradually increasing water content.

This work provided a proof-of-concept of a promising actuator design for amphibious locomotion. The low impact motion demonstrated during terrestrial locomotion experiments can be a great benefit, especially compared to most commonly found stiff-legged amphibious prototypes, and can positively affect a robot’s quality of motion, as well as the interaction with the environment. While the actuator’s performance is suboptimal in each individual locomotion scenario compared to more specialized prototypes, this trade-off is acceptable as it allows the reconfigurability of shape and stiffness that enables amphibious locomotion.

The limitations related to the suboptimal force generation during underwater swimming and the periodic phenomenon of digging into the soil during terrestrial locomotion, can be mitigated with optimization of the actuator’s morphology. This can be achieved with the help of a dynamic model, expanding on the FEM model presented here. Additionally, optimization of the motion planning and control schemes can further increase

performance.

In order for this actuator to be used as the main locomotion system of a robot, certain limitations need to be addressed. The transition between the two forms is currently achieved by a manual adjustment of the actuator's internal pressure. Most pneumatic actuators like the one presented use external pumps or other bulky systems for providing the pressure necessary to deform [136]. An onboard mechanism that will provide fluid pressure would allow tether-free actuation. This will increase the actuator's portability, and will enable the development of experimental prototypes with more degrees of freedom, leading up to the development of a prototype that can negotiate unconstrained terrestrial and aquatic locomotion in 6-DOF.

Specifically the contributions of the work described in this chapter include:

- The design of reconfigurable actuator design, its fabrication method, and experimental proof-of-concept of multi-modal amphibious locomotion.
- The material model selection and parameter identification for the silicone rubber used to fabricate the actuator, as well as other prototypes in this thesis, and experimental validation of the model.
- The experimental parametric analysis of the prototype's output and energetic characteristics, for two vastly different locomotion modes and over a range of kinematic inputs.

4 Conclusions and future outlook

This thesis aims to further the understanding of how variable stiffness can affect a soft actuator's efficacy and performance for locomotion. Incorporating soft materials in robot locomotion has considerable benefits, relating to safety and energy efficiency, as well as limitations relating to challenges in positional accuracy, state estimation, and force output. This thesis explores the concept of variable stiffness, as a means of mitigating these limitations and enabling reconfigurability for improved performance of soft actuators. The topic was investigated from three viewpoints studying actuators with different morphological characteristics in different locomotion scenarios. In each case, a prototype was designed, developed, and experimentally studied in underwater and/or terrestrial conditions.

The first investigation, described in [Publication I] and Section 2.1, focused on studying the effect of a non-uniform stiffness profile to the actuator's generated forces and energetic characteristics for underwater swimming. This study was based on the comparison between two soft actuators: an already existing soft pitching fin with a uniform stiffness profile, and a clone of that, which has higher flexural resistance in one of its edges. The hypothesis was that non-uniform stiffness throughout the actuator's body would affect its bending profile, changing the direction of the generated force towards the more rigid edge. The experimental evaluation demonstrated the expected shift in the proposed actuator's generated forces towards a more favourable direction, resulting in a higher force magnitude and propulsive efficiency. The main limitation of this prototype was that the change of stiffness was permanent, which may not be optimal for the robot's operation in general. This study shows that variable stiffness is a strategy that can be used for optimization of the actuator's output, and can be especially beneficial if coupled with a dynamic stiffness adjusting mechanism.

The second investigation, described in [Publication II] and Section 2.2, focused on studying the effect of a dynamically changing stiffness profile and shape, on the actuator's output for underwater swimming. Drag forces that are generated normal to the surface of an oscillating paddle actuator while it moves through water, usually have a larger magnitude than lift forces. However, due to being symmetric throughout the actuation cycle, they generate no net force. The motivation for this work was the hypothesis that an actuator design that allows an asymmetry in the drag force generation could be used to optimize the force output throughout an actuation cycle. For this purpose, a novel prototype actuator was introduced that comprises a thin rigid frame and a series of cascaded soft flaps. The experimental evaluation of the prototype demonstrated the expected deformation of the soft flaps due to the actuator's oscillations underwater. The deformation and subsequent asymmetry in the generated forces serve as proof-of-concept of the design, which enables a non-zero net force and allows to harness the drag force for thrust vectoring. Additionally, an experimental comparison with a more traditional soft foil demonstrated that the proposed actuator generates a larger surge force with higher propulsive efficiency, as the drag force component of the proposed actuator is dominant over the lift forces that are commonly used with soft foils for thrust vectoring. This study shows that adjusting the shape and stiffness of an actuator can result to optimized locomotion performance, and this adjustment can be achieved in a passive way, by leveraging on the materials and morphology of the actuator. The simplicity of motion planning and control for the proposed prototype further demonstrates the benefit of passively optimizing the drag forces.

Based on the findings mentioned above, the investigation was extended to a more diverse range of environmental conditions, studying the use of soft actuators with variable stiffness for amphibious locomotion. Most implementations for robotic amphibious locomotion rely on mechanically complex mechanisms, and/or mechanisms with fast moving

rigid parts, that can cause abrupt motions and can be damaging to the environment. In [Publication III] (and described in Chapter 3), a soft fluidic actuator was proposed, featuring a reconfigurable design that can easily modify its shape and stiffness. The hypothesis was that this reconfigurability would allow locomotion in aquatic and terrestrial conditions, with the actuator assuming a different form and performing a different motion profile in each case: an oscillating soft paddle for swimming and a rotating wheel for driving on ground. To validate the hypothesis, a prototype was designed, fabricated, and used to experimentally evaluate the performance of the actuator design. The experimental results show the actuator's ability to generate surge and tractive forces, through a parametric analysis of the actuator's output for a range of motion pattern parameters. This study demonstrates the benefits of reconfigurability of design, which enables multi-modal locomotion by easily adjusting the actuator's shape and stiffness. Specifically, it highlights that a rather simple mechanism that relies on simple motion planning and control algorithms, can be used to implement two different motion patterns and generate the required forces in two very different locomotion scenarios.

The next steps of work on this topic include studying variable stiffness actuation in locomotion scenarios with fewer motion restrictions on the actuator, and in conditions closer to "real-world". The prototypes described in this thesis were only evaluated in laboratory conditions, mostly using a single actuator and studying its output in one or two degrees of freedom, using a static setup without disturbances. It would be very valuable to extend the studies described in this thesis, using experimental setups that do not restrict motion, such as incorporating the actuator in a freely-moving robot platform and studying locomotion with multiple degrees of freedom. Additionally, studying locomotion under disturbances, such as underwater thrust vectoring under flow conditions, would be very interesting, as it would reveal dynamic phenomena that can affect robot locomotion. In order to bring the studied locomotion methods from the lab to the field, energetic and operational autonomy, as well as optimization of the actuators' output must be ensured. Specific to the work described in [Publication III], the actuator used external sources of power and pressure. To enable tether-free actuation, and to increase the autonomy of a vehicle using this actuator, a mechanism is needed that can provide the pressure to deform the actuator. Lastly, simulation of soft actuators and their interactions with their surroundings are rather limited in a robotics context. Several attempts have been made to simulate soft materials, however most of this work is either limited to very specific types of actuators and usually does not include interaction with the surroundings. For this purpose, further development work is needed to mature this area, and to allow dynamic simulations of compliant materials to become part of the process of design and development of soft actuators and their control systems.

To summarize, the work described in this thesis shows that designs with passive reconfigurability can lead to optimization of different aspects of an actuation system without increasing control and motion planning requirements. Hyperelastic materials, like silicone rubber, are very well suited for such purposes, due to their ability to withstand and recover from large deformations, to passively store and release energy, and to safely interact with their surroundings. While these characteristics are certainly desirable in applications where agile locomotion with minimal impact to the environment is required, the compliant behaviour of these materials can also introduce limitations relating to lower positional accuracy and challenging state estimation. This thesis shows how some of these drawbacks can be mitigated by dynamically varying the actuator's stiffness depending on the desired output.

List of Figures

1.1	Classification of fish swimming modes	18
2.1	The U-CAT robot	23
2.2	Illustration of generated forces on U-CAT's fins	24
2.3	CAD model of the studied U-CAT fins	24
2.4	Illustration of the fabrication process of the proposed fin	25
2.5	Position control structure for oscillatory pattern	25
2.6	Experimental setup and data acquisition system	26
2.7	Indicative experimental results with U-CAT fins	27
2.8	Parametric study of forces for a range of amplitudes and frequencies of oscillation with original and modified U-CAT fins	27
2.9	Early prototype of the flapped paddle-fin demonstrating the working principle of the soft flaps	29
2.10	Illustration of drag and lift forces acting on the flapped paddle-fin's surface during oscillation	30
2.11	The flapped paddle-fin prototype	31
2.12	Still frames of the flapped paddle fin in oscillation	32
2.13	Indicative experimental results of flapped paddle-fin and original soft fin ...	32
2.14	Parametric study of forces for a range of amplitudes and frequencies of oscillation with flapped paddle-fin and soft fin	33
2.15	The μ -CAT robot swimming underwater using flapped paddle-fins	34
2.16	Kinematic inputs for swimming gait trials with μ -CAT using flapped paddle-fin actuators	34
3.1	Illustration of concept vehicle using the variable stiffness actuator	36
3.2	Mould for casting dumbbell specimen for tensile test	37
3.3	Fabrication and uniaxial tensile testing of silicone specimens	38
3.4	Uniaxial tensile test data of silicone specimens (Elite Double 22 by Zhermack)	39
3.5	The fabrication process of a simplified variable stiffness actuator	40
3.6	Experimental model validation using simulated and physical actuator	41
3.7	The fabrication process of a variable stiffness actuator	42
3.8	The variable stiffness actuator final prototype	43
3.9	Experimental testbeds for locomotion performance evaluation of the variable stiffness actuator	43
3.10	Experimentally determined first natural frequencies of variable stiffness actuator	44
3.11	Velocity control structure for continuous rotations	45
3.12	Experimental results of underwater force characterization with the variable stiffness actuator	46
3.13	Experimental results of terrestrial velocity characterization with the variable stiffness actuator	48

References

- [1] R. Gkliva, M. Sfakiotakis, and M. Kruusmaa, "Development and experimental assessment of a flexible robot fin," in 2018 IEEE International Conference on Soft Robotics (RoboSoft), vol. 1, pp. 208–213, IEEE, 2018.
- [2] A. Simha, R. Gkliva, Ü. Kotta, and M. Kruusmaa, "A flapped paddle-fin for improving underwater propulsive efficiency of oscillatory actuation," IEEE Robotics and Automation Letters, vol. 5, no. 2, pp. 3176–3181, 2020.
- [3] R. Gkliva and M. Kruusmaa, "Soft fluidic actuator for locomotion in multi-phase environments," IEEE Robotics and Automation Letters, vol. 7, no. 4, pp. 10462–10469, 2022.
- [4] M. Kruusmaa, R. Gkliva, J. Tuhtan, A. Tuvikene, and J. Alfredsen, "Salmon behavioural response to robots in an aquaculture sea cage," Royal Society open science, vol. 7, no. 3, p. 191220, 2020.
- [5] W. Remmas, R. Gkliva, and A. Ristolainen, "Dynamic modelling of a screw actuator for improved locomotion control on various terrains." EGU General Assembly 2022, Vienna, Austria, 23-27 May, EGU22-5726, <https://doi.org/10.5194/egusphere-egu22-5726>, 2022.
- [6] B. Siciliano and O. Khatib, Springer Handbook of Robotics. Springer, 2008.
- [7] G. Antonelli, Underwater robots, vol. 3. Springer, 2014.
- [8] C. Nie, X. P. Corcho, and M. Spenko, "Robots on the move: Versatility and complexity in mobile robot locomotion," IEEE Robotics & Automation Magazine, vol. 20, no. 4, pp. 72–82, 2013.
- [9] L. Bruzzone and G. Quaglia, "Locomotion systems for ground mobile robots in unstructured environments," Mechanical sciences, vol. 3, no. 2, pp. 49–62, 2012.
- [10] M. Calisti, G. Picardi, and C. Laschi, "Fundamentals of soft robot locomotion," Journal of The Royal Society Interface, vol. 14, no. 130, p. 20170101, 2017.
- [11] D. Rus and M. T. Tolley, "Design, fabrication and control of soft robots," Nature, vol. 521, no. 7553, pp. 467–475, 2015.
- [12] C. Mai, S. Pedersen, L. Hansen, K. L. Jepsen, and Z. Yang, "Subsea infrastructure inspection: A review study," in 2016 IEEE International Conference on Underwater System Technology: Theory and Applications (USYS), pp. 71–76, IEEE, 2016.
- [13] S. Marras and M. Porfiri, "Fish and robots swimming together: attraction towards the robot demands biomimetic locomotion," Journal of The Royal Society Interface, vol. 9, no. 73, pp. 1856–1868, 2012.
- [14] J. Yuh, G. Marani, and D. R. Blidberg, "Applications of marine robotic vehicles," Intelligent service robotics, vol. 4, no. 4, pp. 221–231, 2011.
- [15] P. W. Webb, "Maneuverability-general issues," IEEE Journal of Oceanic Engineering, vol. 29, no. 3, pp. 547–555, 2004.
- [16] P. R. Bandyopadhyay, "Trends in biorobotic autonomous undersea vehicles," IEEE Journal of Oceanic Engineering, vol. 30, no. 1, pp. 109–139, 2005.

- [17] D. Roper, S. Sharma, R. Sutton, and P. Culverhouse, "A review of developments towards biologically inspired propulsion systems for autonomous underwater vehicles," Proceedings of the Institution of Mechanical Engineers, Part M: Journal of Engineering for the Maritime Environment, vol. 225, no. 2, pp. 77–96, 2011.
- [18] M. Sfakiotakis, D. M. Lane, and J. B. C. Davies, "Review of fish swimming modes for aquatic locomotion," IEEE Journal of oceanic engineering, vol. 24, no. 2, pp. 237–252, 1999.
- [19] D. S. Barrett, M. S. Triantafyllou, D. K. P. Yue, M. A. Grosenbaugh, and M. J. Wolfgang, "Drag reduction in fish-like locomotion," Journal of Fluid Mechanics, vol. 392, pp. 183–212, 1999.
- [20] J. Anderson and N. Chhabra, "Maneuvering and stability performance of a robotic tuna," Integrative and comparative biology, vol. 42, no. 1, pp. 118–126, 2002.
- [21] J. Liu, I. Dukes, and H. Hu, "Novel mechatronics design for a robotic fish," in 2005 IEEE/RSJ International Conference on Intelligent Robots and Systems, pp. 807–812, Aug 2005.
- [22] J. M. Kumph, M. Triantafyllou, M. Dos Santos, and D. Nugent, "Fast starting and maneuvering vehicles: Robopike and Robomuski," in International symposium on unmanned untethered submersible technology, pp. 439–445, University of New Hampshire-Marine systems, 1999.
- [23] H. El Daou, T. Salumäe, G. Toming, and M. Kruusmaa, "A bio-inspired compliant robotic fish: Design and experiments," in 2012 IEEE International Conference on Robotics and Automation, pp. 5340–5345, IEEE, 2012.
- [24] C. H. White, G. V. Lauder, and H. Bart-Smith, "Tunabot flex: a tuna-inspired robot with body flexibility improves high-performance swimming," Bioinspiration & Biomimetics, vol. 16, no. 2, p. 026019, 2021.
- [25] R. K. Katzschmann, J. DelPreto, R. MacCurdy, and D. Rus, "Exploration of underwater life with an acoustically controlled soft robotic fish," Science Robotics, vol. 3, no. 16, p. eaar3449, 2018.
- [26] A. Raj and A. Thakur, "Fish-inspired robots: design, sensing, actuation, and autonomy—a review of research," Bioinspiration & biomimetics, vol. 11, no. 3, p. 031001, 2016.
- [27] F. E. Fish, G. V. Lauder, R. Mittal, A. H. Techet, and M. S. Triantafyllou, "Conceptual design for the construction of a biorobotic AUV based on biological hydrodynamics," in 13th International Symposium on Unmanned Untethered Submersible Technology, Durham, NH, Aug, (Durham, USA), 2003. Aug. 24–27.
- [28] N. Kato, "Median and paired fin controllers for biomimetic marine vehicles," Applied Mechanics Reviews, vol. 58, no. 1–6, pp. 238–252, 2005.
- [29] M. Narasimhan and S. Singh, "Adaptive optimal control of an autonomous underwater vehicle in the dive plane using dorsal fins," Ocean Engineering, vol. 33, no. 3–4, pp. 404–416, 2006.

- [30] S. Hsu, C. Mailey, E. Eade, and J. Janet, "Autonomous control of a horizontally configured undulatory flap propelled vehicle," in 2003 IEEE International Conference on Robotics and Automation (Cat. No. 03CH37422), vol. 2, pp. 2194–2199, IEEE, 2003.
- [31] B. Hobson, M. Murray, and C. A. Pell, "Pilotfish: Maximizing agility in an unmanned-underwater vehicle," in International symposium on unmanned untethered submersible technology, (Durham, USA), pp. 41–51, 1999.
- [32] M. S. Triantafyllou, A. H. Techet, and F. S. Hover, "Review of experimental work in biomimetic foils," IEEE Journal of Oceanic Engineering, vol. 29, no. 3, pp. 585–594, 2004.
- [33] M. Sfakiotakis, R. Gliva, and M. Mountoufaris, "Steering-plane motion control for an underwater robot with a pair of undulatory fin propulsors," in 2016 24th Mediterranean Conference on Control and Automation (MED), (Athens, Greece), pp. 496–503, IEEE, 2016.
- [34] A. Chemori, K. Kuusmik, T. Salumäe, and M. Kruusmaa, "Depth control of the biomimetic U-CAT turtle-like AUV with experiments in real operating conditions," in Robotics and Automation (ICRA), 2016 IEEE International Conference on, pp. 4750–4755, IEEE, 2016.
- [35] J. H. Long Jr, J. Schumacher, N. Livingston, and M. Kemp, "Four flippers or two? tetrapodal swimming with an aquatic robot," Bioinspiration & Biomimetics, vol. 1, no. 1, p. 20, 2006.
- [36] N. Plamondon and M. Nahon, "A trajectory tracking controller for an underwater hexapod vehicle," Bioinspiration & biomimetics, vol. 4, no. 3, pp. 1–8, 2009.
- [37] Z. Shen, J. Na, and Z. Wang, "A biomimetic underwater soft robot inspired by cephalopod mollusc," IEEE Robotics and Automation Letters, vol. 2, no. 4, pp. 2217–2223, 2017.
- [38] A. Villanueva, C. Smith, and S. Priya, "A biomimetic robotic jellyfish (robojelly) actuated by shape memory alloy composite actuators," Bioinspiration & biomimetics, vol. 6, no. 3, p. 036004, 2011.
- [39] J. Najem, S. A. Sarles, B. Akle, and D. J. Leo, "Biomimetic jellyfish-inspired underwater vehicle actuated by ionic polymer metal composite actuators," Smart Materials and Structures, vol. 21, no. 9, p. 094026, 2012.
- [40] J. Hu, H. Li, and W. Chen, "A squid-inspired swimming robot using folding of origami," The Journal of Engineering, vol. 2021, no. 10, pp. 630–639, 2021.
- [41] Z. Chen, T. I. Um, J. Zhu, and H. Bart-Smith, "Bio-inspired robotic cownose ray propelled by electroactive polymer pectoral fin," in ASME International Mechanical Engineering Congress and Exposition, vol. 54884, pp. 817–824, 2011.
- [42] ETH Zurich, "Sepios: Riding the wave of progress," 2014.
- [43] T. Salumäe, A. Chemori, and M. Kruusmaa, "Motion control of a hovering biomimetic four-fin underwater robot," IEEE Journal of Oceanic Engineering, vol. 44, no. 1, pp. 54–71, 2019.

- [44] D. Wang, Y. Liu, J. Deng, S. Zhang, J. Li, W. Wang, J. Liu, W. Chen, Q. Quan, G. Liu, et al., "Miniature amphibious robot actuated by rigid-flexible hybrid vibration modules," Advanced Science, vol. 9, no. 29, p. 2203054, 2022.
- [45] U. Saranlı, M. Buehler, and D. E. Koditschek, "Rhex: A simple and highly mobile hexapod robot," The International Journal of Robotics Research, vol. 20, no. 7, pp. 616–631, 2001.
- [46] C. Georgiades, A. German, A. Hogue, H. Liu, C. Prahacs, A. Ripsman, R. Sim, L.-A. Torres, P. Zhang, M. Buehler, et al., "Aqua: an aquatic walking robot," in 2004 IEEE/RSJ International Conference on Intelligent Robots and Systems (IROS)(IEEE Cat. No. 04CH37566), vol. 4, pp. 3525–3531, IEEE, 2004.
- [47] X. Liang, M. Xu, L. Xu, P. Liu, X. Ren, Z. Kong, J. Yang, and S. Zhang, "The Amphi-Hex: A novel amphibious robot with transformable leg-flipper composite propulsion mechanism," in 2012 IEEE/RSJ International Conference on Intelligent Robots and Systems, pp. 3667–3672, IEEE, 2012.
- [48] L. Bai, G. Dou, W. Duan, Y. Sun, J. Zheng, and X. Chen, "Amphibious robot with a novel composite propulsion mechanism," in 2021 6th IEEE International Conference on Advanced Robotics and Mechatronics (ICARM), pp. 442–447, IEEE, 2021.
- [49] Y. Sun, S. Ma, and X. Luo, "Design of an eccentric paddle locomotion mechanism for amphibious robots," in 2010 IEEE International Conference on Robotics and Biomimetics, pp. 1098–1103, IEEE, 2010.
- [50] H.-L. Wang, X.-Y. Yan, G. Wang, Q.-F. Zhang, Q.-Y. Tian, and Y.-L. Fan, "Experimental research and floating gait planning of crablike robot," Advances in Mechanical Engineering, vol. 12, no. 2, p. 1687814020904853, 2020.
- [51] B. B. Dey, S. Manjanna, and G. Dudek, "Ninja legs: Amphibious one degree of freedom robotic legs," in 2013 IEEE/RSJ International Conference on Intelligent Robots and Systems, pp. 5622–5628, IEEE, 2013.
- [52] B. Zhong, S. Zhang, M. Xu, Y. Zhou, T. Fang, and W. Li, "On a CPG-based hexapod robot: AmphiHex-II with variable stiffness legs," IEEE/ASME Transactions on Mechatronics, vol. 23, no. 2, pp. 542–551, 2018.
- [53] A. S. Boxerbaum, P. Werk, R. D. Quinn, and R. Vaidyanathan, "Design of an autonomous amphibious robot for surf zone operation: part i mechanical design for multi-mode mobility," in Proceedings, 2005 IEEE/ASME International Conference on Advanced Intelligent Mechatronics., pp. 1459–1464, IEEE, 2005.
- [54] M. A. Klein, A. S. Boxerbaum, R. D. Quinn, R. Harkins, and R. Vaidyanathan, "Seadog: A rugged mobile robot for surf-zone applications," in 2012 4th IEEE RAS & EMBS International Conference on Biomedical Robotics and Biomechanics (BioRob), pp. 1335–1340, IEEE, 2012.
- [55] A. R. Vogel, K. N. Kaipa, G. M. Krummel, H. A. Bruck, and S. K. Gupta, "Design of a compliance assisted quadrupedal amphibious robot," in 2014 IEEE International Conference on Robotics and Automation (ICRA), pp. 2378–2383, IEEE, 2014.
- [56] T. Kim, Y.-w. Song, S. Song, and S.-C. Yu, "Underwater walking mechanism of underwater amphibious robot using hinged multi-modal paddle," International Journal of Control, Automation and Systems, vol. 19, no. 4, pp. 1691–1702, 2021.

- [57] R. L. Baines, J. W. Booth, F. E. Fish, and R. Kramer-Bottiglio, "Toward a bio-inspired variable-stiffness morphing limb for amphibious robot locomotion," in 2019 2nd IEEE International Conference on Soft Robotics (RoboSoft), pp. 704–710, IEEE, 2019.
- [58] T. Paschal, M. A. Bell, J. Sperry, S. Sieniewicz, R. J. Wood, and J. C. Weaver, "Design, fabrication, and characterization of an untethered amphibious sea urchin-inspired robot," IEEE Robotics and Automation Letters, vol. 4, no. 4, pp. 3348–3354, 2019.
- [59] A. A. M. Faudzi, M. R. M. Razif, G. Endo, H. Nabae, and K. Suzumori, "Soft-amphibious robot using thin and soft McKibben actuator," in 2017 IEEE International Conference on Advanced Intelligent Mechatronics (AIM), pp. 981–986, IEEE, 2017.
- [60] E. Milana, B. Van Raemdonck, K. Cornelis, E. Dehaerne, J. De Clerck, Y. De Groof, T. De Vil, B. Gorissen, and D. Reynaerts, "Eelworm: A bioinspired multimodal amphibious soft robot," in 2020 3rd IEEE International Conference on Soft Robotics (RoboSoft), pp. 766–771, IEEE, 2020.
- [61] D. K. Patel, X. Huang, Y. Luo, M. Mungekar, M. K. Jawed, L. Yao, and C. Majidi, "Highly dynamic bistable soft actuator for reconfigurable multimodal soft robots," Advanced Materials Technologies, p. 2201259, 2022.
- [62] H. Lipson, "Challenges and opportunities for design, simulation, and fabrication of soft robots," Soft Robotics, vol. 1, no. 1, pp. 21–27, 2014.
- [63] F. Chen and M. Y. Wang, "Design optimization of soft robots: A review of the state of the art," IEEE Robotics & Automation Magazine, vol. 27, no. 4, pp. 27–43, 2020.
- [64] C. J. Esposito, J. L. Tangorra, B. E. Flammang, and G. V. Lauder, "A robotic fish caudal fin: effects of stiffness and motor program on locomotor performance," Journal of Experimental Biology, vol. 215, no. 1, pp. 56–67, 2012.
- [65] A. Jusufi, D. M. Vogt, R. J. Wood, and G. V. Lauder, "Undulatory Swimming Performance and Body Stiffness Modulation in a Soft Robotic Fish-Inspired Physical Model," Soft robotics, vol. 4, pp. 202–210, sep 2017.
- [66] Z. Wolf, A. Jusufi, D. M. Vogt, and G. V. Lauder, "Fish-like aquatic propulsion studied using a pneumatically-actuated soft-robotic model," Bioinspiration and Biomimetics, vol. 15, p. 046008, jul 2020.
- [67] Y. Tang, Y. Chi, J. Sun, T.-H. Huang, O. H. Maghsoudi, A. Spence, J. Zhao, H. Su, and J. Yin, "Leveraging elastic instabilities for amplified performance: Spine-inspired high-speed and high-force soft robots," Science Advances, vol. 6, no. 19, p. eaaz6912, 2020.
- [68] Y.-J. Park and K.-J. Cho, "Design and manufacturing a bio-inspired variable stiffness mechanism in a robotic dolphin," in International Conference on Intelligent Robotics and Applications, pp. 302–309, Springer, 2013.
- [69] Y.-J. Park, T. M. Huh, D. Park, and K.-J. Cho, "Design of a variable-stiffness flapping mechanism for maximizing the thrust of a bio-inspired underwater robot," Bioinspiration & biomimetics, vol. 9, no. 3, p. 036002, 2014.
- [70] M. J. McHenry, C. A. Pell, and J. H. Long, "Mechanical control of swimming speed: stiffness and axial wave form in undulating fish models," The Journal of experimental biology, vol. 198, no. Pt 11, pp. 2293–305, 1995.

- [71] M. Ziegler, M. Hoffmann, J. P. Carbajal, and R. Pfeifer, "Varying body stiffness for aquatic locomotion," in 2011 IEEE International Conference on Robotics and Automation, pp. 2705–2712, IEEE, 2011.
- [72] S. Kobayashi, T. Ozaki, M. Nakabayashi, H. Morikawa, and A. Itoh, "Bioinspired aquatic propulsion mechanisms with real-time variable apparent stiffness fins," in 2006 IEEE International Conference on Robotics and Biomimetics, pp. 463–467, IEEE, 2006.
- [73] M. Nakabayashi, H. Soyano, S. Kobayashi, and H. Morikawa, "Bio-inspired aquatic propulsion mechanism using a fin with a variable-effective-length spring," Journal of Aero Aqua Bio-mechanisms, vol. 1, no. 1, pp. 104–110, 2010.
- [74] J.-S. Koh, E. Yang, G.-P. Jung, S.-P. Jung, J. H. Son, S.-I. Lee, P. G. Jablonski, R. J. Wood, H.-Y. Kim, and K.-J. Cho, "Jumping on water: Surface tension-dominated jumping of water striders and robotic insects," Science, vol. 349, no. 6247, pp. 517–521, 2015.
- [75] J. W. Hurst, J. E. Chestnutt, and A. A. Rizzi, "An actuator with physically variable stiffness for highly dynamic legged locomotion," in IEEE International Conference on Robotics and Automation, 2004. Proceedings. ICRA'04. 2004, vol. 5, pp. 4662–4667, IEEE, 2004.
- [76] K. C. Galloway, J. E. Clark, and D. E. Koditschek, "Design of a tunable stiffness composite leg for dynamic locomotion," in International Design Engineering Technical Conferences and Computers and Information in Engineering Conference, vol. 49040, pp. 215–222, 2009.
- [77] S. Chopra, M. T. Tolley, and N. Gravish, "Granular jamming feet enable improved foot-ground interactions for robot mobility on deformable ground," IEEE Robotics and Automation Letters, vol. 5, no. 3, pp. 3975–3981, 2020.
- [78] A. Sadeghi, A. Mondini, E. Del Dottore, A. K. Mishra, and B. Mazzolai, "Soft-legged wheel-based robot with terrestrial locomotion abilities," Frontiers in Robotics and AI, vol. 3, p. 73, 2016.
- [79] D. T. Kühnel, T. Helps, and J. Rossiter, "Kinematic analysis of vibrobot: a soft, hopping robot with stiffness-and shape-changing abilities," Frontiers in Robotics and AI, vol. 3, p. 60, 2016.
- [80] T. Umedachi, V. Vikas, and B. Trimmer, "Softworms: the design and control of non-pneumatic, 3d-printed, deformable robots," Bioinspiration & biomimetics, vol. 11, no. 2, p. 025001, 2016.
- [81] S. Seok, C. D. Onal, K.-J. Cho, R. J. Wood, D. Rus, and S. Kim, "Meshworm: a peristaltic soft robot with antagonistic nickel titanium coil actuators," IEEE/ASME Transactions on mechatronics, vol. 18, no. 5, pp. 1485–1497, 2012.
- [82] P. Wu, W. Jiangbei, and F. Yanqiong, "The structure, design, and closed-loop motion control of a differential drive soft robot," Soft robotics, vol. 5, no. 1, pp. 71–80, 2018.
- [83] E. Steltz, A. Mozeika, N. Rodenberg, E. Brown, and H. M. Jaeger, "JSEL: Jamming skin enabled locomotion," in 2009 IEEE/RSJ International Conference on Intelligent Robots and Systems, pp. 5672–5677, IEEE, 2009.

- [84] D. Zappetti, S. H. Jeong, J. Shintake, and D. Floreano, "Phase changing materials-based variable-stiffness tensegrity structures," Soft robotics, vol. 7, no. 3, pp. 362–369, 2020.
- [85] Y. Tang, Q. Zhang, G. Lin, and J. Yin, "Switchable adhesion actuator for amphibious climbing soft robot," Soft robotics, vol. 5, no. 5, pp. 592–600, 2018.
- [86] B. Zhong, S. Zhang, M. Xu, Y. Zhou, T. Fang, and W. Li, "On a cpg-based hexapod robot: Amphihex-ii with variable stiffness legs," IEEE/ASME Transactions on Mechatronics, vol. 23, no. 2, pp. 542–551, 2018.
- [87] R. Baines, S. K. Patiballa, J. Booth, L. Ramirez, T. Sipple, A. Garcia, F. Fish, and R. Kramer-Bottiglio, "Multi-environment robotic transitions through adaptive morphogenesis," Nature, vol. 610, no. 7931, pp. 283–289, 2022.
- [88] T. Salumäe, R. Raag, J. Rebane, A. Ernits, G. Toming, M. Ratas, and M. Kruusmaa, "Design principle of a biomimetic underwater robot U-CAT," in 2014 Oceans-St. John's, pp. 1–5, IEEE, 2014.
- [89] V. Preston, T. Salumäe, and M. Kruusmaa, "Underwater confined space mapping by resource-constrained autonomous vehicle," Journal of Field Robotics, vol. 35, no. 7, pp. 1122–1148, 2018.
- [90] T. Salumäe, A. Chemori, and M. Kruusmaa, "Motion control architecture of a 4-fin u-cat auv using dof prioritization," in 2016 IEEE/RSJ International Conference on Intelligent Robots and Systems (IROS), pp. 1321–1327, IEEE, 2016.
- [91] "EPOS2 Positioning Controllers Firmware Specification," 2017. www.maxongroup.com; accessed July, 2022.
- [92] "EPOS2 Positioning Controllers Application Notes," 2016. www.maxongroup.com; accessed July, 2022.
- [93] J. S. Palmisano, R. Ramamurti, J. D. Geder, M. Pruessner, W. C. Sandberg, and B. Ratna, "How to maximize pectoral fin efficiency by control of flapping frequency and amplitude," in 18th International Symposium on Unmanned Untethered Submersible Technology, pp. 124–132, 2013.
- [94] G. V. Lauder and E. D. Tytell, "Hydrodynamics of undulatory propulsion," Fish physiology, vol. 23, pp. 425–468, 2005.
- [95] C. Georgiades, M. Nahon, and M. Buehler, "Simulation of an underwater hexapod robot," Ocean Engineering, vol. 36, no. 1, pp. 39–47, 2009.
- [96] M. Sfakiotakis, J. Fasoulas, and R. Gliva, "Dynamic modeling and experimental analysis of a two-ray undulatory fin robot," in 2015 IEEE/RSJ International Conference on Intelligent Robots and Systems (IROS), pp. 339–346, IEEE, 2015.
- [97] C. Siegenthaler, C. Pradalier, F. Günther, G. Hitz, and R. Siegwart, "System integration and fin trajectory design for a robotic sea-turtle," in 2013 IEEE/RSJ International Conference on Intelligent Robots and Systems, pp. 3790–3795, IEEE, 2013.
- [98] B. Han, X. Luo, X. Wang, and X. Chen, "Mechanism design and gait experiment of an amphibian robotic turtle," Advanced Robotics, vol. 25, no. 16, pp. 2083–2097, 2011.

- [99] D. Font, M. Tresanchez, C. Siegentahler, T. Pallejà, M. Teixidó, C. Pradalier, and J. Palacin, "Design and implementation of a biomimetic turtle hydrofoil for an autonomous underwater vehicle," Sensors, vol. 11, no. 12, pp. 11168–11187, 2011.
- [100] P. Kodati, J. Hinkle, A. Winn, and X. Deng, "Microautonomous robotic ostraciiform (marco): Hydrodynamics, design, and fabrication," IEEE Transactions on Robotics, vol. 24, no. 1, pp. 105–117, 2008.
- [101] N. Kato, "Control performance in the horizontal plane of a fish robot with mechanical pectoral fins," IEEE journal of oceanic engineering, vol. 25, no. 1, pp. 121–129, 2000.
- [102] P. E. Sitorus, Y. Y. Nazaruddin, E. Leksono, and A. Budiyo, "Design and implementation of paired pectoral fins locomotion of labriform fish applied to a fish robot," Journal of Bionic Engineering, vol. 6, no. 1, pp. 37–45, 2009.
- [103] S.-H. Song, M.-S. Kim, H. Rodrigue, J.-Y. Lee, J.-E. Shim, M.-C. Kim, W.-S. Chu, and S.-H. Ahn, "Turtle mimetic soft robot with two swimming gaits," Bioinspiration & Biomimetics, vol. 11, no. 3, p. 036010, 2016.
- [104] S. B. A. Kashem, S. Jawed, J. Ahmed, and U. Qidwai, "Design and implementation of a quadruped amphibious robot using duck feet," Robotics, vol. 8, no. 3, p. 77, 2019.
- [105] B. Kwak and J. Bae, "Design of hair-like appendages and comparative analysis on their coordination toward steady and efficient swimming," Bioinspiration & Biomimetics, vol. 12, no. 3, p. 036014, 2017.
- [106] S. B. Behbahani and X. Tan, "Design and modeling of flexible passive rowing joint for robotic fish pectoral fins," IEEE Transactions on Robotics, vol. 32, no. 5, pp. 1119–1132, 2016.
- [107] G. V. Lauder, "Function of the caudal fin during locomotion in fishes: kinematics, flow visualization, and evolutionary patterns," American Zoologist, vol. 40, no. 1, pp. 101–122, 2000.
- [108] S. C. Licht, M. Wibawa, F. S. Hover, and M. S. Triantafyllou, "Towards amphibious robots: Asymmetric flapping foil motion underwater produces large thrust efficiently," tech. rep., Massachusetts Institute of Technology. Sea Grant College Program, 2009.
- [109] C. Meurer, A. Simha, Ü. Kotta, and M. Kruusmaa, "Nonlinear orientation controller for a compliant robotic fish based on asymmetric actuation," in 2019 International Conference on Robotics and Automation (ICRA), pp. 4688–4694, IEEE, 2019.
- [110] A. Healey, S. Rock, S. Cody, D. Miles, and J. Brown, "Toward an improved understanding of thruster dynamics for underwater vehicles," in Proceedings of IEEE Symposium on Autonomous Underwater Vehicle Technology (AUV'94), pp. 340–352, 1994.
- [111] C. Georgiades, "Simulation and control of an underwater hexapod robot," Master's thesis, McGill University, 2005.

- [112] B. Mosadegh, P. Polygerinos, C. Keplinger, S. Wennstedt, R. F. Shepherd, U. Gupta, J. Shim, K. Bertoldi, C. J. Walsh, and G. M. Whitesides, "Pneumatic networks for soft robotics that actuate rapidly," Advanced functional materials, vol. 24, no. 15, pp. 2163–2170, 2014.
- [113] F. Ilievski, A. D. Mazzeo, R. F. Shepherd, X. Chen, and G. M. Whitesides, "Soft robotics for chemists," Angewandte Chemie, vol. 123, no. 8, pp. 1930–1935, 2011.
- [114] B. Gorissen, D. Reynaerts, S. Konishi, K. Yoshida, J.-W. Kim, and M. De Volder, "Elastic inflatable actuators for soft robotic applications," Advanced Materials, vol. 29, no. 43, p. 1604977, 2017.
- [115] O. Yasa, Y. Tshimitsu, M. Y. Michelis, L. S. Jones, M. Filippi, T. Buchner, and R. K. Katzschmann, "An overview of soft robotics," Annual Review of Control, Robotics, and Autonomous Systems, vol. 6, 2022.
- [116] M. T. Tolley, R. F. Shepherd, B. Mosadegh, K. C. Galloway, M. Wehner, M. Karpelson, R. J. Wood, and G. M. Whitesides, "A resilient, untethered soft robot," Soft robotics, 2014.
- [117] J. Shintake, V. Cacucciolo, D. Floreano, and H. Shea, "Soft robotic grippers," Advanced materials, vol. 30, no. 29, p. 1707035, 2018.
- [118] X. Zhang and A. E. Oseyemi, "A herringbone soft pneu-net actuator for enhanced conformal gripping," Robotica, vol. 40, no. 5, pp. 1345–1360, 2022.
- [119] P. Polygerinos, S. Lyne, Z. Wang, L. F. Nicolini, B. Mosadegh, G. M. Whitesides, and C. J. Walsh, "Towards a soft pneumatic glove for hand rehabilitation," in 2013 IEEE/RSJ International Conference on Intelligent Robots and Systems, pp. 1512–1517, IEEE, 2013.
- [120] J. Ning, C. Ti, and Y. Liu, "Inchworm inspired pneumatic soft robot based on friction hysteresis," J. Robot. Autom., vol. 1, no. 1, pp. 54–63, 2017.
- [121] R. F. Shepherd, F. Ilievski, W. Choi, S. A. Morin, A. A. Stokes, A. D. Mazzeo, X. Chen, M. Wang, and G. M. Whitesides, "Multigait soft robot," Proceedings of the national academy of sciences, vol. 108, no. 51, pp. 20400–20403, 2011.
- [122] J. M. Florez, B. Shih, Y. Bai, and J. K. Paik, "Soft pneumatic actuators for legged locomotion," in 2014 IEEE International Conference on Robotics and Biomimetics (ROBIO 2014), pp. 27–34, IEEE, 2014.
- [123] M. Soliman, M. A. Mousa, M. A. Saleh, M. Elsamanty, and A. G. Radwan, "Modelling and implementation of soft bio-mimetic turtle using echo state network and soft pneumatic actuators," Scientific reports, vol. 11, no. 1, pp. 1–11, 2021.
- [124] ASTM International, West Conshohocken, PA, ASTM D412-16(2021), Standard Test Methods for Vulcanized Rubber and Thermoplastic Elastomers—Tension, 2021. www.astm.org.
- [125] L. Marechal, P. Balland, L. Lindenroth, F. Petrou, C. Kontovounisios, and F. Bello, "Toward a common framework and database of materials for soft robotics," Soft robotics, vol. 8, no. 3, pp. 284–297, 2021.

- [126] C. Tawk and G. Alici, "Finite element modeling in the design process of 3d printed pneumatic soft actuators and sensors," Robotics, vol. 9, no. 3, p. 52, 2020.
- [127] S. K. Melly, L. Liu, Y. Liu, and J. Leng, "A review on material models for isotropic hyperelasticity," International Journal of Mechanical System Dynamics, vol. 1, no. 1, pp. 71–88, 2021.
- [128] M. S. Xavier, A. J. Fleming, and Y. K. Yong, "Finite element modeling of soft fluidic actuators: Overview and recent developments," Advanced Intelligent Systems, vol. 3, no. 2, p. 2000187, 2021.
- [129] C. Renaud, J.-M. Cros, Z.-Q. Feng, and B. Yang, "The Yeoh model applied to the modeling of large deformation contact/impact problems," International Journal of Impact Engineering, vol. 36, no. 5, pp. 659–666, 2009.
- [130] P. Polygerinos, Z. Wang, J. T. Overvelde, K. C. Galloway, R. J. Wood, K. Bertoldi, and C. J. Walsh, "Modeling of soft fiber-reinforced bending actuators," IEEE Transactions on Robotics, vol. 31, no. 3, pp. 778–789, 2015.
- [131] P. Polygerinos, N. Correll, S. A. Morin, B. Mosadegh, C. D. Onal, K. Petersen, M. Cianchetti, M. T. Tolley, and R. F. Shepherd, "Soft robotics: Review of fluid-driven intrinsically soft devices; manufacturing, sensing, control, and applications in human-robot interaction," Advanced Engineering Materials, vol. 19, no. 12, p. 1700016, 2017.
- [132] soft robotics toolkit. <https://softroboticstoolkit.com/book/pneunets-fabrication>, accessed in: July, 2022.
- [133] F. Schmitt, O. Piccin, L. Barbé, and B. Bayle, "Soft robots manufacturing: A review," Frontiers in Robotics and AI, vol. 5, p. 84, 2018.
- [134] K. Yoshida and H. Hamano, "Motion dynamics and control of a planetary rover with slip-based traction model," in Unmanned Ground Vehicle Technology IV, vol. 4715, pp. 275–286, International Society for Optics and Photonics, 2002.
- [135] A. Fall, B. Weber, M. Pakpour, N. Lenoir, N. Shahidzadeh, J. Fiscina, C. Wagner, and D. Bonn, "Sliding friction on wet and dry sand," Physical review letters, vol. 112, no. 17, p. 175502, 2014.
- [136] B. Jumet, M. D. Bell, V. Sanchez, and D. J. Preston, "A data-driven review of soft robotics," Advanced Intelligent Systems, vol. 4, no. 4, p. 2100163, 2022.

Acknowledgements

I would like to thank my supervisor Prof. Maarja Kruusmaa, for giving me the opportunity to be part of her team and work on this subject. She provided guidance and support during my studies here, but also showed trust and enabled me to be independent and to take initiative and full responsibility for my work. Additionally, she provided countless opportunities for collaboration and networking, learning skills beyond my narrow field of research, and helped me develop as a researcher.

I would also like to thank all my colleagues and friends at the Centre for Biorobotics, who spent time and effort constantly teaching me new skills, helping me brainstorm, build, and troubleshoot hardware and software, and for helping me feel at home in Estonia.

The work presented in this thesis was financially supported by:

- the European Union's Research and Innovation programme Horizon 2020 project ROBOMINERS (grant agreement 820971),
- the European Union's MSCA-RISE scheme "Bio-inspired Technologies for a Sustainable Marine Ecosystem" (grant agreement 824043),
- the Estonian Research Council "Multiscale Natural Flow Sensing for Coasts and Rivers" (grant agreement PRG1243),
- IUT institutional research funding of the Estonian Ministry of Education and Research "Bio-inspired underwater robots" (IUT33-9),
- the ERA-NET FLAG-ERA JTC2016 partner Estonian Research Council, in the framework of RoboCom++
- The Archimedes foundation (Sihtasutus Archimedes) with the Dora+ short term mobility scholarship programme

Last but not least I want to thank my friends, family, and especially my parents and brother for always being there for me.

Appendix 1

Publication 1

R. Gkliva, M. Sfakiotakis, and M. Kruusmaa, "Development and experimental assessment of a flexible robot fin," in 2018 IEEE International Conference on Soft Robotics (RoboSoft), vol. 1, pp. 208–213, IEEE, 2018

Development and Experimental Assessment of a Flexible Robot Fin

Roza Gkliva¹, Michael Sfakiotakis² and Maarja Kruusmaa¹

Abstract—Energy efficiency and motion precision are particularly important for unmanned underwater vehicles (UUVs) undertaking complex missions. To achieve these objectives, researchers consider different materials when designing UUVs. In this work, we present the development and experimental assessment of a bio-inspired flexible actuator, based on the fins used in the Autonomous Underwater Vehicle U-CAT. The novel aspect of the new fin design is that it allows manipulation of the magnitude and direction of the generated thrust vector, by increasing the flexural resistance along its front edge through a rigid insert. The potential for using the fin as a U-CAT actuator is assessed through the comparison of results from parametric studies inside a water tank, run for both the here-proposed and the original design. The results indicate that the modified fin can generate an increased overall force, with a relatively small increase in power consumption. More interestingly, the overall direction of the thrust vector is better aligned with the robot's surge axis, at the expense of reducing the sway motion capability. Overall, the new design holds considerable potential for enhancing the propulsive performance of fin-actuated underwater vehicles, while representing a simple and robust implementation of undulating flexible propulsors.

I. INTRODUCTION

In recent years, there has been considerable interest by the scientific, research and industrial communities, in the development and use of unmanned robotic vehicles for remote access in underwater environments. The demand for energy efficiency and precise position control in the presence of drifting currents has prompted the development of bio-inspired solutions to replace the lift-based control surfaces or multi-thruster systems found in more traditional UUVs [1].

Bio-inspired propulsion designs for robotic underwater vehicles follow two main paradigms; the first emulating the continuously flexing fish bodies for increased propulsive efficiency [2], [3], [4], [5], and the second employing mechanical analogues of biological active appendages [6], [7]. Most of the systems in the second category include either pectoral or lateral, pitching or heaving fins [8], [9], [6], [10], [11], [12], [13], [14], [15], [16], based on the morphology and functionality of the fins and paddles of marine species, and have the potential to increase the robot's thrust vectoring capacity and energy efficiency, while maintaining a stealthy operation [6].

A distinction within the group of bio-inspired robots can be made, based on the properties of the materials used to

make their actuators. While rigid actuators were the norm in previous years, recently soft/flexible actuators are becoming more popular. In regards to the means of actuation of these propulsion mechanisms, in the relevant literature appears a plethora of different designs, fully actuated and not [6], [17]. The motivation for designing underactuated fins stems mainly from the desire to further study the kinematics of the fin, the generated force, and the resulting propulsive efficiency [18]. Taking advantage of the underactuated nature of these fins, we can study how varying the kinematic parameters affects the generated force, in regards to magnitude as well as direction.

In this context, this paper presents the development and experimental study of a flexible pitching fin, suitable for underwater robot propulsion. This actuator is a variant of the flexible fins used on the U-CAT robot [14], which was modified so that one of the edges perpendicular to the fin's axis of revolution remains rigid and oscillates along with the motor, while the other lags behind, forming an undulatory wave that transverses the fin diagonally from the rigid-leading edge towards the trailing edge. To assess this fin's efficacy, its force generating capacity and energy efficiency was experimentally compared to that of the existing U-CAT fins. This was done through a series of parametric experiments, where both the existing U-CAT actuator and the new one were placed in a laboratory water tank, fastened on a 4-axis force sensor and tested for the same range of kinematic parameters (frequency and amplitude of oscillation).

Our findings indicate that the modified fin affords increased overall force generation, at the expense of a relatively small increase in power consumption. More interestingly, the overall direction of the generated force vector is better aligned with the robot's surge axis, thereby improving the vehicle's forward thrust capacity; however, this also results in a reduction of the sway motion capability. Overall, the new design holds considerable potential for increasing the propulsive performance of fin-actuated underwater vehicles, and presents a simpler and more robust (albeit less versatile) implementation of undulating propulsive appendages, compared to multi-actuator designs [19], [20]

The remainder of this paper is structured as follows: Section II presents the design of the modified fin, along with the developed experimental setup. The results of the parametric tests conducted to assess the performance of the modified fin in comparison to the original design are detailed in Section III. Lastly, discussion and conclusions are presented in Section IV.

This work was supported by the ERA-NET FLAG-ERA JTC2016 partner Estonian Research Council, in the framework of RoboCom++.

¹Roza Gkliva and Maarja Kruusmaa are with the Centre for Biorobotics, Tallinn University of Technology, Tallinn, Estonia {roza.gkliva, maarja.kruusmaa}@ttu.ee

²Michael Sfakiotakis is with the Department of Electrical Engineering, Technological Educational Institute of Crete, Heraklion, Greece. msfak@staff.teicrete.gr

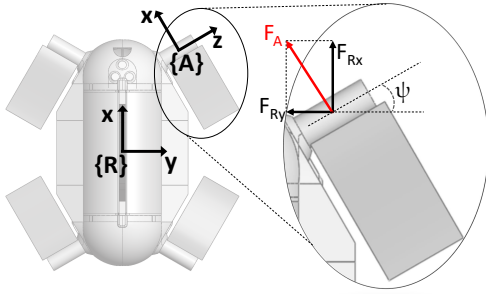


Fig. 1. U-CAT robot in hovering mode using the original fins. The overall vector F_A of the generated force is in the direction of the x -axis of the fin frame $\{A\}$.

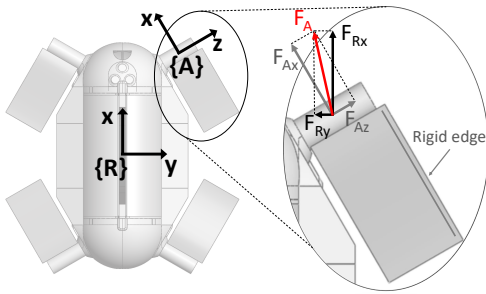


Fig. 2. U-CAT robot in hovering mode using the proposed fin. The overall vector F_A of the generated force involves components on both the x - and z -axis of the fin frame $\{A\}$, thereby increasing the force on the x -axis of the robot frame $\{R\}$.

II. EXPERIMENTAL DEVICE - DATA ACQUISITION

Fig. 1 shows a top view of the robot U-CAT in a configuration developed for hovering, where all fins are facing inwards. In this configuration, the robot uses its front fins to move forward. The placement of the fins at an angle $\psi = 30^\circ$ to the robot's body allows for its movement in 6 dof [21]. A disadvantage of this configuration is the loss in surge (related to the presence of the F_{Ry} component in Fig. 1 inset) that occurs because the force vectors generated by the fins are not parallel to the vehicle's surge direction (R_x). To minimize the drop in surge efficiency, a modified fin is proposed, that will generate a force vector not perpendicular to its axis of rotation, but better aligned to the surge direction (Fig. 2). The goal is to generate some amount of force along the actuator's axis of rotation, in the direction away from the robot, drawing the overall force F_A outwards, decreasing the loss (F_{Ry} in Fig. 2 inset) and increasing the fin's contributions along the surge axis.

Figs. 1, 2 show also the two frames of reference for all the force vectors used in this study. The robot's body frame $\{R\}$ has its x -axis parallel to the robot's surge axis pointing towards the front end of the robot. The fin's reference frame $\{A\}$ is attached with its z -axis aligned with the fin motor axis and the x -axis being on the $R_x R_y$ plane. This frame

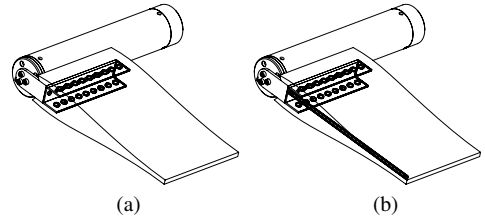


Fig. 3. CAD of the studied fins showing the internal structure: (a) Original fin. (b) Modified fin (rigid bar is visible near the outside edge).

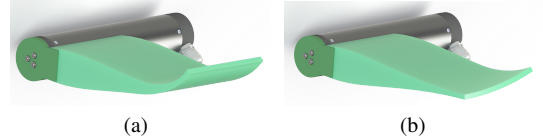


Fig. 4. CAD of the studied fins, illustrating their bending capabilities: (a) Original fin. (b) Modified fin.

$\{A\}$ is also used as reference for the experimental study as seen in Fig. 5. We define the fin's angular position θ as the rotation around the fin's z -axis with a starting reference of 0° when the fin's longitudinal axis is parallel to the A_x -axis.

A. Fin prototype

Both the original and the modified fins consist of a flexible silicone part (Zhermack Elite Double 22) cast around a rigid perforated base that can be fastened to the motor's shaft. The modified fin also contains a rigid bar along one of its edges (Fig. 3b). This bar differentiates considerably the bending profile of the modified fin compared to the original design. The modification results in an undulatory wave that transverses the fin diagonally from the rigid-leading edge towards its trailing edge (see Fig. 4b). It also makes the fin heavier by 6.3%, with the original fin weighing 0.429 kg and the modified 0.456 kg. The generated force's direction in pitching and undulatory fins is towards the leading edge. Because in this case the goal was to move the generated force's direction outwards, the rigid bar was placed near the outside edge of the fin.

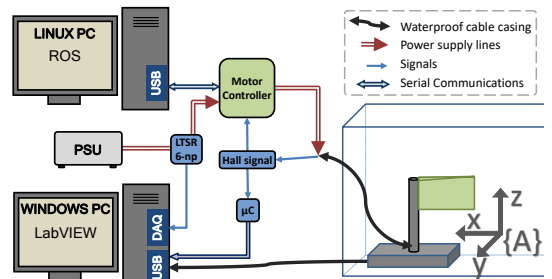


Fig. 5. The experimental setup.

B. Experimental Setup

The experimental setup used for this study can be separated into two interconnected sub-systems (Fig. 5). The first sub-system consists of a Linux computer, running ROS (Robot Operating System [22]), sending motion commands to the actuator's motor controller and recording all communications data. The second sub-system consists of a Windows computer running a custom LabVIEW Virtual Instrument (VI), that acquires data from the test-bed sensors. In the water tank, the actuator is attached on a custom-developed 4-axis force plate that measures forces along the x , y and z axes, as well as torque around the z -axis. The motor's Hall-effect sensors' signals are intercepted before the motor controller and used by a micro-controller to calculate its actual angular position. An LTSR 6-np (by LEM USA Inc.) current sensor configured to 3 primary turns (measuring ± 2 A) is used to measure the system's current consumption. Position feedback and current consumption data are sampled at 1 kHz, while the force plate data are sampled at 100 Hz.

The force plate was calibrated using a set of known weights and validated with a Lutron FG-5000A force gauge.

The motor used is the Maxon EC-max 30, a brushless EC motor with Hall sensors, controlled by the EPOS2 Module 36/2 digital positioning controller, which is powered by a Rohde & Schwarz HMP4040 power supply.

C. Experimental Protocol

The efficacy of the proposed actuator was evaluated through a series of parametric experiments, performed inside a laboratory test tank. The flexible actuator was fastened on the force plate (Fig. 6a) and positioned in the tank. Various combinations of kinematic parameters for the fin's oscillation frequency f and amplitude A were used, whose range was specified based on actuator performance limitations identified in previous experiments with the original fin [23]. While each kinematic parameter set is tested, the data acquisition system is recording the data. Both the original and the modified versions of the fin are tested on the same set of kinematic parameters with as close to the same experimental conditions as possible. This allows for later comparison of the results.

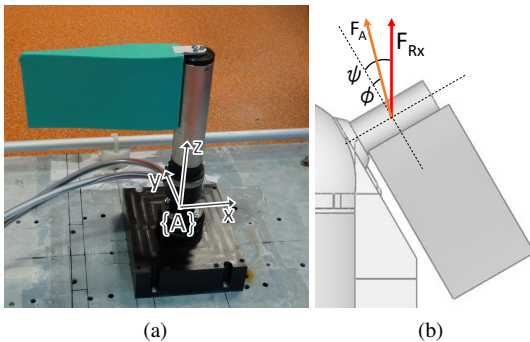


Fig. 6. (a) The modified fin mounted on the force plate, (b) The resulting force F_A and how it contributes to the robot's surge.

ROS handles the implementation of the fin kinematics as follows: a set of desired kinematic parameters for the fin's motion, amplitude and frequency, is sent over a specific topic, where the appropriate node is listening in. There, these parameters are used to calculate the motion profile velocity, acceleration and deceleration, taking into account the motor's gearbox ratio, as well as upper and lower limits for the motion profile's and kinematic parameters' values. The motion profile settings are then sent to the motor controller, where the control signal is generated.

Since actuator position feedback is provided by the motor's Hall sensor, before the start of each set of experiments, the fin has to be manually brought to the 0° position, i.e., oriented along the x -axis of $\{A\}$ -frame.

In each experimental run, the LabVIEW data acquisition VI is started first, followed by a new parameter set being sent to the motor controller. This ensures that the start of the experiment is captured in LabVIEW. The Labview VI runs for a set amount of time and then stops and prompts for the data to be saved. After that, the ROS nodes are terminated.

D. Data processing

The LabVIEW data were directly imported into MATLAB for post processing and analysis. There, a locally weighted linear regression ('lowess') filter was applied to smooth the noisy force (filter span: 10) and current consumption data (filter span: 90). Also, the first few transient periods of the measurements are discarded, as only the steady state is useful for mean value calculations. Specifically, for each measurement set, of the steady state range, 6 oscillation periods are used for further analysis.

The force components' timeseries were used to calculate the magnitude of the overall force vector [N] as:

$$F_A = \sqrt{F_{Ax}^2 + F_{Az}^2} \quad (1)$$

Given that the F_x and F_z components contribute to the robot's thrust, F_y is omitted from the overall force calculations. The angle of the resulting force was calculated according to [24] as:

$$\phi = \tan^{-1} \left(\frac{F_{Az}}{F_{Ax}} \right) \quad (2)$$

The angle of the resulting force was then used to calculate the force's contribution to the robot's surge, as shown in Fig. 6. The R_x component of force (F_{Rx}) is calculated as:

$$F_{Rx} = F_A \cos \phi', \quad (3)$$

where $\phi' = \psi - \phi$, is the angle between the resulting force F_A and robot's surge direction, and $\psi = 30^\circ$ is the actuator's angle to the robot's body (Fig. 6b).

The mean consumed power [W] was calculated given the voltage provided to the motor controller $V_m = 28[V]$ and the mean value of the measured current consumption, as:

$$P_{in,mean} = V_m I_{mean} \quad (4)$$

Subsequently, the static thrust/power ratio [N / W] of the fin, obtained as:

$$\eta = \frac{F_{Rx}}{P_{in,mean}} \quad (5)$$

was used as an indirect measure of the actuator's efficiency [25].

III. RESULTS

The experiments presented here were focused on assessing the modified fin's force generating capacity and propulsive efficiency. To achieve this, the processed results of the modified fin are compared to those of the original. The kinematic parameter space considered for the desired motion patterns involved combinations of $f = [0.5 : 0.3 : 2.6]$ Hz and $A = [10^\circ : 10^\circ : 60^\circ]$. While the motor controller achieved accurate position control for most parameter combinations, with position errors ranging between 0 – 3%, in some cases of combined high values of frequency and amplitude, the position error was large enough for the experiment to be considered not useful, so these sets were omitted for both fins in the following analysis.

A. Individual results

Individual results demonstrating the temporal evolution of the shaft's position, the current consumption and the force generated along the x , y , and z axes, by each fin for the same set of kinematic parameters, $A = 40^\circ$, $f = 1.7$ Hz, can be seen in Fig. 7. In this section all force vectors are in reference to the $\{A\}$ frame (Fig. 6a).

An initial large consumption can be observed during the first couple of periods of each experiment. This may be related to the fact that, during this time, the actuator has to start moving a previously still mass of water. The dashed red line in the same graph denotes the current consumption mean value, calculated for a number of whole periods of oscillations during steady state. Initial transient phenomena

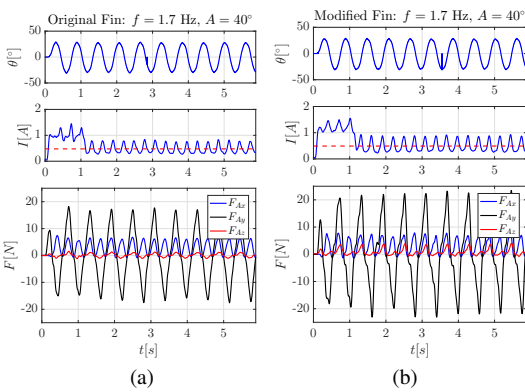


Fig. 7. Individual experimental results for position feedback, current consumption and generated forces along all 3 axes: (a) original fin, (b) modified fin

are observed in the force measurements, where steady state appears after less than two periods of oscillation.

For every period of the fins' motion, in all three axes, two peaks of force can be observed. For the F_{Ax} component, those peaks appear in the same direction, while for the F_{Ay} component, the peaks appear symmetrically across the 0 N line, for both fins. For the F_{Az} component, there appears a difference between the two fins, where in the original fin's case the peaks are symmetrical across the 0 N line, while for the modified fin the peaks have the same direction. This can be explained as zero net amount of force being generated along the z -axis for the original fin, and a non-zero amount for the modified. This way, for the modified fin, the F_{Ax} and F_{Az} components of the generated force appear to oscillate at twice the fin's oscillating frequency f , both generating a time-averaged non-zero net amount of force. Also, the F_{Az} measurements show that the fin produces consistently asymmetrical amounts of force when moving clockwise and counterclockwise. The F_{Ay} component of the force can be seen to oscillate at the same frequency as the fin in both cases. It should be noted that even though the sway component exhibits peaks that are considerably larger than the other two components, because it oscillates around 0 N, it produces zero net amount of force.

The force and current consumption measurements are closely linked to the angular position of the fin. All force components are minimized when the actuator comes to a stop in both cases, while maximum values are observed during the accelerating part of its motion. Similar patterns are observed in the current consumption graphs, where maximum values appear during the accelerating part and minimum values when it is stopped.

B. Parametric analysis

Figs. 8, 9 show the results of the parametric study for the effect of the kinematic parameters f and A on the magnitude of two of the three force components for both fins (as was noted previously, the F_{Ay} component produces zero amount of net force, so it will not be included here). These are mean force values calculated using a number of whole periods during the steady-state part of the time-series, as a function of the desired oscillation amplitude, over a range of frequencies. Fig. 10 shows mean values for the F_{Rx} component in the

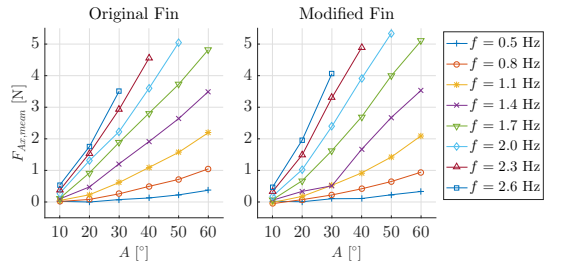


Fig. 8. Experimental results of the x -axis force component.

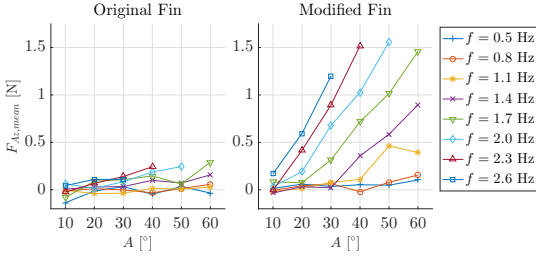


Fig. 9. Experimental results of the z -axis force component.

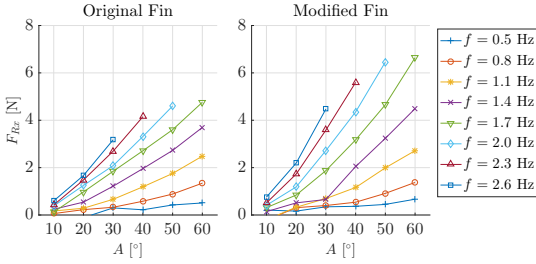


Fig. 10. Calculated force contribution to the robot's surge (F_{Rx}).

robot's surge direction, as calculated in (3). This is the fin's contribution to the robot's surge.

Both fins show similar trends when given the same kinematic parameters, i.e. increasing the oscillation amplitude or frequency results in an increase of the generated force. Comparing the two fins in these graphs, we observe that similar amounts of force are generated along the fin's positive x -axis, while, in contrast to the original fin, the modified variant exhibits a non-negligible force component in the positive z -axis direction.

The fin's contribution to the robot's surge (F_{Rx} , Fig. 10) shows a similar rising trend for increasing amplitude and frequency in both cases, with the modified fin generating larger amounts of force for higher values of the kinematic parameters. The non-zero positive force along the fin's z -axis draws the overall force's angle towards the robot's surge direction. This results in higher values of the generated forces along the robot's x -axis.

Fig. 11 shows the mean values for the current consumption measurements, calculated for a number of whole periods of oscillation. The modified fin shows higher values of consumption, over the original fin, for combinations of high values of the kinematic parameters. This can be attributed (at least partially) to the increased mass of the modified fin.

Results of the mean thrust/power ratio (5), used as an indirect metric of efficiency, can be seen in Fig. 12. The modified fin exhibits comparable η values for the lower frequencies, and significantly higher values for higher frequencies. This demonstrates that drawing the force vector towards the surge direction has a positive effect on the fin's contribution to the robot's thrust, even though the power consumption was

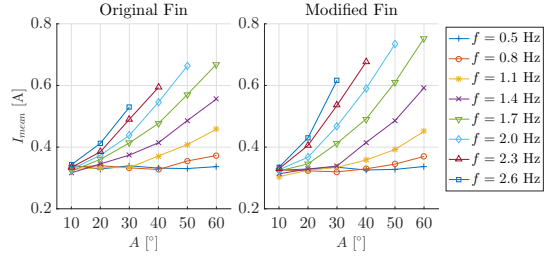


Fig. 11. Experimental results of current consumption.

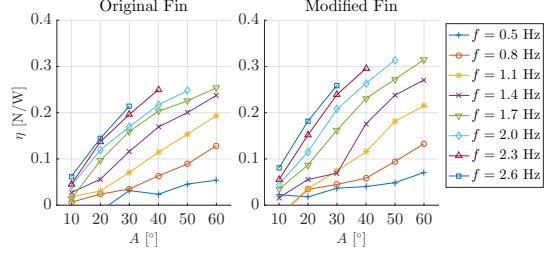


Fig. 12. Experimental results of the calculated thrust/power ratio.

higher in most cases for the modified fin.

IV. DISCUSSION AND CONCLUSIONS

We have presented the development of a flexible actuator intended for underwater propulsion, and its experimental comparison to the existing actuator of the U-CAT robot.

The assessment of the two flexible actuators shows that changing the way the actuator bends has an effect on not only the force output magnitude, but also on the force's direction. More specifically, these two fins react differently to changes in the kinematic parameters for their motion profile. Changing the kinematic parameters for the modified fin, alters not only the magnitude (as in the original fin) but also the direction of the generated force vector. This change is not directly controllable, as those two variables are coupled and depend on both kinematic parameters.

The comparison between the two demonstrates increased force generation by the modified fin, combined with higher thrust/power ratio. More specifically, the modified fin shows an increase of 39% in its contribution to the robot's surge F_{Rx} , for the highest observed value of this force for both fins ($A = 60^\circ$, $f = 1.70$ Hz). For the same parameter set the static thrust/power ratio η increases by 24%.

Regarding application to U-CAT, due to the robot's angled actuator configuration, the modified fins' characteristics would allow an increase in the generated surge force, e.g., for applications where forward thrust during hover mode is required. On the other hand, use of the modified fin would also result in a reduction of the force generated on the robot's y -axis, thereby diminishing the capacity for sway motion.

For this reason, future work will include the design, development and assessment of a flexible actuator capable

of dynamically manipulating the force vector's angle. This actuator will retain the advantage of 6-dof motion capability afforded by the original actuators, with the addition of the improved forward thrust of the here presented modified fin. These will be incorporated on the U-CAT AUV, to study low level control of the actuators, as well as relevant vehicle control schemes. Finally, future work will also involve the development of a mathematical model for the actuator, which will assist the optimization of its overall morphology and control design.

REFERENCES

- [1] D. Roper, S. Sharma, R. Sutton, and P. Culverhouse, "A review of developments towards biologically inspired propulsion systems for autonomous underwater vehicles," *Proceedings of the Institution of Mechanical Engineers, Part M: Journal of Engineering for the Maritime Environment*, vol. 225, no. 2, pp. 77–96, 2011.
- [2] D. S. Barrett, M. S. Triantafyllou, D. K. P. Yue, M. A. Grosenbaugh, and M. J. Wolfgang, "Drag reduction in fish-like locomotion," *Journal of Fluid Mechanics*, vol. 392, pp. 183–212, 1999.
- [3] J. Anderson and N. Chhabra, "Maneuvering and stability performance of a robotic tuna," *Integrative and comparative biology*, vol. 42, no. 1, pp. 118–126, 2002.
- [4] J. Liu, I. Dukes, and H. Hu, "Novel mechatronics design for a robotic fish," in *2005 IEEE/RSSJ International Conference on Intelligent Robots and Systems*, pp. 807–812, Aug 2005.
- [5] J. M. Kumph, M. Triantafyllou, M. Dos Santos, and D. Nugent, "Fast starting and maneuvering vehicles: Robopike and Robomuski," in *International symposium on unmanned untethered submersible technology*, pp. 439–445, University of New Hampshire-Marine systems, 1999.
- [6] P. Bandyopadhyay, "Trends in biorobotic autonomous undersea vehicles," *IEEE Journal of Oceanic Engineering*, vol. 30, no. 1, pp. 109–139, 2005.
- [7] F. E. Fish, G. V. Lauder, R. Mittal, A. H. Techet, and M. S. Triantafyllou, "Conceptual design for the construction of a biorobotic AUV based on biological hydrodynamics," in *13th International Symposium on Unmanned Untethered Submersible Technology, Durham, NH, Aug, 2003*.
- [8] N. Kato, "Median and paired fin controllers for biomimetic marine vehicles," *Applied Mechanics Reviews*, vol. 58, no. 1-6, pp. 238–252, 2005.
- [9] M. Narasimhan and S. Singh, "Adaptive optimal control of an autonomous underwater vehicle in the dive plane using dorsal fins," *Ocean Engineering*, vol. 33, no. 3-4, pp. 404–416, 2006.
- [10] S. Hsu, C. Mailey, E. Eade, and J. Janet, "Autonomous control of a horizontally configured undulatory flap propelled vehicle," in *2003 IEEE International Conference on Robotics and Automation (Cat. No.03CH37422)*, vol. 2, pp. 2194–2199, 2003.
- [11] B. Hobson, M. Murray, and C. A. Pell, "Pilotfish: Maximizing agility in an unmanned-underwater vehicle," in *International symposium on unmanned untethered submersible technology*, pp. 41–51, 1999.
- [12] M. S. Triantafyllou, A. H. Techet, and F. S. Hover, "Review of experimental work in biomimetic foils," *IEEE Journal of Oceanic Engineering*, vol. 29, no. 3, pp. 585–594, 2004.
- [13] M. Sfakiotakis, R. Gliva, and M. Mountoufaris, "Steering-plane motion control for an underwater robot with a pair of undulatory fin propulsors," in *2016 24th Mediterranean Conference on Control and Automation (MED)*, pp. 496–503, IEEE, 2016.
- [14] A. Chemori, K. Kuusmik, T. Salumäe, and M. Kruusmaa, "Depth control of the biomimetic u-cat turtle-like auv with experiments in real operating conditions," in *Robotics and Automation (ICRA), 2016 IEEE International Conference on*, pp. 4750–4755, IEEE, 2016.
- [15] J. H. Long Jr, J. Schumacher, N. Livingston, and M. Kemp, "Four flippers or two? tetrapodal swimming with an aquatic robot," *Bioinspiration & Biomimetics*, vol. 1, no. 1, p. 20, 2006.
- [16] N. Plamondon and M. Nahon, "A trajectory tracking controller for an underwater hexapod vehicle," *Bioinspiration & biomimetics*, vol. 4, no. 3, pp. 1–8, 2009.
- [17] W.-S. Chu, K.-T. Lee, S.-H. Song, M.-W. Han, J.-Y. Lee, H.-S. Kim, M.-S. Kim, Y.-J. Park, K.-J. Cho, and S.-H. Ahn, "Review of biomimetic underwater robots using smart actuators," *International journal of precision engineering and manufacturing*, vol. 13, no. 7, pp. 1281–1292, 2012.
- [18] H. Liu and O. Curet, "Propulsive performance of an under-actuated robotic ribbon fin," *Bioinspiration & Biomimetics*, 2017.
- [19] Y. Cai, S. Bi, and H. Ma, "Research on robotic fish propelled by oscillating pectoral fins," in *Robot Fish*, pp. 119–160, Springer, 2015.
- [20] G. V. Lauder and J. L. Tangorra, "Fish locomotion: biology and robotics of body and fin-based movements," in *Robot Fish*, pp. 25–49, Springer, 2015.
- [21] T. Salumäe, A. Chemori, and M. Kruusmaa, "Motion control architecture of a 4-fin U-CAT AUV using DOF prioritization," in *Intelligent Robots and Systems (IROS), 2016 IEEE/RSSJ International Conference on*, pp. 1321–1327, IEEE, 2016.
- [22] M. Quigley, K. Conley, B. Gerkey, J. Faust, T. Foote, J. Leibs, R. Wheeler, and A. Y. Ng, "ROS: an open-source robot operating system," in *ICRA workshop on open source software*, vol. 3, p. 5, Kobe, Japan, 2009.
- [23] T. Salumäe, A. Chemori, and M. Kruusmaa, "Motion control of a hovering biomimetic four-fin underwater robot," *IEEE Journal of Oceanic Engineering*, 2017.
- [24] B. Sprinkle, R. Bale, A. P. S. Bhalla, M. A. MacIver, and N. A. Patankar, "Hydrodynamic optimality of balistiform and gymnotiform locomotion," *European Journal of Computational Mechanics*, pp. 1–13, 2017.
- [25] J. S. Palmisano, R. Ramamurti, J. D. Geder, M. Pruessner, W. C. Sandberg, and B. Ratna, "How to maximize pectoral fin efficiency by control of flapping frequency and amplitude," in *18th International Symposium on Unmanned Untethered Submersible Technology*, 2013.

Appendix 2

Publication II

A. Simha, R. Gkliva, Ü. Kotta, and M. Kruusmaa, "A flapped paddle-fin for improving underwater propulsive efficiency of oscillatory actuation," IEEE Robotics and Automation Letters, vol. 5, no. 2, pp. 3176–3181, 2020

A Flapped Paddle-Fin for Improving Underwater Propulsive Efficiency of Oscillatory Actuation

Ashutosh Simha , Roza Gkliva , Ülle Kotta , and Maarja Kruusmaa 

Abstract—This letter presents a novel design of an oscillatory fin for thrust-efficient and agile underwater robotic locomotion. We propose a flat paddle-fin comprising a set of overlapping cascaded soft flaps that open in one half of the stroke cycle and close in the other. Consequently, asymmetry in the lateral drag force exerted by the fin during oscillatory actuation is passively achieved. This enables a substantially higher degree of efficiency in force generation than conventional oscillatory fins which rely on weaker longitudinal wake-induced forces. Experimental results show a high degree of improvement in net thrust and propulsive-efficiency over conventional fins. Locomotion with the proposed fin has been demonstrated on an underwater robotic platform. Various gaits were achieved using oscillatory actuation, via angular and phase offsets between the actuators.

Index Terms—Biologically-inspired robots, marine robotics, mechanism design.

I. INTRODUCTION

AUTONOMOUS Underwater Vehicles (AUVs) have been increasingly finding application in missions requiring a high degree of agility and endurance which has motivated a wide range of biologically inspired designs [1]. These AUVs can be broadly classified into jet-propulsion systems, modeled after jellyfish, scallops, octopus ([2]–[4]), undulatory systems, modeled after snakes and manta-rays etc. ([5]–[10]) and oscillatory systems modeled after fish classes such as Carangiforms, Thunniforms and Osstraciiforms ([11]–[13]).

Oscillatory AUVs generate thrust by utilizing the wake-induced forces due to fin oscillations [14]. At low inflow conditions, these forces are significantly weaker than the drag-induced lateral force that acts perpendicular to the fin. The lateral force however, can not be used for locomotion as it is symmetric in the stroke-cycle and produces zero net acceleration. For this reason, a class of AUVs which feature asymmetry in the lateral

force during the *power-stroke* and *recovery-stroke* half cycles are presented in [15]–[21].

In order to achieve asymmetric drag force without complex actuation or gait shaping involving multiple actuated joints, the following robots have been designed. In [22], [23], the actuator comprises rigid flaps that open and close during the power and recovery stroke. In [24], asymmetry is achieved using a spring loaded passive rowing joint which is swept back to offer less resistance to flow during the recovery stroke. In [22] and [23], it can be observed that during the recovery-stroke, the flaps are not completely parallel to the flow as they are required to open again during the power-stroke. This results in nontrivial drag during recovery. Moreover, due to the inertia of the rigid flaps, some of the energy during the power-stroke is utilized for opening them up. Further in [24], a nontrivial drag force from the fluid is required to sweep the fin towards the body during the recovery stroke due to the torsional spring.

Another method of achieving asymmetric drag force with conventional fins is in employing skewed actuation signals having a faster power stroke and a slower recovery stroke. Some works in this direction are [25]–[28]. However, increasing asymmetry necessitates a significantly smaller duty cycle of the power stroke, and oscillation frequency, resulting in intermittent and slower motion.

In this letter we propose a novel *flapped paddle-fin* that comprises a rigid thin frame, with cascaded flaps bending open during the recovery-stroke and closing during the power-stroke (Fig. 1). This design is inspired by the cascaded structure of the feathers on a bird's wing which overlap in a louver-like structure [29], [30]. The flapped paddle-fin (or *lowered fin*) has the following advantages over earlier designs:

- **Simplicity in design:** The proposed fin requires simple oscillatory actuation without complex stroke shaping mechanisms, and with a single actuated joint.
- **Negligible recovery drag:** The asymmetry in lateral force is high as the flaps are almost parallel to the flow during the recovery stroke, creating negligible drag.
- **Efficient power utilization:** The negligible inertia of the flaps allows them to open and close freely, enabling almost total utilization of on-board power for locomotion, thereby increasing efficiency.
- **Modeling simplicity:** Negligible inertia and drag during recovery and flat plate dynamics during the power stroke, allow reliable force modeling, thereby providing potential for accurate model based control.

Manuscript received September 10, 2019; accepted February 11, 2020. Date of publication February 21, 2020; date of current version March 5, 2020. This letter was recommended for publication by Associate Editor Prof. M. Dunbabin and Editor Prof. Jonathan Roberts upon evaluation of the reviewers' comments. This work was supported in part by the Estonian Research Council in the framework of ETAG17107 and in part by Institutional Research funding IUT339. (*Ashutosh Simha and Roza Gkliva, contributed equally to this work.*) (Corresponding author: Ashutosh Simha.)

Ashutosh Simha and Ülle Kotta are with the Department of Software Science, Tallinn University of Technology, 12616 Tallinn, Estonia (e-mail: ashutosh.iisc@gmail.com; kotta@cc.ioc.ee).

Roza Gkliva and Maarja Kruusmaa are with the Centre for Biorobotics, Department of Computer Systems, Tallinn University of Technology, 12616 Tallinn, Estonia (e-mail: roza.gkliva@ttu.ee; maarja.kruusmaa@ttu.ee).

Digital Object Identifier 10.1109/LRA.2020.2975747

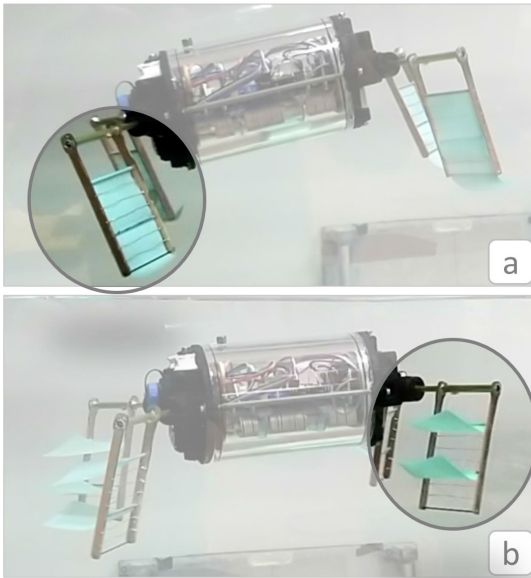


Fig. 1. Flapped paddle-fin based robot (a) flaps close during power-stroke, (b) flaps open during recovery-stroke.

In what follows we describe the mechanical design of the fin and its mathematical model, demonstrate the fin's efficiency by conducting comparative experiments with a conventional soft fin. Finally, we demonstrate how the fins can be utilized on an AUV for generating various gaits.

II. DESIGN CONCEPT

A. Forces Due to Oscillatory Motion

The primary hydrodynamic forces that are generated from oscillatory motion of the fin are due to drag, and the wake effect [14], [31], [32]. The drag force is exerted on the fin by the fluid that is laterally displaced during oscillation, and acts perpendicular to the surface of the fin. For a conventional rigid fin, the resultant drag-force components that are perpendicular to the longitudinal axis of the fin average out to zero over the stroke cycle. This force therefore produces no net thrust, and consequently can not be utilized for locomotion. The force that is used for locomotion is the second one, due to the wake-effect. As explained in [14] (see Fig. 11.4), this wake-force is generated when the fin oscillates in a nonzero inflow velocity regime. In this case, the oscillatory motion of the fin's trailing edge generates a wake behind the fin, into which momentum is imparted. This momentum that is shed off the trailing edge of the fin, and the resulting force, are linear with respect to the inflow velocity (or the forward swimming velocity of the robot). Kinetic energy imparted into the wake (wake power) is given by [14] as

$$P = \frac{1}{2} m_v w^2 U, \quad (1)$$

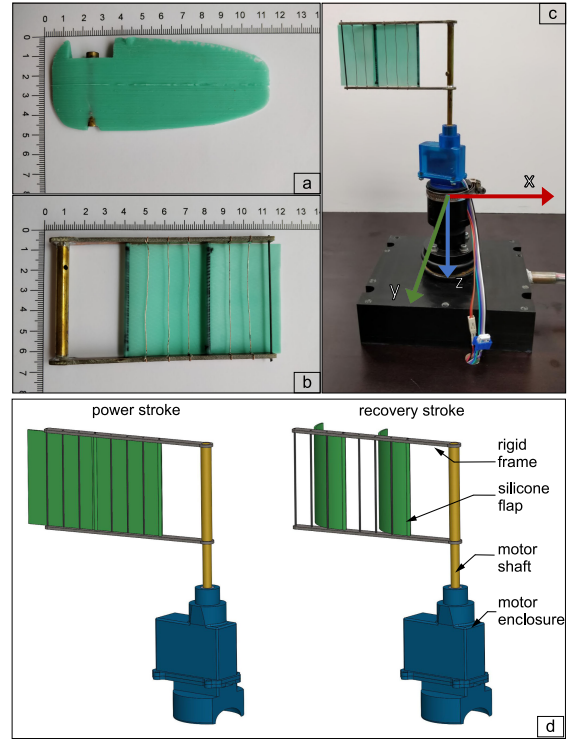


Fig. 2. Studied fins: (a) soft fin, (b) flapped paddle-fin, (c) Fin prototype mounted on force/torque test bed, (d) CAD illustration of the two states of the fin prototype, recovery and power-stroke.

where m_v is the virtual mass per unit length of the fin tip, w is the perpendicular velocity of the tail segment, and U is the forward swimming speed (or inflow velocity).

From the above discussion, it is evident that the wake-power is not significant at low swimming speeds. However, the lateral forces, though producing no net thrust, have a much higher magnitude, compared to the force corresponding to the above mentioned wake-power. This is observed in several other oscillatory fins (see for e.g. Fig. 8 in [33] and Fig. 7 in [34]).

B. Design and Fabrication

In order to generate highly asymmetric drag forces, the louvered fin is designed such that during the power-stroke, passive flaps are pressed against a rigid structure and form a flat paddle, and during the recovery-stroke the flaps are bent away from the fin structure, allowing water to flow through. The proposed fin (Fig. 2b) consists of a rigid frame and a series of flexible flaps. The flaps are assembled on the rigid frame in a cascaded configuration and slightly overlap in length.

Each flap is manufactured by casting silicone (Zhermack Elite Double 22) in an open rectangular mould. A flat surface is used to apply even pressure to the top of the mould. This results in curing a thin light-weight silicone sheet of uniform thickness.

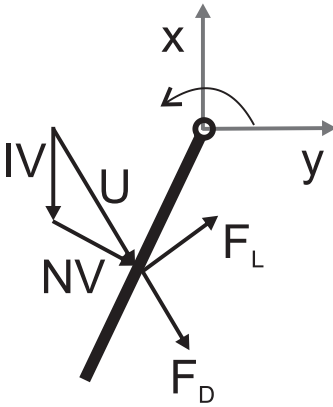


Fig. 3. Representation of drag and lift forces acting on the fin's surface during oscillation.

Before casting, a carbon fibre rod that has been covered in thread, is placed in the mould in a depression near one of the edges. The thread provides a rough surface for better adhesion between the silicone and the carbon fibre rod. This rod is used to mount the flap on the rigid frame and functions as the leading edge of the flap, and is constrained from rotating. The stiffness of the flap near the leading edge prevents it from folding over in the recovery stroke. Moreover, before casting, a piece of thin net is placed throughout the surface of the mould. This gets embedded in the silicone and adds to the flap's structural stability. The rigid frame is made of two copper-clad PCB strips on each side soldered on a brass tube. Additional support wires are placed across the frame, to prevent the flaps from passing through the gaps during the power-stroke.

The proposed fin has been compared with a conventional soft fin (Fig. 2(a)), which consists of a flexible silicone part cast around a brass tube used for mounting on the motor shaft.

III. MODELING OF FORCES OF FLAPPED PADDLE-FIN

The significant force that acts during oscillation on the flapped paddle-fin at low speed locomotion, is the drag force F_D which is exerted in a direction collinear with the net flow velocity U , which is the sum of the normal fluid velocity due to flapping NV and external inflow IV as indicated in Fig. 3. Under zero external flow condition, F_D is perpendicular to the fin's surface i.e. in the lateral direction. A secondary force F_L is also exerted perpendicular to drag. At low inflow conditions however F_L is appreciably small compared to F_D , and is therefore not incorporated into the mathematical model. Moreover, modeling this force precisely is indeed a nontrivial task for the asymmetric fin, and it is therefore subsequently considered as a small residual force for control design.

The drag force on the fin is calculated by dividing the fin's surface into several segments along the length of the fin, and the drag force due to each segment is computed according to a standard form-drag (quadratic) model [14], and subsequently

integrated along the length. Let w denote the (uniform) width of each segment that is exposed to the flow during oscillation. The width of the flap area that impedes the flow during the power stroke is calculated to be 6 cm during the power stroke, and estimated to be 0.6 cm during the recovery-stroke. This is because most of the flap area does not impede the flow during recovery, however there is a residual impedance from the frame and parts of the flaps near the hinges. We denote the drag coefficient in water as C_d , the density as $\rho = 997 \text{ Kg/m}^3$, and the instantaneous angular displacement of the fin by $\theta(t)$. The flap area in the fin is calculated to be within 3 cm to 10 cm of its length. Let ds denote the incremental length. Then, the drag force is given by

$$F_D(t) = \int_{0.03}^{0.1} \frac{1}{2} C_d \rho w \dot{\theta}^2(t) s^2 ds. \quad (2)$$

It is assumed that the power-stroke occurs when θ decreases and recovery-stroke occurs when θ increases. We obtain the lateral force during the power-stroke as

$$\begin{aligned} F_D(t) &= \frac{1}{2} C_d \rho w \dot{\theta}^2(t) \left[\frac{s^3}{3} \right]_{0.03}^{0.1} \\ &= 9.1 \times 10^{-5} C_d \rho \dot{\theta}^2(t). \end{aligned} \quad (3)$$

During the recovery-stroke we obtain the lateral force by using $w = 0.6 \text{ cm}$ as

$$F_D(t) = -9.1 \times 10^{-6} C_d \rho \dot{\theta}^2(t). \quad (4)$$

The components of the force in the body-fixed frame of the force-plate is obtained (under zero inflow conditions) as

$$\begin{aligned} F_x(t) &= F_D(t) \sin(\theta(t)), \\ F_y(t) &= F_D(t) \cos(\theta(t)). \end{aligned} \quad (5)$$

The angular displacement is achieved by using a proportional control law for the motor with reference

$$\theta_r = -\frac{A}{2} \sin(2\pi f t). \quad (6)$$

IV. EXPERIMENTAL SETUP

The efficacy of the flapped paddle-fin was initially assessed via a series of experiments using a force/torque measurement device (Fig. 2c) in a laboratory test tank. This device measures forces along the primary x , y and z axes as well as torque around z . Combinations of two variables, amplitude A and frequency f , of the actuator's oscillatory motion (6) were tested. The ranges of each parameter were determined based on motor's saturation limits. Also recorded were time-series of the motor's angular position, as well as the current consumption of the actuator.

During post-processing, smoothing is applied to noisy data using a Lowess smoothing technique and mean values of the forces and current consumption are calculated over $n = 8$ cycles of steady state oscillation. The ratio of surge force over consumed power η is used as a metric of propulsive efficiency

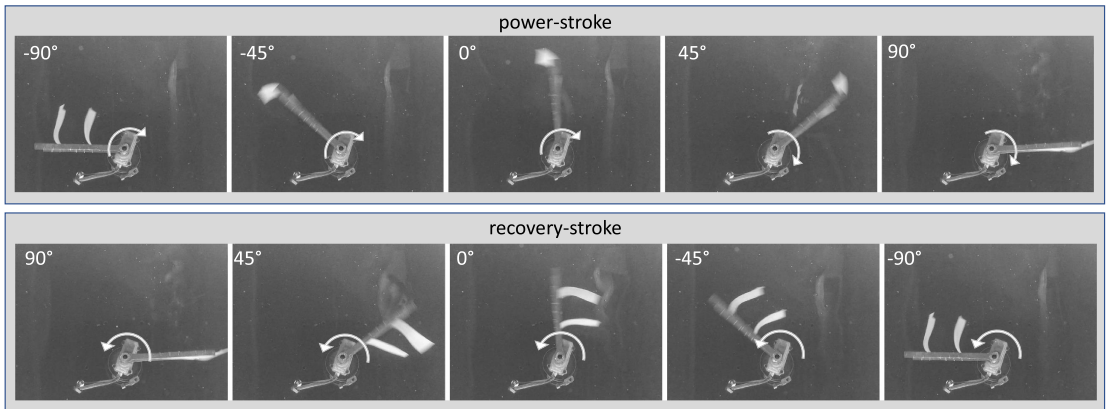


Fig. 4. Frames of the oscillation cycle showing the motion of flaps during the power and recovery stroke.

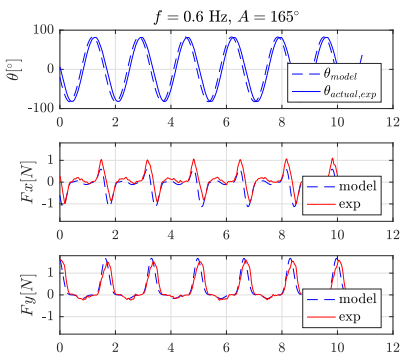


Fig. 5. Comparison of simulated model and experimentally determined forces.

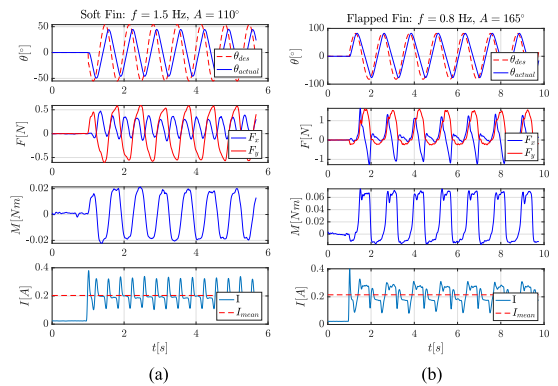


Fig. 6. Individual experimental results for position feedback, generated forces and torque as well as current consumption: (a) soft fin, (b) flapped paddle-fin.

([35]) as

$$\eta = \frac{1}{nT} \frac{\int_0^{nT} F_p(t) dt}{\int_0^{nT} VI(t) dt}. \quad (7)$$

Here F_p is the propulsive force which is F_x for the soft fin and F_y for the flapped-fin. V is the constant voltage, $I(t)$ is the current consumption, and T is the time-period of oscillation.

V. RESULTS AND DISCUSSION

A. Flapped Paddle-Fin on Testbed

A series of frames of the flapped paddle-fin during one cycle of oscillation can be seen in Fig. 4. Here it can be observed that the flaps open completely during the recovery-stroke, with negligible impedance to the flow.

Fig. 5 shows the temporal evolution of the experimentally determined as well as the simulated forces based on the model in section III. The model closely follows the experiment, apart from the fact that there is a slightly larger experimental longitudinal force F_x . This is due to the residual unmodeled wake-induced forces that occur during oscillation. On the other hand, the actual

lateral force is slightly smaller than the simulated value as the stroke velocity increases. This can be attributed to the fact that the drag coefficient C_d decreases while the flow has a positive velocity away from the fin. For our model, C_d was empirically calculated from (3) and (4) using force measurements. We assume that C_d has been averaged over the surface area of the fin. We also assume that, under no external flow conditions, the angle of attack of the flow is independent of the angular position (may depend only on angular velocity), as flow near the surface of the fin acts perpendicular to it, independent of the angular position, consequently so is C_d . However there is a dependence on the flow velocity, or angular velocity of the fin, and we assume a square-law relationship, allowing us to factor out C_d as a constant from the integral (2).

Fig. 6 shows experimental results of two different runs, one with the soft fin and one with the flapped paddle-fin. The amplitude and frequency for both fins were selected from the two actuators' data sets to demonstrate the maximum propulsive force in each case (the lateral force F_y for the flapped-fin and

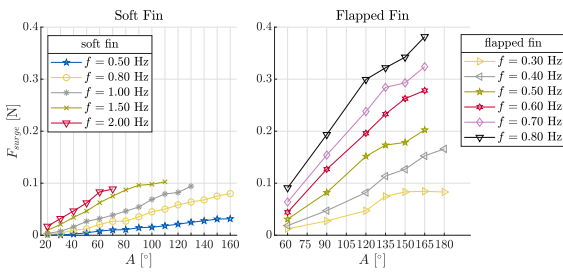


Fig. 7. Experimental results of the average propulsive force component.

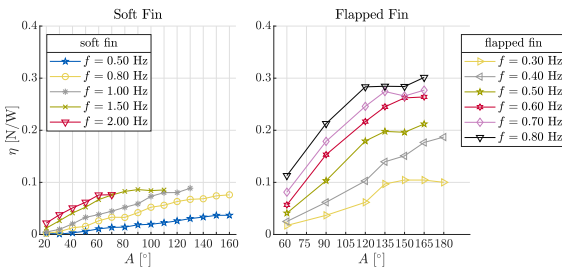


Fig. 8. Experimental results for propulsive-efficiency.

longitudinal force F_x for the soft fin), within the limitations of the motor. It can be seen in Fig. 6 a that F_y is appreciably greater than F_x , but averages to zero due to symmetric drag while F_x is significantly asymmetric since the soft fin is optimized for wake forces. On the other hand, in case of the flapped-fin, the lateral force F_y is highly asymmetric due to negligible recovery drag, and contrary to the soft fin, F_x in this case primarily contains the projected component of the lateral drag-force, and negligible wake forces, and is therefore not significantly asymmetric. Next, it can be seen that the torque M , measured around the axis of rotation of the actuator, which is the moment due to the forces generated from actuating the fin, is also asymmetric for the flapped paddle-fin and symmetric for the soft fin. Moreover, the plot of the current consumption I shows only a slight increase in mean current consumption during steady state for the flapped paddle-fin over the soft fin, while achieving significant increase in thrust.

Fig. 7 compares the average propulsive force between both fins. The range of parameters were chosen to be within the motor saturation limits. It can be seen here that the net thrust is significantly higher in case of the flapped-fin, and increases quasi-linearly with amplitude for higher frequencies.

Fig. 8 compares the propulsive efficiency of both fins. It can be seen that along with net thrust, the propulsive efficiency of the flapped-fin also increases. This can be attributed to the fact that the consumed power for both fins is comparable, but in the case of the conventional soft fin, most of the power is wasted in the lateral force component. On the other hand, the flapped-fin utilizes this dominant force, resulting in simultaneous increase of thrust and efficiency, without the need of trading them off.

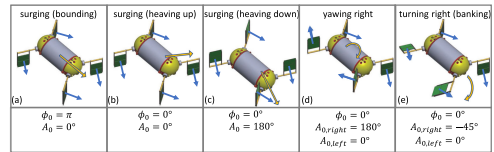


Fig. 9. Angular offset (A_0) and phase offset ϕ_0 for underwater swimming gaits. The robot's motion direction is indicated with yellow arrows. The individual actuator force directions are indicated with blue arrows.

B. The μ -CAT Robot Trials

Locomotion using the flapped paddle-fin has been studied on an AUV actuated by four servo-motors (see attached [video](#) [36]). Actuation schemes based on vectoring the mean thrust of each fin via differential variation of phase offset ϕ_0 and angular offset A_0 of oscillation have been heuristically developed in order to achieve basic locomotion gaits as illustrated in Fig. 9 and explained as follows.

- **Surging (heave up):** The four fins are synchronized in angular offset and phase of 0° . All fins generate force in the direction normal to their surface at the angular offset point (A_0), and towards the front of the robot. These forces, combined with torque during the power-stroke, cause a surge forward, as well as pitch up, allowing the negatively buoyant robot to surface.
- **Surging (heave down):** The robot fins are synchronized with an angular offset of 180° and zero phase offset. All fins generate force in the direction normal to their surface at the angular offset point (A_0), and towards the back of the robot. These forces, combined with torque during the power-stroke, cause the robot to surge backwards and down.
- **Surging (bounding):** Both the rear and front fins generate forward thrust forces, with a direction normal to their surface at the angular offset point (A_0), as well as a pitching moment that tends to rotate the robot around its lateral axis. The rear fins have a phase offset of 180° . Because of the phase offset between the front and rear fins, the moment's frequency is double of that observed in "surging (heaving up)" and "surging (heaving down)" but reduced in magnitude. This enables the robot to surge smoothly as the front fins engage the power-stroke while the rear fins recover and vice-versa. On the other hand, if the phase offset is zero, the robot moves intermittently, as demonstrated in the previous two surging gaits.
- **Yawing right:** The fins on the left of the robot have an angular offset (A_0) of 180° and those on the right side, 0° , and the phase offset is zero. This creates a difference in the forces on either side, resulting in zero net thrust force and a clockwise moment.
- **Turning right (banking):** The fins on the right have an angular offset (A_0) of 0° vectoring the force forward, while the fins on the left side have an angular offset of -45° , thereby vectoring the force downwards. This creates a clockwise yaw-torque as well as a roll-torque to the right, allowing the robot to bank right.

VI. CONCLUSION

The flapped paddle-fin mechanism showed that the lateral drag during the recovery stroke was indeed negligible, thereby enabling a high degree of asymmetry in lateral force. By exploiting the asymmetry in the lateral force with the proposed fin, thrust as well as propulsive efficiency were significantly improved over conventional fins. A mathematical model for the forces during the power and recovery stroke was developed for the proposed fin, and it was shown to closely follow the experimental data. This is beneficial for future model-based control as the forces have a simple, closed-form expression for oscillatory actuation. The proposed fin was finally mounted on an underwater robotic platform, and several basic locomotion gaits were achieved using phase and angular offset control of each fin. The robot demonstrated appreciable agility and maneuverability, thereby justifying the fin design. Further avenues for research include studying the fin dynamics in varying flow conditions, and determining the optimal fin structure and design parameters.

ACKNOWLEDGMENT

The authors would like to thank Simha Hnln for providing valuable insight into the fin design and Andres Ernits for help during the fin fabrication process.

REFERENCES

- [1] D. Roper, S. Sharma, R. Sutton, and P. Culverhouse, "A review of developments towards biologically inspired propulsion systems for autonomous underwater vehicles," *Proc. Institution Mech. Eng., Part M: J. Eng. Maritime Environ.*, vol. 225, no. 2, pp. 77–96, 2011.
- [2] Z. Shen, J. Na, and Z. Wang, "A biomimetic underwater soft robot inspired by cephalopod mollusc," *IEEE Robot. Autom. Lett.*, vol. 2, no. 4, pp. 2217–2223, Oct. 2017.
- [3] A. Villanueva, C. Smith, and S. Priya, "A biomimetic robotic jellyfish (robjelly) actuated by shape memory alloy composite actuators," *Bioinspiration Biomimetics*, vol. 6, no. 3, 2011, Art. no. 036004.
- [4] J. Najem, S. A. Sarles, B. Akle, and D. J. Leo, "Biomimetic jellyfish-inspired underwater vehicle actuated by ionic polymer metal composite actuators," *Smart Mater. Struct.*, vol. 21, no. 9, 2012, Art. no. 094026.
- [5] M. Sfakiotakis, R. Gliva, and M. Mountoufaris, "Steering-plane motion control for an underwater robot with a pair of undulatory fin propulsors," in *Proc. 24th Mediterranean Conf. Control Autom.*, 2016, pp. 496–503.
- [6] P. Liljebäck, Ø. Stavadahl, K. Y. Pettersen, and J. T. Gravdahl, "Mamba-a waterproof snake robot with tactile sensing," in *Proc. IEEE/RSJ Int. Conf. Intell. Robots Syst.*, 2014, pp. 294–301.
- [7] G. Liu, Y. Ren, J. Zhu, H. B. Smith, and H. Dong, "Thrust producing mechanisms in ray-inspired underwater vehicle propulsion," *Theor. Appl. Mech. Lett.*, vol. 5, no. 1, pp. 54–57, 2015.
- [8] O. M. Curet, N. A. Patankar, G. V. Lauder, and M. A. MacIver, "Mechanical properties of a bio-inspired robotic knifefish with an undulatory propulsor," *Bioinspiration Biomimetics*, vol. 6, no. 2, 2011, Art. no. 026004.
- [9] R. Salazar, V. Fuentes, and A. Abdelkefi, "Classification of biological and bioinspired aquatic systems: A review," *Ocean Eng.*, vol. 148, pp. 75–114, 2018.
- [10] M. Sfakiotakis, D. M. Lane, and J. B. C. Davies, "Review of fish swimming modes for aquatic locomotion," *IEEE J. Ocean. Eng.*, vol. 24, no. 2, pp. 237–252, Apr. 1999.
- [11] A. P. Mignano, S. Kadapa, J. L. Tangorra, and G. V. Lauder, "Passing the wake: Using multiple fins to shape forces for swimming," *Biomimetics*, vol. 4, no. 1, 2019, Art. no. 23.
- [12] J. L. Tangorra, G. V. Lauder, P. G. Madden, R. Mittal, M. Bozkurttas, and I. W. Hunter, "A biorobotic flapping fin for propulsion and maneuvering," in *Proc. IEEE Int. Conf. Robot. Autom.*, 2008, pp. 700–705.
- [13] R. Zhang, Z. Shen, and Z. Wang, "Ostraciiform underwater robot with segmented caudal fin," *IEEE Robot. Autom. Lett.*, vol. 3, no. 4, pp. 2902–2909, Oct. 2018.
- [14] G. V. Lauder and E. D. Tytell, "Hydrodynamics of undulatory propulsion," *Fish Physiol.*, vol. 23, pp. 425–468, 2005.
- [15] C. Siegenthaler, C. Pradaliere, F. Günther, G. Hitz, and R. Siegwart, "System integration and fin trajectory design for a robotic sea-turtle," in *Proc. IEEE/RSJ Int. Conf. Intell. Robots Syst.*, 2013, pp. 3790–3795.
- [16] B. Han, X. Luo, X. Wang, and X. Chen, "Mechanism design and gait experiment of an amphibian robotic turtle," *Adv. Robot.*, vol. 25, no. 16, pp. 2083–2097, 2011.
- [17] D. Font *et al.*, "Design and implementation of a biomimetic turtle hydrofoil for an autonomous underwater vehicle," *Sensors*, vol. 11, no. 12, pp. 11 168–11 187, 2011.
- [18] P. Kodati, J. Hinkle, A. Winn, and X. Deng, "Microautonomous robotic ostraciiform (MARCO): Hydrodynamics, design, and fabrication," *IEEE Trans. Robot.*, vol. 24, no. 1, pp. 105–117, Feb. 2008.
- [19] N. Kato, "Control performance in the horizontal plane of a fish robot with mechanical pectoral fins," *IEEE J. Ocean. Eng.*, vol. 25, no. 1, pp. 121–129, Jan. 2000.
- [20] P. E. Sitorus, Y. Y. Nazaruddin, E. Leksono, and A. Budiyo, "Design and implementation of paired pectoral fins locomotion of labriform fish applied to a fish robot," *J. Bionic Eng.*, vol. 6, no. 1, pp. 37–45, 2009.
- [21] S.-H. Song *et al.*, "Turtle mimetic soft robot with two swimming gaits," *Bioinspiration Biomimetics*, vol. 11, no. 3, 2016, Art. no. 036010.
- [22] S. B. A. Kashem, S. Jawed, J. Ahmed, and U. Qidwai, "Design and implementation of a quadruped amphibious robot using duck feet," *Robotics*, vol. 8, no. 3, 2019, Art. no. 77.
- [23] B. Kwak and J. Bae, "Design of hair-like appendages and comparative analysis on their coordination toward steady and efficient swimming," *Bioinspiration Biomimetics*, vol. 12, no. 3, 2017, Art. no. 036014.
- [24] S. B. Behbahani and X. Tan, "Design and modeling of flexible passive rowing joint for robotic fish pectoral fins," *IEEE Trans. Robot.*, vol. 32, no. 5, pp. 1119–1132, Oct. 2016.
- [25] C. J. Esposito, J. L. Tangorra, B. E. Flammang, and G. V. Lauder, "A robotic fish caudal fin: Effects of stiffness and motor program on locomotor performance," *J. Exp. Biol.*, vol. 215, no. 1, pp. 56–67, 2012.
- [26] G. V. Lauder, "Function of the caudal fin during locomotion in fishes: Kinematics, flow visualization, and evolutionary patterns," *Amer. Zoologist*, vol. 40, no. 1, pp. 101–122, 2000.
- [27] S. C. Licht, M. Wibawa, F. S. Hover, and M. S. Triantafyllou, "Towards amphibious robots: Asymmetric flapping foil motion underwater produces large thrust efficiently," Massachusetts Inst. Technol. Sea Grant College Program, Tech. Rep., 2009. [Online]. Available: <https://dspace.mit.edu/handle/1721.1/96997>
- [28] C. Meurer, A. Simha, Ü. Kotta, and M. Kruusmaa, "Nonlinear orientation controller for a compliant robotic fish based on asymmetric actuation," in *Proc. Int. Conf. Robot. Autom.*, 2019, pp. 4688–4694.
- [29] W. Yang and B. Song, "Experimental investigation of aerodynamics of feather-covered flapping wing," *Appl. Bionics Biomech.*, vol. 2017, pp. 1–8, 2017.
- [30] K. E. Crandell and B. W. Tobalske, "Kinematics and aerodynamics of avian upstrokes during slow flight," *J. Exp. Biol.*, vol. 218, no. 16, pp. 2518–2527, 2015.
- [31] M. Bozkurttas, J. Tangorra, G. Lauder, and R. Mittal, "Understanding the hydrodynamics of swimming: From fish fins to flexible propulsors for autonomous underwater vehicles," in *Proc. Adv. Sci. Technol.*, Trans Tech Publ, 2008, vol. 58., pp. 193–202.
- [32] N. Martin, C. Roh, S. Idrees, and M. Gharib, "To flap or not to flap: Comparison between flapping and clapping propulsions," *J. Fluid Mech.*, vol. 822, 2017. [Online]. Available: https://www.cambridge.org/core/journals/journal-of-fluid-mechanics/volume/30403C855643CF929A0F964C8D4CA5FE?sort=canonical.position%3Aasc&pageNum=2&searchWithinIds=30403C855643CF929A0F964C8D4CA5FE&productType=JOURNAL_ARTICLE&template=cambridge-core%2Fjournal%2Farticle-listings%2Flistings-wrapper&hideArticleJournalMetaData=true&displayNasaAds=false
- [33] C. Georgiades, M. Nahon, and M. Buehler, "Simulation of an underwater hexapod robot," *Ocean Eng.*, vol. 36, no. 1, pp. 39–47, 2009.
- [34] R. Gkliva, M. Sfakiotakis, and M. Kruusmaa, "Development and experimental assessment of a flexible robot fin," in *Proc. IEEE Int. Conf. Soft Robot.*, 2018, pp. 208–213.
- [35] J. S. Palmisano, R. Ramamurti, J. D. Geder, M. Pruessner, W. C. Sandberg, and B. Ratna, "How to maximize pectoral fin efficiency by control of flapping frequency and amplitude," in *Proc. 18th Int. Symp. Unmanned Unethered Submersible Technol.*, Portsmouth, New Hampshire, USA, 2013.
- [36] Youtube video: "Flapped paddle fin AUV" 2019. [Online]. Available: <https://youtu.be/1Q0tyTmzbGA>, Accessed: Feb. 28, 2020.

Appendix 3

Publication III

R. Gkliva and M. Kruusmaa, "Soft fluidic actuator for locomotion in multi-phase environments," IEEE Robotics and Automation Letters, vol. 7, no. 4, pp. 10462-10469, 2022

Soft Fluidic Actuator for Locomotion in Multi-Phase Environments

Roza Gkliva ^{1b} and Maarja Kruusmaa ^{1b}

Abstract—This letter presents the design, development, and experimental assessment of a soft fluidic actuator that can enable locomotion in a variety of aquatic and terrestrial environments. Most actuation strategies for amphibious locomotion rely on rigid, fast moving components to generate thrust and tractive forces. Our prototype, comprising soft materials, and relying on simple motion planning and control strategies, demonstrates two gaits, that we employ for locomotion in two vastly different scenarios, underwater swimming and moving on granular terrain with varying levels of water content. By adjusting its internal pressure, the actuator dynamically varies its stiffness and shape, and transitions between wheel and soft paddle form. Experimental results of locomotion in controlled laboratory conditions serve as proof-of-concept for the proposed actuator's efficacy. Using two different motion patterns and control schemes, we show that this prototype achieves both thrust and tractive forces.

Index Terms—Amphibious locomotion, hydraulic/pneumatic actuators, soft robot materials and design.

I. INTRODUCTION

TRADITIONAL methods of terrestrial locomotion include wheels and tracks, with legged configurations gaining in popularity [1]. Aquatic locomotion counterparts include combinations of propellers and lift-based control surfaces or multi-thruster systems [2]. These methods have a proven record of highly efficient and agile locomotion in their respective applications. However, their performance declines significantly when manoeuvring is needed in unstructured, unstable environments, as well as when transitioning through drastically different environments. To mitigate the diminishing performance of locomotion in these conditions, the research community is exploring alternative methods of locomotion, including hybrid designs [3], [4] and compliant materials [4], [5]. In this work, we use these two strategies to develop and study actuation methods for locomotion in aquatic and terrestrial environments, as well as through multi-phase environments such as shore zones (Fig. 1).

Manuscript received 22 March 2022; accepted 13 July 2022. Date of publication 19 July 2022; date of current version 4 August 2022. This letter was recommended for publication by Associate Editor P. Chirarattananon and Editor Y. -L. Park upon evaluation of the reviewers' comments. This work was supported in part by the European Union's Horizon 2020 Research and Innovation Programme ROBOMINERS under Grant Agreement 820971, and in part by the Estonian Research Council under Grant PRG1243 Multiscale Natural Flow Sensing for Coasts and Rivers. (Corresponding author: Roza Gkliva.)

The authors are with the Centre for Biorobotics, Department of Computer Systems, Tallinn University of Technology, 12618 Tallinn, Estonia (e-mail: roza.gkliva@ttu.ee; maarja.kruusmaa@ttu.ee).

This letter has supplementary downloadable material available at <https://doi.org/10.1109/LRA.2022.3192204>, provided by the authors.

Digital Object Identifier 10.1109/LRA.2022.3192204

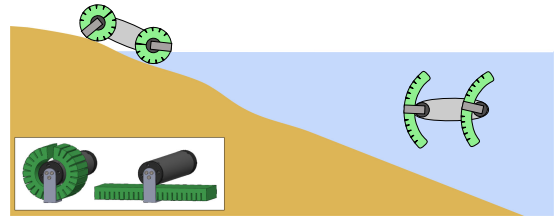


Fig. 1. Illustration of a concept vehicle using the proposed actuator. Top left: the fully pressurized, stiffer actuator generates tractive forces enabling terrestrial locomotion by rotating around a motor shaft. Right: the softer actuator generates propulsive forces enabling underwater swimming by oscillating around the motor shaft. Inset: CAD model of the actuator in both states.

A C-shaped compliant leg design, was used to demonstrate exceptionally agile locomotion, enabling the RHex vehicle to negotiate terrains of varying complexity [6]. This work was instrumental for the development of a series of actuators and robots, aimed at studying amphibious locomotion using appendages that resemble wheels or curved legs and compliant flippers, by manually [7] or dynamically [8]–[10] switching between curved leg or wheel, and flat fin.

Mechanically simpler mechanisms, that employ underactuated and partially passive configurations, have also successfully demonstrated amphibious locomotion. A design combining a circular 1-DOF leg and flat flipper [11], and a similar actuator comprising a stiff fan-shaped leg and a flipper with manually variable stiffness [12] have demonstrated locomotion on terrestrial and aquatic environments. A design comprising a stiff leg with a grate-like morphology, covered by a compliant flap that transforms the leg into a paddle and passively optimizes drag forces during swimming, allowed the RoboTerp quadruped to transition between walking on land and swimming on the water surface [13]. A flat paddle 1-DOF mechanism with a passive elastic hinge enabled underwater walking and swimming for the PEAR hexapod [14].

The strategies mentioned above include rigid, and/or fast moving parts, that can be damaging to the environment or to the robot itself, and can generate large unwanted accelerations in the robot's motion. The combination of rapid impacts of rigid actuators on granular and deformable terrains has additional negative effects on locomotion performance, resulting in reduced traction or the actuators digging into the ground. Integrating compliant parts into locomotion mechanisms can introduce benefits such as increased safety when interacting with the environment, the ability to store and release energy through passive elastic

components, as well as improved quality of motion when negotiating unstructured environments [4]. Completely or partially soft robots have been developed to study amphibious locomotion. A variable stiffness material-pneumatic prototype [15] was used to investigate the dynamic switch between leg and flipper form by adjusting the temperature and internal pressure of its components. Despite its slow actuation, this method shows promising results mostly due to the decoupling of stiffness and shape. A sea urchin-inspired amphibious robot using actuated rigid spines and extensible soft legs was used to investigate bio-inspired locomotion patterns in aquatic and terrestrial conditions [16]. A quadruped robot comprising groups of interconnected thin and soft McKibben actuators demonstrated locomotion on wet and dry terrains, using a variety of walking and crawling gaits [17]. A worm-inspired soft robot, featuring serially connected and individually driven pneumatic actuators, was used to investigate crawling and swimming gaits [18].

In this letter we propose a 1-DOF, reconfigurable, soft fluidic actuator (Fig. 1). Comparing to previous implementations of actuators in similar environments, our prototype employs a rather simple mechanism that allows to dynamically modify its shape and stiffness. Its morphology and compliant material, in combination with simple control and motion planning strategies, enable locomotion in aquatic, terrestrial, and in multi-phase environments. The reconfiguration of the actuator's shape and functionality is achieved by varying its internal pressure. Its locomotion performance was evaluated via a series of experiments in controlled laboratory conditions. To our knowledge, this is the first soft fluidic actuator of this kind to be used for amphibious locomotion. The compliant material and its simplicity of actuation can lead to more widespread usage of this type of actuator, especially in applications where less invasive presence is required.

The contributions of this work include the development of an actuator with the following characteristics:

- **Flexibility of locomotion:** We provide experimental proof-of-concept for locomotion in aquatic, terrestrial and mixed environments.
- **Simplicity of reconfiguration and actuation:** The actuator transitions between its two states by simply varying its internal pressure, enabling a variety of locomotion modes. Actuation relies on 1-DOF rotational or oscillatory motion patterns.
- **Simplicity of design and fabrication:** 3D-printed moulds, wax, and a commercially available composite silicone are the main components used for fabrication.

In what follows we describe the actuator concept, including its design and fabrication (Section II), the experimental evaluation, including test rigs, experimental protocols, as well as motion patterns and controllers that were implemented (Section III). Experimental results and a discussion on the efficacy of the proposed prototype are in Section IV.

II. ACTUATOR CONCEPT AND FABRICATION

The design of this concept actuator was inspired by the fast PneuNet design described in [19]. PneuNet actuators consist of

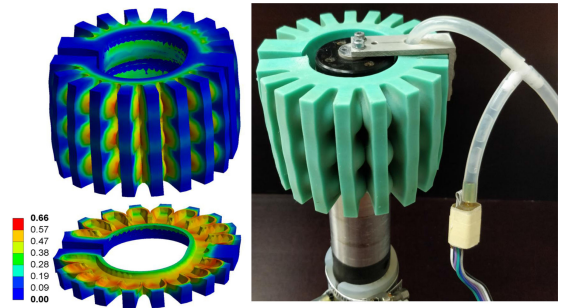


Fig. 2. Deformation due to pressure increase of 100 kPa. Left: equivalent elastic strain levels in a FEM simulation (Ansys), Right: the physical actuator with a fluid intake tube and a pressure sensing module.

a soft elastomeric part that contains a network of interconnected air chambers and optionally include flexible strain-limiting elements that affect the actuator's bending profile [20], [21]. Their shape can be controlled by adjusting the internal pressure. Despite their relatively simple design and actuation, their reliability and robustness [19], [22] have made them attractive for a variety of applications. They have been used mainly to study grasping [23], rehabilitation [24], as well as locomotion [22], [25], [26].

We hypothesize that because this design allows the dynamic adjustment of the actuator's stiffness and shape, it is suitable for locomotion in a variety of different conditions, premise partly supported by [12]. By increasing the internal pressure in the actuator, its internal cavities expand. Due to a non-extensible fabric embedded in its flat side, it is constrained from elongation and is deformed as seen in Figs. 1 and 2. With increased internal pressure, in its cylindrical shape, and wrapped around the motor canister, it is stiffer and can better withstand radial and tangential forces. This makes it appropriate to function as a wheel and generate tractive forces by rotating around the motor shaft.

When the internal pressure in the actuator is kept at levels that do not cause deformation, it can be used to generate propulsive forces by performing oscillations around the motor shaft, functioning as a pair of bilateral paddles. Splitting the actuator vertically into two halves, and examining each half separately as an individual paddle, we can look into the actuation cycle's reciprocating motion consisting of two phases: a power phase and a recovery phase. During the recovery phase, the force that is applied to the actuator's external surface, because of the motor's oscillatory motion pattern, causes the paddle to bend towards its smooth side. During the power phase, the segmented geometry on the other side of the actuator prevents bending in the other direction. We hypothesize that this asymmetry will result in a positive net force throughout the actuation cycle, that can be used to generate thrust forces while submerged.

A. FEM Static Analysis

A nonlinear FEM simulation was used to predict the actuator's bending behaviour and to determine the morphology and dimensions appropriate for the experimental validation described

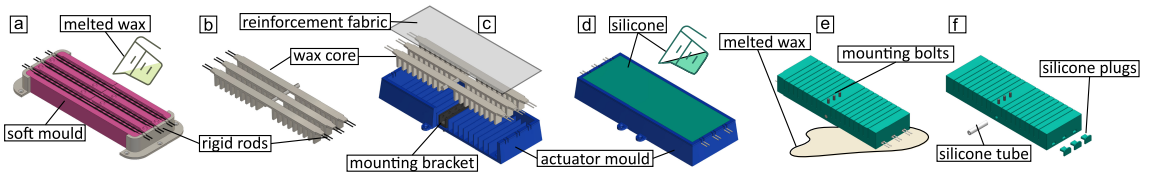


Fig. 3. The fabrication process: (a) metal rods ($\varnothing.5$ mm) are suspended over a soft mould on two 3D-printed brackets. These rods provide stability to the wax core, and serve as attachment points during casting the actuator. Melted wax is poured into the mould. (b) After setting, the wax core is demoulded and cleaned of excess wax. (c) An aluminium bracket with a series of bolts attached to it, the wax core and a reinforcement fabric are assembled into the mould. The bolts are used to fasten the cured actuator to a motor shaft. (d) Silicone is mixed, degassed and poured into the mould. (e) After a second degassing and curing, the silicone actuator is demoulded, the wax is melted off at 80°C and pours out from openings on its sides. (f) After the wax and metal rods have been removed and traces of wax have been cleaned, silicone plugs and an intake silicone tube are glued in using Sil-Poxy by Smooth-On.

TABLE I
PROTOTYPE SPECIFICATIONS

Dimensions at rest	$17 \times 6 \times 2$ cm
Soft actuator mass	0.25 kg
Silicone	Elite Double 22 (Zhermack)
Silicone hardness	22 Shore A
Elongation at break	450%
Reinforcement fabric	Art.Nr:09502-003-000007 (KauPo)

TABLE II
SENSORS FOR DATA ACQUISITION

Description	Model	Sampling Rate	Experiment type
Angular position	maxon hall sensors	100 Hz	underwater
Angular velocity	maxon hall sensors	10 Hz	terrestrial
Current	INA219 by TI	100 Hz	both
Force/Torque	ATI Axia80-m20	100 Hz	underwater
Pressure	MS5407-AM	50 Hz	both
Displacement	VL53L0X	40 Hz	terrestrial

in this work. For this analysis we used a hyperelastic model of the actuator's material, the actuator's geometry from a 3D CAD model, and a set of boundary conditions described below. The results included the equivalent elastic stress and strain, and the total deformation.

To characterize the material, we ran tensile tests with specimens made of Elite Double 22 silicone compound by Zhermack (Badia Polesine (RO), Italy). We used an Instron 5866 uniaxial testing machine and followed the ASTM D412 standard [27] for Vulcanized Rubber and Thermoplastic Elastomers. To simulate the actuator's behaviour in Ansys a 3^{rd} order Yeoh model was used, as it can describe deformation under large strains using limited data [28]. Assuming incompressibility of the material, the model takes the form:

$$W(I_1) = \sum_{i=1}^3 C_{i0}(I_1 - 3)^i. \quad (1)$$

Here, $I_1 = \lambda_1^2 + \lambda_2^2 + \lambda_3^2$ is the first invariant of the three principal stretch ratios, and $C_{10} = 78783$ Pa, $C_{20} = 16732$ Pa, and $C_{30} = 6618.5$ Pa are the material constants obtained from fitting the tensile experiment data to the 3^{rd} order Yeoh model. For the purpose of the simulations, the density of the material was experimentally estimated as $\rho = 1164$ kg / m³.

The model was verified using a scaled-down partial version of the actuator and comparing to simulated results. To determine the simulation boundary conditions, the actuator's internal pressure was measured while it was pressurized until it reached a desired point of deformation after which it was allowed to return to rest. Due to its incompressibility, water was used to increase the internal pressure [19], to apply a consistent pressure on the internal walls of the actuator and on the pressure sensor.

To generate the final design of the actuator, the model was used in an iterative process of design and simulation cycles [29], using SolidWorks to modify the CAD model and Ansys Workbench

to run FEM simulations. The following settings and boundary conditions were used in a static structural simulation in Ansys Workbench [29], [30]. a) The external surface surrounding the fixation bolts was defined as a "fixed support". b) All internal surfaces were used to apply pressure, normal to these surfaces. c) The external surfaces between the chambers were defined as "frictionless contact" pairs, to prevent the actuator geometry from penetrating itself. d) The contact between the inextensible layer and the hyperelastic material was defined as a "bonded contact".

The inextensible elastic layer was modelled using a 1^{st} order Yeoh model with material constant $C_{10} = 7.9$ MPa [31]. The aim of this process was to find a geometry that can achieve the desired deformation without failing under load. The number and geometry of chambers, the wall thickness, as well as the gap size between chambers, were modified to achieve the desired bending profile [30]. The inextensible layer thickness and total length of the actuator were constant, and were determined by the thickness of the strain limiting fabric and by the radius of the motor canister respectively. While this design borrows its main features from the original PneuNet actuators, it differs in using a fixation point and fluid intake in the middle of the actuator, as well as using three parallel networks of chambers, compared to the traditional single network configuration. A simulation and the prototype of the final design can be seen in Fig. 2 deformed under 100 kPa of added pressure.

B. Prototype Fabrication

The fabrication of the actuator follows a two-step lost-wax casting process. During the first step (Fig. 3(a), (b)), a wax core is created, that will be used to create the actuator's internal cavity network. During the second step (Fig. 3(c)–(f)) the wax core is

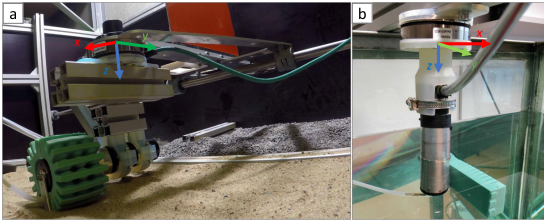


Fig. 4. Experimental testbeds. a: terrestrial, b: underwater.

used in a 3D-printed mould, to cast a soft actuator. The final specifications of the actuator can be seen in Table I.

This method of fabrication may be slightly more challenging compared to the traditionally popular method of casting the top and bottom parts of the actuator separately and then bonding them together [32]. However, in this case, it produces more consistent results, with fewer failure points.

III. EXPERIMENTS

To validate our hypothesis regarding the suitability of the actuator for locomotion in underwater and terrestrial conditions, we ran experiments separately for these two scenarios, as described in the following subsections. For both scenarios, the soft actuator was mounted on a waterproofed BLDC motor (EC-max 30 by Maxon Motors) driven by an EPOS2 36/2 motor controller, such that it was allowed to fully deform and rotate around the motor shaft (Fig. 4, and accompanying video). Two different combinations from an array of sensors (Table II) were employed in the two test rigs. The data acquisition was performed by a Windows PC running Matlab scripts and a multi-rate Simulink model under Real-Time Desktop in external mode. Sampling rates were chosen to minimize data acquisition latency.

To achieve locomotion in aquatic and terrestrial environments, two motion profiles are required. A continuous rotation of the fully deformed actuator will allow it to generate tractive forces when on ground. An oscillatory motion of the actuator in its low pressure state can generate thrust forces when fully submerged. The motor driver used in these experiments offers a variety of operating modes with different controller structures [33]. For each motion an appropriate control scheme was implemented as described in following sections. All controller gains and feedforward factors were tuned using the “regulation tuning wizard” in the Epos Studio software.

A. Characterization of Blocked Swimming Force

The actuator’s efficacy related to generating underwater propulsive forces was evaluated via a series of experiments in a water tank (Fig. 4(b)), focusing on the measurement of forces generated by in-place oscillations.

The oscillatory motion was achieved by prescribing a sinusoidal trajectory with amplitude A and frequency f (Table III) to the motor that the actuator is mounted on. Fig. 5 shows the control scheme employed for the actuator’s oscillatory motion. This scheme was implemented in Maxon’s EPOS2 Module 36/2

TABLE III
EXPERIMENT PARAMETERS

Type of Experiment	Parameter	Range
Underwater	Oscillation amplitude ($^{\circ}$)	[60, 70, 80, 90]
	Oscillation frequency (Hz)	[1.5, 1.75]
Terrestrial	Angular velocity (rpm)	[5, 10, 20, 30, 40]
	Water content in soil (%)	[0, 6.25, 12.5, 25]

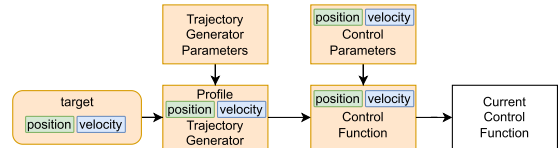


Fig. 5. Control structure for position control (oscillations) and velocity control (rotations). Orange colour denotes scheme-specific functions.

as a position controller using “Profile Position Mode” [34]. This structure employs a position PID controller with a current PI controller as subordinate regulator. At a constant rate, a target position is generated based on the sinusoidal motion profile. The target position is applied to the trajectory generator, which generates a position demand value that is used as input to a position control function. The profile position trajectory generator parameters include the type of motion profile, a velocity profile and an acceleration/deceleration profile that are calculated based on the target position. To protect the motor from high current, velocity and acceleration limits are imposed. The position controller accepts the position demand value and the actual position of the motor shaft. The position control parameters include velocity and acceleration demand values calculated based on the desired A , f , the maximum allowed tracking error, as well as PID controller gains and feedforward factors for velocity and acceleration. The controller output is a current demand value that is fed to the current controller.

For each experiment, the actuator’s internal pressure was initially increased by 5–10 kPa, to ensure that the internal chambers maintain their shape, not allowing the actuator to bend backwards. Water was used to increase the internal pressure, to maintain constant buoyancy. Then the actuator was mounted on a force sensor that was suspended over a tank of water, such that the actuator was fully submerged and oriented with its large side normal to the x -axis (Fig. 4(b)). The ranges of A and f were determined empirically, based on position tracking performance, and motion profile limitations described above. The experiment and data acquisition ran for a number of whole periods of actuation, with 10 replicates per A , f combination. The internal pressure of the actuator was measured but not actively controlled.

Post-processing included smoothing of noisy data and calculating evaluation metrics as described below. The noise in the current and force data was filtered out using a 10^{th} order Savitzky-Golay filter. A Hampel filter was used to remove outliers in the current measurements. To summarize the results of the experiments, averaged values were calculated using a

number ($n = 7$) of whole actuation periods. To evaluate the controller performance, the amplitude tracking error was calculated by comparing the average actual oscillation amplitude with the nominal desired oscillation amplitude.

$$A_{error} = |A - (\bar{\theta}_{high} - \bar{\theta}_{low})| \quad (2)$$

To evaluate the actuator's energetic characteristics, the ratio of propulsive force over the averaged consumed power was used [35], for a number n of whole periods T .

$$\eta = \frac{\overline{F_p}}{\overline{P_{in}}} = \frac{1}{nT} \frac{\int_0^{nT} F_p(t) dt}{\int_0^{nT} VI(t) dt}. \quad (3)$$

Here, $\overline{P_{in}}$ is the averaged consumed power calculated using the measured current consumption $I(t)$ and a constant voltage $V = 24$ V, and $F_p(t)$ is the instantaneous propulsive force.

The actuator's first natural frequency has been experimentally estimated using force measurements after manual excitation, and found to be $f_{n,air} = 2.439$ Hz and $f_{n,water} = 1.7241$ Hz while suspended in air and in water respectively.

B. Characterization of Terrestrial Velocity

The actuator's efficacy for locomotion in dry and wet terrestrial conditions was evaluated via a set of experiments on sandy terrain (Fig. 4(a)), focusing on the measurement of the distance travelled by the actuator as it rolls on the ground.

To achieve a wheel-like behaviour and to generate tractive forces, the internal pressure of the actuator is increased until it reaches the desired deformed state, and a constant angular velocity is commanded to its motor. The control scheme used for this purpose (Fig. 5), is implemented as a velocity controller with "Profile Velocity Mode" in Maxon's EPOS2 Module 36/2 [34]. This structure employs a velocity PI controller with a current PI controller as subordinate regulator. A target velocity is sent to the profile velocity trajectory generator, which generates a velocity demand value that is used as input to a velocity control function. The profile velocity trajectory generator parameters include profile acceleration and deceleration values calculated based on a desired acceleration threshold. The velocity controller accepts the velocity demand coming from the trajectory generator as well as the actual angular position of the motor shaft. The velocity control parameters include the velocity controller gains and the feedforward factors for velocity and acceleration. The output is a current demand value that is sent to the current controller along with the current measurement.

Our study includes the transition between aquatic and terrestrial locomotion, such as when a robot would traverse a littoral zone to move from land to water and vice versa. The sand-water-air environment as a three-phase system is appropriate for investigating locomotion in such multi-phase environments, due to the effects of water content to the shear modulus of sand [36]. To address this aspect, the experiment variables included a sweep of actuator angular velocities, as well as varying levels of water content to investigate moving through a multi-phase environment (Table III), with 10 replicates per combination. These parameters were selected based on the hypothesis that they affect the actuator's efficacy and can demonstrate its ability to generate

tractive forces in dry and wet conditions, and to examine the multi-phase conditions between the two locomotion scenarios described in this work. The range of the parameters was determined based on visual observations of the water content in the experimental tank, as well as based on limitations of the experimental setup, e.g., limited space for wet sand experiments.

For each experiment, the actuator was mounted on a gantry that slides on a linear guide with reduced friction, allowing motion in 2 DOF: translation along x and rotation around x . Initially, the actuator, mounted on the motor shaft and resting flat on the terrain, was deformed until it achieved "wheel status," by increasing its internal pressure. Then, the motor shaft was actuated to follow a rotational motion pattern, causing the deformed actuator to rotate. The traction forces between the actuator and the soil cause the gantry to move linearly along x . The experiment and data acquisition ended when the gantry had travelled a predetermined distance. The constant pressure to deform the actuator was applied by adding air with a bicycle pump. As pressure did not fluctuate throughout hours of experiments, active control was not necessary.

In post-processing, noisy data was filtered and performance metrics were calculated and summarized as averaged values. The velocity of the gantry along the x -axis was estimated using backwards differentiation of the smoothed (10^{th} order Savitzky-Golay filter) linear displacement.

$$u(t) = \frac{x(t) - x(t-1)}{\tau}, \quad (4)$$

where x is the gantry's position along x at times t and $t-1$, and τ is the time increment.

Assuming no braking during the range of data, the slip ratio of the wheel was calculated based on [37], as:

$$s(t) = \frac{r\omega(t) - u(t)}{r\omega(t)}, \quad (5)$$

where r is the deformed actuator's radius, assuming constant curvature and ω is the angular velocity of the motor shaft.

To evaluate the actuator's energy characteristics, the Cost of Transport metric was used:

$$CoT = \frac{\overline{P_{in}}}{mg\bar{u}} = \frac{1}{nT} \frac{\int_0^{nT} VI(t) dt}{mg \int_0^{nT} u(t) dt}. \quad (6)$$

Here, $m = 2.15$ kg is the mass of the actuator assembly, including the actuator, and all hardware that are moved by it, and excluding the gantry that is balancing on the rail, g is the acceleration of gravity, and $u(t)$ is the gantry's instantaneous velocity along the x direction. Averaged values were calculated over a number n of full periods T or rotation, to account for periodic phenomena in the actuator's motion.

IV. RESULTS AND DISCUSSION

The experiments presented here were focused on the evaluation of the actuator's locomotion performance in two drastically different environments, by measuring blocked swimming forces in an aquatic environment and locomotion velocity while traversing sandy terrain. Additionally, we hypothesized that modifying

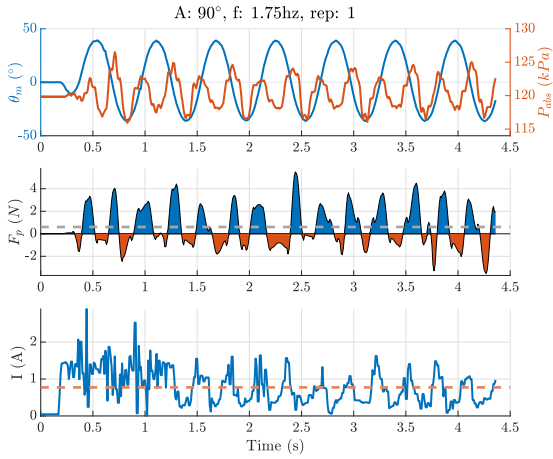


Fig. 6. Indicative underwater force experiment. The upper graph shows the motor’s actual position, as it follows a sinusoidal motion pattern, and the internal absolute pressure of the actuator. The middle graph shows the temporal evolution of the instantaneous thrust force. The dashed horizontal line denotes the phase-averaged value, while positive (forward) forces are shaded blue and negative (backward) forces are shaded red. The lower graph shows the instantaneous current consumption of the motor in blue colour and the average current consumption as a dashed horizontal line.

the terrain conditions by varying the water content of sand will give us some understanding of the actuator’s behaviour in the transition between terrestrial and aquatic locomotion. The following subsections offer a description of the experimental results and a discussion on the two locomotion modes. General discussion on the actuator’s performance can be found in Section V.

A. Swimming Forces

Fig. 6 shows indicative underwater experiment results. Examining the pressure measurements in combination with the motor shaft angular position, we observe that the pressure measurement can provide an indication of the actuator’s deformation under drag forces that apply pressure to its external surfaces as a result of its own motion in water. This pattern, compared to the pattern of generated thrust forces, shows a correlation between the angular position and velocity of the motor, the internal pressure, and the magnitude and direction of the thrust force. More specifically, while positive force peaks develop during the faster motion of the actuator, when the actuator stops and changes direction of motion, negative forces are generated. During this stop of motion, the elastic behaviour of the material causes the actuator to momentarily return to its original undeformed state, potentially causing these negative forces. This correlation between measured pressure and thrust force could offer a proprioceptive approach for estimating the generated forces. There also seems to be a slight asymmetry in the high and low peaks of the pressure graph, as well as inconsistencies in the duration of the positive and negative forces. These may be attributed to manufacturing inconsistencies, how

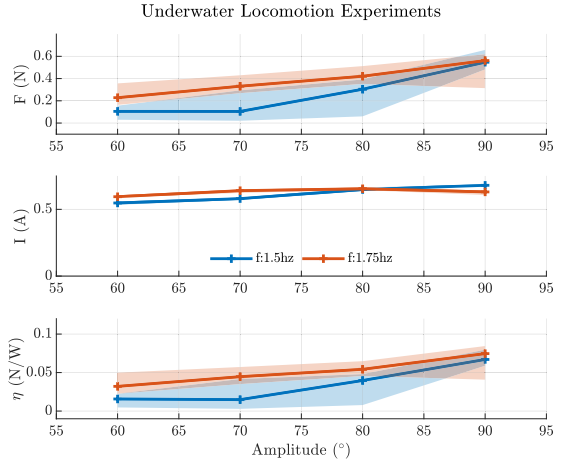


Fig. 7. Aggregate results of underwater experiments. Two frequencies and four amplitudes of oscillation were studied. The crosses show the median values of 10 replicates for each parameter set, with 25th and 75th percentiles as shaded areas. The upper graph shows the evolution of thrust forces, as oscillation amplitude increases, for two frequencies of oscillation. The middle graph shows the median current consumption. The lower graph shows the energetic efficiency metric as described in (3).

the actuator is mounted in the test rig, or to waves reflecting off the walls of the test tank and interfering with the measurements.

Fig. 7 offers a summary of the results of the entire sweep of experimental parameters. The upper graph shows that increasing both oscillation parameters generally results in increased thrust forces. The reduced current consumption during faster oscillations ($f = 1.75$ Hz) can be attributed to the tested frequency being close to the actuator’s first natural frequency. However, while higher frequency shows a higher thrust force trend in the lower amplitudes, the two datasets converge at higher amplitudes, due to increased amplitude tracking error at the (90° , 1.75 Hz) parameter set, caused by velocity and acceleration limits set to the motion controller.

The efficiency metric η , shows that this actuator performs worse than previous prototypes designed exclusively for aquatic locomotion [38], [39], mainly due to reduced force generation. While further optimization of the actuator’s morphology, motion planning and control can improve this metric, we recognize that the reduced performance is a trade-off that enables locomotion in terrestrial conditions.

B. Terrestrial Velocity

Fig. 8 presents indicative terrestrial experiment results. It is evident that a constant angular velocity of the motor generates a somewhat constant linear velocity of the gantry. A jump that occurs when the actuator is rolling over its seam (e.g., at 5 sec on Fig. 8) can be corrected with higher internal pressure or with optimizing the actuator dimensions.

Fig. 9 presents a summary of the terrestrial locomotion experiments. These graphs show that increasing the motor’s angular

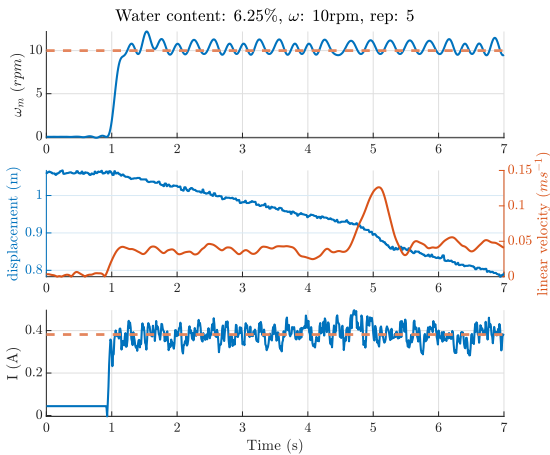


Fig. 8. Indicative terrestrial locomotion experiment in sand. The upper graph shows the actual angular velocity of the actuator’s motor shaft. The dashed horizontal line denotes the desired angular velocity. The middle graph shows the temporal evolution of the gantry’s position along the rail as it moves towards the distance sensor, as well as the gantry’s velocity calculated based on (4). The lower graph shows the instantaneous current consumption in blue colour and the averaged as a red dashed line.

velocity results in higher linear velocity of the gantry. The gantry velocity is also dependent on the water content level, with the two edge cases (0% and 25%) achieving lower speeds with a nonlinear relationship and the two middle sets (6.25% and 12.5%) achieving consistently higher speeds following a rather linear relationship. This dependence on water content appears also in the middle and bottom graphs, with the two edge sets having a higher slip ratio and Cost of Transport, and the 6.25% set consistently lowest. This behaviour is supported by Fall *et al.* in [36] that showed that some water in sand increases its shear modulus, but too much water decreases it back to levels of dry sand. As a qualitative confirmation of this, we observed visually (see accompanying video) that in loose soil, either dry sand or very wet sand, the actuator can more easily dig itself into the soil if it finds resistance along its direction of motion.

V. CONCLUSION

We have presented the design and development of a soft fluidic actuator that can enable aquatic and terrestrial locomotion, from fully submerged swimming to negotiating wet and dry granular terrain. This wide range of locomotion is achieved by using a design and a compliant material that allow the actuator to transition between two shapes: paddle and wheel, by modifying the actuator’s internal pressure.

Our hypothesis regarding the proposed actuator’s locomotion performance was evaluated via a series of experiments in the two target environmental conditions. We also investigated conditions that resemble the transition between aquatic and terrestrial locomotion, by gradually increasing the water content of the soil. The experiments and data analysis justify the actuator design and choice of material, and serve as proof-of-concept. While

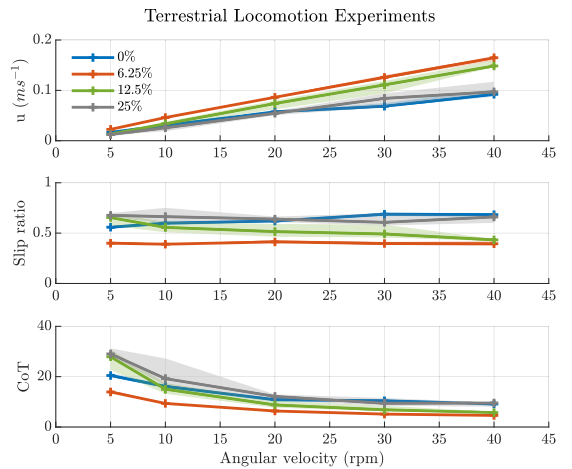


Fig. 9. Aggregate results for terrestrial locomotion experiments. The crosses show the median values of 10 replicates for each parameter set, with 25th and 75th percentiles as shaded areas. The upper graph shows the linear velocity of the gantry for all angular velocities and all levels of water content in the soil. The middle and bottom graphs show the slip ratio and the Cost of Transport calculated based on (5) and (6) respectively.

the performance in either locomotion scenario is suboptimal, we accept this trade-off, as the same design choices allow the easy reconfigurability of shape and stiffness that enables amphibious locomotion. Regarding locomotion on deformable and granular terrains, compared to most stiff-legged amphibious prototypes, this actuator demonstrates relatively low impact motion and does not disturb the terrain as much. This can be very beneficial to a robot’s locomotion characteristics, when e.g., exploring areas with fragile ecosystems where low environmental impact is necessary, or when performing data collection where high accelerations can affect data quality.

We hypothesize that a third mode of locomotion, surface swimming, can be achieved by this actuator, using a combination of the two modes described in this letter, i.e., rotating around the motor shaft with low internal pressure, while on the water surface. This mode of locomotion demonstrated in previous literature [40] was not experimentally investigated in this work, but will be part of our future work.

More importantly, we aim to further investigate the transition between locomotion modes, extending the experimental setups to allow more degrees of freedom, including unconstrained underwater and terrestrial locomotion. This will allow investigation of dynamic transitions between modes, such as underwater to surface swimming, surface swimming to terrestrial locomotion, etc. Currently, the transition between the actuator’s two forms is achieved by either manually increasing the volume of its internal fluid, or using a bulky pump system. To increase portability and autonomy of the actuator, a mechanism will be developed that will allow the controlled transition between the two forms. Additionally, optimization of motor kinematics and motion planning will be investigated to improve performance.

ACKNOWLEDGMENT

The authors thank Asko Ristolainen for his contributions on the actuator fabrication, as well as Jaan Rebane and Andres Ernits for their support with the experimental setup.

REFERENCES

- [1] B. Siciliano and O. Khatib, *Springer Handbook of Robotics*. Berlin, Germany: Springer, 2008.
- [2] G. Antonelli, *Underwater Robots*, vol. 3, Berlin, Germany: Springer, 2014.
- [3] L. Bruzzone and G. Quaglia, "Locomotion systems for ground mobile robots in unstructured environments," *Mech. Sci.*, vol. 3, no. 2, pp. 49–62, 2012.
- [4] M. Calisti, G. Picardi, and C. Laschi, "Fundamentals of soft robot locomotion," *J. Roy. Soc. Interface*, vol. 14, no. 130, 2017, Art. no. 20170101.
- [5] D. Rus and M. T. Tolley, "Design, fabrication and control of soft robots," *Nature*, vol. 521, no. 7553, pp. 467–475, 2015.
- [6] U. Sarani, M. Buehler, and D. E. Koditschek, "RHex: A simple and highly mobile hexapod robot," *Int. J. Robot. Res.*, vol. 20, no. 7, pp. 616–631, 2001.
- [7] C. Georgiades et al., "AQUA: An aquatic walking robot," in *Proc. IEEE/RSJ Int. Conf. Intell. Robots Syst.*, 2004, pp. 3525–3531.
- [8] X. Liang et al., "The AmphiHex: A novel amphibious robot with transformable leg-flipper composite propulsion mechanism," in *Proc. IEEE/RSJ Int. Conf. Intell. Robots Syst.*, 2012, pp. 3667–3672.
- [9] L. Bai, G. Dou, W. Duan, Y. Sun, J. Zheng, and X. Chen, "Amphibious robot with a novel composite propulsion mechanism," in *Proc. 6th IEEE Int. Conf. Adv. Robot. Mechatron.*, 2021, pp. 442–447.
- [10] Y. Sun, S. Ma, and X. Luo, "Design of an eccentric paddle locomotion mechanism for amphibious robots," in *Proc. IEEE Int. Conf. Robot. Biomimetics*, 2010, pp. 1098–1103.
- [11] B. B. Dey, S. Manjanna, and G. Dudek, "Ninja legs: Amphibious one degree of freedom robotic legs," in *Proc. IEEE/RSJ Int. Conf. Intell. Robots Syst.*, 2013, pp. 5622–5628.
- [12] B. Zhong, S. Zhang, M. Xu, Y. Zhou, T. Fang, and W. Li, "On a CPG-based hexapod robot: AmphiHex-II with variable stiffness legs," *IEEE/ASME Trans. Mechatron.*, vol. 23, no. 2, pp. 542–551, Apr. 2018.
- [13] A. R. Vogel, K. N. Kaipa, G. M. Krummel, H. A. Bruck, and S. K. Gupta, "Design of a compliance assisted quadrupedal amphibious robot," in *Proc. IEEE Int. Conf. Robot. Automat.*, 2014, pp. 2378–2383.
- [14] T. Kim, Y.-W. Song, S. Song, and S.-C. Yu, "Underwater walking mechanism of underwater amphibious robot using hinged multi-modal paddle," *Int. J. Control. Automat. Syst.*, vol. 19, no. 4, pp. 1691–1702, 2021.
- [15] R. L. Baines, J. W. Booth, F. E. Fish, and R. Kramer-Bottiglio, "Toward a bio-inspired variable-stiffness morphing limb for amphibious robot locomotion," in *Proc. 2nd IEEE Int. Conf. Soft Robot.*, 2019, pp. 704–710.
- [16] T. Paschal, M. A. Bell, J. Sperry, S. Steniewicz, R. J. Wood, and J. C. Weaver, "Design, fabrication, and characterization of an untethered amphibious sea urchin-inspired robot," *IEEE Robot. Automat. Lett.*, vol. 4, no. 4, pp. 3348–3354, Oct. 2019.
- [17] A. A. M. Faudzi, M. R. M. Razif, G. Endo, H. Nabae, and K. Suzumori, "Soft-amphibious robot using thin and soft McKibben actuator," in *Proc. IEEE Int. Conf. Adv. Intell. Mechatron.*, 2017, pp. 981–986.
- [18] E. Milana et al., "EELWORM: A bioinspired multimodal amphibious soft robot," in *Proc. 3rd IEEE Int. Conf. Soft Robot.*, 2020, pp. 766–771.
- [19] B. Mosadegh et al., "Pneumatic networks for soft robotics that actuate rapidly," *Adv. Funct. Mater.*, vol. 24, no. 15, pp. 2163–2170, 2014.
- [20] F. Ilievski, A. D. Mazzeo, R. F. Shepherd, X. Chen, and G. M. Whitesides, "Soft robotics for chemists," *Angewandte Chemie*, vol. 123, no. 8, pp. 1930–1935, 2011.
- [21] B. Gorissen, D. Reynaerts, S. Konishi, K. Yoshida, J.-W. Kim, and M. De Volder, "Elastic inflatable actuators for soft robotic applications," *Adv. Mater.*, vol. 29, no. 43, 2017, Art. no. 1604977.
- [22] M. T. Tolley et al., "A resilient, untethered soft robot," *Soft Robot.*, vol. 1, pp. 213–223, 2014.
- [23] J. Shintake, V. Caccuciolo, D. Floreano, and H. Shea, "Soft robotic grippers," *Adv. Mater.*, vol. 30, no. 29, 2018, Art. no. 1707035.
- [24] P. Polygerinos et al., "Towards a soft pneumatic glove for hand rehabilitation," in *Proc. IEEE/RSJ Int. Conf. Intell. Robots Syst.*, 2013, pp. 1512–1517.
- [25] J. Ning, C. Ti, and Y. Liu, "Inchworm inspired pneumatic soft robot based on friction hysteresis," *J. Robot. Automat.*, vol. 1, no. 1, pp. 54–63, 2017.
- [26] R. F. Shepherd et al., "Multigait soft robot," *Proc. Nat. Acad. Sci. USA*, vol. 108, no. 51, pp. 20400–20403, 2011.
- [27] *Standard Test Methods for Vulcanized Rubber and Thermoplastic Elastomers-Tension*, ASTM D412-16(2021), ASTM International, West Conshohocken, PA, USA, 2021. [Online]. Available: www.astm.org
- [28] C. Renaud, J.-M. Cros, Z.-Q. Feng, and B. Yang, "The yeoh model applied to the modeling of large deformation contact/impact problems," *Int. J. Impact Eng.*, vol. 36, no. 5, pp. 659–666, 2009.
- [29] C. Tawk and G. Alici, "Finite element modeling in the design process of 3D printed pneumatic soft actuators and sensors," *Robotics*, vol. 9, no. 3, 2020, Art. no. 52.
- [30] M. S. Xavier, A. J. Fleming, and Y. K. Yong, "Finite element modeling of soft fluidic actuators: Overview and recent developments," *Adv. Intell. Syst.*, vol. 3, no. 2, 2021, Art. no. 2000187.
- [31] P. Polygerinos et al., "Modeling of soft fiber-reinforced bending actuators," *IEEE Trans. Robot.*, vol. 31, no. 3, pp. 778–789, Jun. 2015.
- [32] P. Polygerinos et al., "Soft robotics: Review of fluid-driven intrinsically soft devices; manufacturing, sensing, control, and applications in human-robot interaction," *Adv. Eng. Mater.*, vol. 19, no. 12, 2017, Art. no. 1700016.
- [33] EPOS2 positioning controllers application notes, maxon motor AG, Sachseln, Switzerland, 2016. [Online]. Available: www.maxongroup.com
- [34] EPOS2 positioning controllers firmware specification, maxon motor AG, Sachseln, Switzerland, 2017. [Online]. Available: www.maxongroup.com
- [35] J. S. Palmisano, R. Ramamurti, J. D. Geder, M. Pruessner, W. C. Sandberg, and B. Ratna, "How to maximize pectoral fin efficiency by control of flapping frequency and amplitude," in *Proc. 18th Int. Symp. Unmanned Untethered Submersible Technol.*, 2013, pp. 124–132.
- [36] A. Fall et al., "Sliding friction on wet and dry sand," *Phys. Rev. Lett.*, vol. 112, no. 17, 2014, Art. no. 175502.
- [37] K. Yoshida and H. Hamano, "Motion dynamics and control of a planetary rover with slip-based traction model," in *Proc. Int. Soc. Opt. Photon. Unmanned Ground Veh. Technol.*, 2002, pp. 275–286.
- [38] R. Gkliva, M. Sfakiotakis, and M. Kruusmaa, "Development and experimental assessment of a flexible robot fin," in *Proc. IEEE Int. Conf. Soft Robot.*, 2018, pp. 208–213.
- [39] A. Simha, R. Gkliva, Ü. Kotta, and M. Kruusmaa, "A flapped paddle-fin for improving underwater propulsive efficiency of oscillatory actuation," *IEEE Robot. Automat. Lett.*, vol. 5, no. 2, pp. 3176–3181, Apr. 2020.
- [40] G. Dudek et al., "A visually guided swimming robot," in *Proc. IEEE/RSJ Int. Conf. Intell. Robots Syst.*, 2005, pp. 3604–3609.

Curriculum Vitae

Personal data

Name Roza Gkliva
Date and place of birth 15 June 1982, Rodos, Greece
Nationality Greek

Contact information

E-mail roza.gkliva@ttu.ee

Education

2017-... Tallinn University of Technology, School of Information Technologies,
PhD, Computer and Systems Engineering
2012-2016 Technological Educational Institute of Crete, School of Engineering,
MSc, Advanced Systems of Manufacturing, Automation, and Robotics
2005-2010 Technological Educational Institute of Crete, School of Engineering,
BSc, Mechanical Engineering

Language competence

Greek native
English fluent
German basic

Professional employment

2017- ...	Tallinn University of Technology	Early Stage Researcher
2017-2017	Tallinn University of Technology	Engineer
2017-2017	University of the Aegean	Lecturer
2014-2016	Technological Educational Institute of Crete	Engineer
2013-2015	Technological Educational Institute of Crete	Lecturer
2012-2016	Lionbridge IT	Internet Assessor
2011-2011	Laserworks Engraving	Mechanical Engineer

Defended theses

- 2016, Design and Development of Undulatory Fin Mechanisms, MSc, supervisor Dr. M. Sfakiotakis, Technological Educational Institute of Crete, Department of Mechanical Engineering & Department of Electrical Engineering
- 2010, Computer Aided Kinematic Simulation of Mechanisms, BSc supervisor Dr. M. Petousis, Technological Educational Institute of Crete, Department of Mechanical Engineering

ISSN 2585-6901 (PDF)
ISBN 978-9949-83-951-3 (PDF)